

Investigating Ptychographic Phase Retrieval in Terms of Vibration Correction, Online Data Analysis, and Direct 3D Reconstruction

Dissertation
zur Erlangung des Doktorgrades
an der Fakultät für Mathematik, Informatik und
Naturwissenschaften
Fachbereich Physik
der Universität Hamburg

Vorgelegt von
Silvio Achilles

Hamburg

2023

The work described in this thesis was done at the Photon Science division of Deutsches Elektronen-Synchrotron, a Research Centre of the Helmholtz Association.

Gutachter der Dissertation:	Prof. Dr. Christian G. Schroer Prof. Dr. Peter Modregger
Zusammensetzung der Prüfungskommission:	Prof. Dr. Daniela Pfannkuche Prof. Dr. Christian G. Schroer Prof. Dr. Peter Modregger Prof. Dr. Patrick Huber Dr. habil. Thomas Keller
Vorsitzende der Prüfungskommission:	Prof. Dr. Daniela Pfannkuche
Datum der Disputation:	16.01.2024
Vorsitzender des Fach-Promotionsausschusses Physik:	Prof. Dr. Markus Drescher
Leiter des Fachbereichs Physik:	Prof. Dr. Günter Sigl
Dekan der Fakultät MIN:	Prof. Dr.-Ing. Norbert Ritter

Abstract

X-ray ptychography is becoming increasingly popular. The semi-transparency of matter to X-rays allows to look into their structure and thereby lay the foundation to understand their functionality. X-ray Ptychography achieves a spatial resolution down to the single nanometer regime. A broad range of materials are well suited for investigation, such as biological samples, catalysts or microchips. Modern synchrotron radiation sources allow to perform ptychographic scans in minutes, which enables the investigation of fast dynamic processes. Furthermore, ptychography is perfectly suited to be combined with tomographic routines to resolve three-dimensional structures.

Nevertheless, ptychography is still a challenging method. The mechanical hardware of a ptychographic microscope must provide a stability similar to the achieved spatial resolution. Instabilities cause a blurring of the reconstructed object and reduce the reconstruction quality.

The ptychographic data evaluation is computationally expensive and mostly done offline, which means the data acquisition and evaluation are subsequent steps. If the sample is positioned out of the field of view, this is only noticed once the data is reconstructed, leading to a waste of valuable measurement time at synchrotron radiation sources. The computational effort of the ptychographic data evaluation is enormous. The evaluation software has to be optimized to cope with the amount of data. Fourth generation synchrotron radiation sources such as PETRA IV will acquire ptychographic datasets at even higher data rates.

In this thesis, three projects are presented that address the current challenges of ptychography. First, an algorithmic approach is introduced that corrects for the vibrations that occur during the ptychographic data acquisition. The algorithm decreases the spatial resolution by a factor 2 for a dataset that is significantly disturbed by vibrations. Second, a structure and implementation for online ptychography has been developed, that performs the data evaluation while the data is still acquired. This enables a real time feedback during the experiment. Third, an optimized software for direct 3D ptychography has been implemented, that yields a performance high enough to catch up with the high acquisition rate of fourth generation synchrotron sources. The implementation is about a factor 3000 faster than the before version.

Zusammenfassung

Ptychographie mit Röntgenstrahlung wird immer beliebter. Die Semi-Transparenz der Materie für Röntgenstrahlung ermöglicht es, die Struktur der Materie zu untersuchen und damit die Grundlage für das Verständnis der Funktionsweise zu legen. Mit der Röntgen-Ptychographie ist eine räumliche Auflösung bis in den einstelligen Nanometerbereich erreichbar. Vielfältige Materialien sind für die Untersuchung geeignet, wie biologische Proben, Katalysatoren oder Mikrochips. Moderne Synchrotronquellen erlauben es ptychographische Scans innerhalb von Minuten durchzuführen, wodurch die Untersuchung dynamischer Prozesse ermöglicht wird. Weiterhin lässt sich die Röntgen-Ptychographie mit tomographischen Verfahren kombinieren, um dreidimensionale Strukturen darzustellen.

Nichtsdestotrotz ist Röntgen-Ptychographie eine anspruchsvolle Methode. Die mechanische Hardware eines ptychographischen Mikroskops muss eine Stabilität aufweisen, die der erreichten räumlichen Auflösung entspricht. Instabilitäten reduzieren die Qualität des rekonstruierten Objekts.

Die ptychographische Datenauswertung ist sehr rechenintensiv und wird i.d.R. offline durchgeführt. Offline bedeutet, die Datenerfassung und -Auswertung sind nacheinander abfolgende Schritte. Sollte die Probe nicht innerhalb des Sichtfelds positioniert sein, wird erst bemerkt wenn die Daten rekonstruiert sind. Dies führt dazu, dass wertvolle Messzeit an Synchrotronquellen verschwendet wird.

Weiterhin erfordert der hohe Rechenaufwand, dass die Auswertungssoftware entsprechend optimiert ist, um den hohen Datenraten gerecht zu werden. Synchrotronquellen der vierten Generation werden noch deutlich größere Datenmengen erzeugen.

Diese Arbeit behandelt die zuvor dargestellten Herausforderungen mit drei Projekten. Zunächst wird ein algorithmischer Ansatz vorgestellt, der die bei der ptychografischen Datenerfassung auftretenden Vibrationen korrigiert. Der Algorithmus reduziert die räumliche Auflösung um einen Faktor 2 für einen Datensatz, der signifikant durch Vibrationen beeinträchtigt ist. Weiterhin wurde eine Implementierung für die Online-Ptychographie entwickelt, die die Datenauswertung während der Datenerfassung durchführt. Dies ermöglicht eine Rückmeldung in Echtzeit während des Experiments. Abschließend wurde eine GPU-beschleunigte Implementierung für die direkte 3D Ptychographie entwickelt. Die erreichte Rekonstruktionsgeschwindigkeit ist hoch genug, um mit den hohen Akquisitionsraten von Synchrotronquellen der vierten Generation mitzuhalten. Die Implementierung ist ungefähr um einen Faktor 3000 schneller als die vorherige Version.

Contents

Abbreviations	1
1 Introduction	1
2 Theoretical Background	3
2.1 Interaction of X-rays and Matter	3
2.1.1 X-rays	3
2.1.2 Scattering	3
2.1.3 Absorption	4
2.1.4 Complex Refractive Index	4
2.1.5 Propagation	5
2.1.6 Coherence	7
2.1.7 Synchrotron Radiation	7
2.2 Ptychography	8
2.2.1 The Ptychographic Model	9
2.2.2 extended Ptychographic Iterative Engine	12
2.2.3 refractive Ptychographic Iterative Engine	13
2.2.4 Difference Map	14
2.2.5 parallel extended Ptychographic Iterative Engine	15
2.2.6 Software	15
2.3 Tomography	17
2.3.1 The Tomographic Model	18
2.3.2 Sinogram	20
2.3.3 Standard Backprojection	20
2.3.4 Filtered Backprojection	21
2.3.5 Simultaneous Iterative Reconstruction Technique	25
2.3.6 Conjugate Gradient Least Squares	27
2.3.7 Software	28
2.4 Ptychographic Tomography	29
2.4.1 Data Acquisition	29
2.4.2 Ptychographic X-ray Computed Tomography	30
2.4.3 Coupled Ptychographic Tomography	31

3	Ensemble Refinement	33
3.1	Adaption of the Ptychographic Model	34
3.2	Simulation Study	36
3.2.1	Verification of the Model and the Implementation	39
3.2.2	Uncertainties of the Non-Negative Least Squares Fit	40
3.2.3	A First Reconstruction	41
3.3	Siemens star	42
3.3.1	Dataset	42
3.3.2	Reconstruction	44
3.3.3	Spatial Resolution	48
3.4	Zeolite	51
3.4.1	Dataset	51
3.4.2	Reconstruction	53
3.5	Implementation Details and Performance	54
3.6	Conclusion	56
4	Streaming Ptychography	59
4.1	Ptychography at the COSMIC Beamline	60
4.1.1	Fast CCD Detector and Preprocessing	60
4.1.2	Illumination Initialization	61
4.2	Implementation	63
4.2.1	ZeroMQ	63
4.2.2	Network Transfer of Images	63
4.2.3	Events	64
4.2.4	ptycho	67
4.3	Demonstration of the Streaming Reconstruction	68
4.4	Offline Reconstructions	70
4.5	Pipeline	70
4.6	Conclusion	72
5	Coupled Ptychographic Tomography	73
5.1	Implementation Details	73
5.2	Sample and Experiment	74
5.3	Ptychographic and Tomographic Reconstruction Algorithms	75
5.4	Performance	77
5.5	Position Refinement	78
5.5.1	Simulation Study	78

5.5.2 Zeolite	82
5.6 Conclusion	84
6 Summary and Conclusion	85
7 Acknowledgements	99

Abbreviations

TEM	Transmission Electron Microscopy
SEM	Scanning Electron Microscopy
XRF	X-ray Fluorescence
PXCT	Ptychographic X-ray Computed Tomography
CPT	Coupled Ptychographic Tomography
PtyNAMi	Ptychographic Nano-Analytical Microscope
ER	Ensemble Refinement
PIE	Ptychographic Iterative Engine
ePIE	extended Ptychographic Iterative Engine
pePIE	parallel extended Ptychographic Iterative Engine
refPIE	refractive Ptychographic Iterative Engine
DM	Difference Map
BP	Backprojection
FBP	Filtered Backprojection
ART	Algebraic Reconstruction Technique
SIRT	Simultaneous Iterative Reconstruction Technique
SART	Simultaneous Algebraic Reconstruction Technique
BP-SART	Backprojection-based SART
CGLS	Conjugate Gradient Least Squares
NNLS	Non-Negative Least Squares
JSON	JavaScript Object Notation
FZP	Fresnel Zone Plate
CRLs	Compound Refractive Lenses
GPU	Graphics Processing Unit
CPU	Central Processing Unit
HDR	High Dynamic Range
DOF	Depth of Field
CCD	Charge Coupled Device
MB	Megabyte
GB	Gigabyte
FIB	Focused Ion Beam
DESY	Deutsches Elektronen-Synchrotron
ALS	Advanced Light Source
LBNL	Lawrence Berkeley National Laboratory
NERSC	National Energy Research Scientific Computing Center

1 Introduction

X-ray microscopy has become an essential tool to understand the functional behaviour of modern materials, such as microchips or catalysts. Consider the amount of solar cells that is deployed almost everywhere. The efficiency of a solar cell is, inter alia, limited by small defects in their nano structure. To understand the correlation between defects and efficiency, methods are necessary to quantify the defects and the electrical performance. X-rays are an ideal tool for this. They have the unique feature that matter is semi-transparent for them, such that an X-ray beam transmits even through extended materials.

A lot of X-ray microscopy methods have been developed that allow to analyze the electron density [1]–[3], atomic composition [4]–[6], crystallographic information [7]–[10], or the chemical state [11]–[13]. Multi-modal experiments allow to acquire and evaluate multiple of these contrasts simultaneously [14]–[19]. The lowest spatial resolution is obtained with scanning X-ray microscopy methods [20]. In many of these approaches, the limit for the spatial resolution is defined by the focal spot size of the utilized X-ray optics.

In contrast, X-ray ptychography overcomes this limitation [21]. A 2D detector and a reconstruction algorithm function as a virtual lens, thereby achieve a magnification similar to an objective lens in an optical microscope. This yields a superior spatial resolution beyond the probe size. The popularity of ptychography is supported by its reliability and flexibility. A ptychographic dataset has a certain degree of redundancy, by illuminating overlapping regions while scanning the sample. This makes the data evaluation very stable. Furthermore, the scanning allows to image extended specimens, and ptychography can be combined with tomographic routines to zoom into the 3D nano structure of a material. Therefore, many synchrotron sources make use of ptychography [22]–[27].

Despite ptychographies high popularity and wide field of application, it comes with many challenges that need to be addressed. Crucial for a spatial resolution in the single nanometer regime is the mechanical stability during the experiment. Instabilities cause a blurring in the ptychographic reconstruction and thereby increase the spatial resolution. Another challenge is the large amount of data that a ptychographic scan acquires to reconstruct a small region of the sample. The result of 2D ptychography is a complex-valued image that has roughly a size of a few Megabyte (MB). In contrast, the amount of collected data can be up to several

Gigabyte (GB). Commonly, the raw diffraction data is saved on a storage system and consumes an enormous amount of hardware resources. The processing of the acquired data is computationally very expensive. In order to perform the computational data evaluation on a routine basis, it is essential to have software that is stable and optimized to cope for the high data rates. Furthermore, ptychography is conventionally done offline, meaning the data evaluation is only done once the data acquisition is completed. This yields a limiting experience for the user. Mistakes made during a ptychographic scan can only be identified after the scan is done.

This thesis comprises three projects in chapter 3 - 5 which address the above mentioned challenges of ptychography. The outline of this work is as follows.

First, chapter 2 summarizes the theoretical principles on which the methods in this thesis are build up. Starting from a general description of X-rays, their interaction with matter, the propagation through free space and the importance of coherence. The first method introduced is X-ray ptychography, which is central to all projects in this thesis. Afterwards, an introduction to tomography is given. The theory concludes by elaborating how ptychography and tomography can be combined.

Chapter 3 introduces an approach for ptychography to algorithmically correct mechanical instabilities happening during the data acquisition. The correction of the disturbances relies on a mathematical determination of the relative movement between sample and illumination via a least squares optimization. The approach is tested on simulated and experimental data.

Chapter 4 elaborates the development of online ptychographic data analysis. The acquired data is reconstructed on-the-fly to give a feedback for the user already during the scan. The live evaluation is part of a pipeline that includes an offline reconstruction with highest quality for postprocessing.

Chapter 5 presents the development of a Graphics Processing Unit (GPU) accelerated framework for Coupled Ptychographic Tomography (CPT). The coupled approach has been proven to be beneficial over the conventional approach [28], [29]. The combined mathematical description of ptychography and tomography allows to utilize features such as 2D ptychographic position correction during the 3D reconstruction.

Finally, chapter 6 gives an outlook about the effect of these developments for the future of X-ray ptychographic imaging. Especially important is the prospective availability of fourth generation synchrotron sources [30]–[36], that have a coherent flux by a factor 100 to 1000 larger than third generation sources. It is highlighted how the contributions of this work can be continued.

2 Theoretical Background

This chapter describes the theoretical principles that are necessary to understand the evaluations and discussions in this thesis. For the beginning, a brief introduction to X-ray radiation and its interaction with matter is given in section 2.1. This enables to have a thorough look on ptychography in section 2.2 and tomography in section 2.3. Finally, it is elaborated how ptychography and tomography can be combined in section 2.4.

2.1 Interaction of X-rays and Matter

The information in this section can be found in [37], if not otherwise noted.

2.1.1 X-rays

Radiation is quantized in small packages referred to as photons. A photon has an electric field and a magnetic field that oscillate perpendicularly against each other, while propagating through space. The periodicity of this oscillation is called the wavelength λ and the photons energy E is directly proportional to λ

$$E = \frac{hc}{\lambda} = h\nu. \quad (2.1)$$

The velocity of light is denoted by $c \approx 3 \cdot 10^8$ m/s, the photons frequency by $\nu = \frac{1}{\lambda}$ and the Planck constant by $h = 6.626 \cdot 10^{-34} \frac{\text{J}}{\text{Hz}}$. X-rays are photons with a wavelength roughly between 10 nm and 10 pm. Furthermore, X-rays can interact with matter, by two different processes: Scattering and absorption. Those are explained in the next two sections.

2.1.2 Scattering

There are two types of scattering: elastic and inelastic. Throughout this thesis, only elastic scattering is considered and inelastic scattering is not further described. A detailed derivation of the elastic scattering process would start by explaining the scattering of a photon with a single electron and gradually increases to compounds of atoms that are described as a homogenous volume.

In a simplified picture, the elastic scattering process is given by the following. The electric field of a photon causes the electron density of an atom to oscillate with the same frequency as the photon. The oscillating electron density emits a spherical wave with the same frequency ν as the incident photon. When having a wavefield that scatters with a material, then many spherical waves are emitted. The different pathways of all these spherical waves interfere with each other.

2.1.3 Absorption

A photon can be absorbed by an atom. The atom is excited into a state with higher energy, where one electron leaves the atom, and the atom remains in an excited state. The excited electronic system relaxes with a series of transitions.

Due to the relaxation, energy gets free. There are different possibilities for what can happen with the energy. The energy can leave the atom as a photon, which is referred to as X-ray Fluorescence (XRF). However, any effect after the absorption of the photon is not considered in this thesis and a further description is omitted.

2.1.4 Complex Refractive Index

Now, a mathematical quantification for the interaction of radiation and matter is introduced, which is the complex refractive index n

$$n(\lambda) = 1 - \delta(\lambda) + i\beta(\lambda), \quad (2.2)$$

in which δ describes the phase shift due to scattering and β the decrease in the amplitude due to absorption. The imaginary unit is $i^2 = -1$. The 1 in equation 2.2 can be understood as a wave propagating through vacuum, meaning that in vacuum $\delta = \beta = 0$. Both δ and β are material constants, but they are dependent on the wavelength λ of the radiation. In this thesis, the radiation is always considered as monochromatic and the wavelength dependency of n is dropped.

The thin-object approximation is used to model the interaction of radiation and matter. The approximation considers that only single scattering occurs. Furthermore, the samples extent along the propagation path must fit well inside the Depth of Field (DOF) of the illumination. Then, the interaction of a wavefront P_0 with a

material n is given by

$$P = P_0 e^{ik \int_0^d n(x)-1 dx}, \quad (2.3)$$

$$P = P_0 e^{-ik \int_0^d \delta(x) dx} e^{-k \int_0^d \beta(x) dx}, \quad (2.4)$$

with P being the wavefront after interacting with the material, e is the exponential constant, and $k = \frac{2\pi}{\lambda}$ the wave-vector. The constituents δ and β must be integrated along the length d of the propagation path x through the material.

Later in this thesis, a lot of attention is given to δ and β , such that the definition of the complex refractive index decrement ν is introduced here

$$\nu := n - 1 = -\delta + i\beta. \quad (2.5)$$

2.1.5 Propagation

With the understanding how X-rays interact with matter, it is not clear yet how X-rays propagate through free space, or vacuum. This is of particular interest as ptychography relies on a mathematical model for the propagation. A full description would start from the Maxwell equations. Here, only a truncated picture is drawn that yields the equations to perform the wavefield propagation. The explanation is based on the Huygens-Fresnel-Principle. [38]

Consider the wavefront $\psi_0(x_0, y_0, 0)$ shown in figure 2.1. The propagated wavefield ψ at position (x, y, z) is given by

$$\psi(x, y, z) = \frac{1}{i\lambda} \iint_{\psi_0} \psi_0(x_0, y_0, 0) \frac{e^{ikr}}{r} \cos(\theta) dx_0 dy_0. \quad (2.6)$$

The distance between the point of origin and the point of incidence is denoted by r . The angle between r and the normal vector at $(x_0, y_0, 0)$ is denoted by θ . The integration is performed by expressing r as

$$r = \sqrt{z^2 + (x - x_0)^2 + (y - y_0)^2}. \quad (2.7)$$

Inserting equation 2.7 into equation 2.6 yields something complicated to solve. There are a couple of approximations necessary to arrive at a feasible expression for equation 2.6, including the Fresnel approximation. The final approximated form of equa-

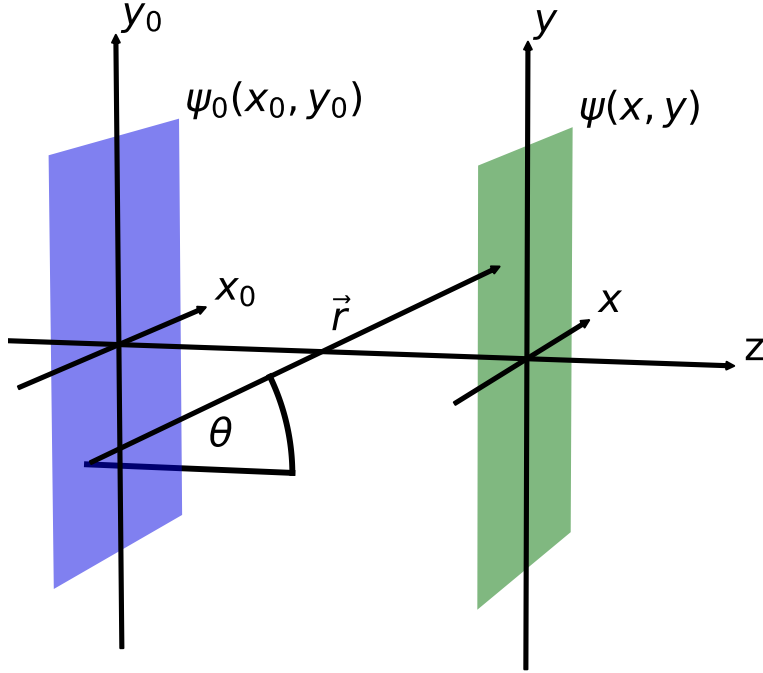


Figure 2.1: Definition of the coordinate system for the propagation of a wavefield ψ_0 from an incident plane $(x_0, y_0, 0)$ to an arriving plane (x, y, z) .

tion 2.6 is

$$\psi(x, y, z) = \frac{e^{ikz} e^{\frac{ik}{2z}(x^2+y^2)}}{i\lambda z} \iint_{-\infty}^{\infty} \psi_0(x_0, y_0) e^{ik\frac{x_0^2+y_0^2}{2z}} e^{-i2\pi\frac{xx_0+yy_0}{\lambda z}} dx_0 dy_0, \quad (2.8)$$

which is the Fresnel diffraction integral and allows for a propagation to any given point (x, y, z) . When working in long distances, the Fraunhofer approximation can be utilized that states

$$z \gg k \frac{(x_0^2 + y_0^2)_{\max}}{2}. \quad (2.9)$$

Exemplarily equation 2.9 is tested for a dataset treated in chapter 3 and 5. The size of the wavefield is $x_0 \approx y_0 \approx 1.8 \mu\text{m}$ and the wavelength is $\lambda = 0.138 \text{ nm}$. This yields that the propagation distance z must be much greater than 0.148 m , which is well fulfilled with an actual distance of 2.13 m . The Fraunhofer approximation in

equation 2.9 allows to simplify Fresnel diffraction integral in equation 2.8 to

$$\psi_z(x, y) \approx \frac{e^{ikz} e^{\frac{ik}{2z}(x^2+y^2)}}{i\lambda z} \iint_{-\infty}^{\infty} \psi_0(x_0, y_0) e^{-i2\pi(u_x x + u_y y)} dx_0 dy_0, \quad (2.10)$$

in which u_x and u_y are the spatial frequencies $\frac{x}{\lambda z}$ and $\frac{y}{\lambda z}$, respectively. Equation 2.10 is a 2D Fourier transform \mathcal{F} . Hence, the propagation into long distances, from now on described as the far-field, is done by applying a Fourier transformation to the incident wavefield ψ_0 .

2.1.6 Coherence

Ptychography relies on coherent radiation. The definition of coherence given here originates from [37]. The term coherence describes a constant phase relation of wavefields. Assuming two photons are in phase at a certain time and position. They will become out of phase due to propagation when the photons are not perfectly monochromatic or do not propagate in the same direction. The non-monochromaticity is described by the longitudinal coherence length L_L

$$L_L = 0.5 \cdot \frac{\lambda^2}{\Delta\lambda}, \quad (2.11)$$

which states that two photons with a wavelength difference $\Delta\lambda$ are out of phase after propagating a distance of L_L .

When two photons are out of phase due to the divergence of the individual propagation paths, then it is referred to as transverse coherence. The transversal coherence length describes the dimensions of the propagated wavefield perpendicular to the direction of the propagation, in which the wavefield is still coherent. The transversal coherence length L_T depends on the size D of the source and distance R from the source

$$L_T = \frac{\lambda R}{2D}. \quad (2.12)$$

2.1.7 Synchrotron Radiation

Using coherent X-rays for imaging implies that these must be produced. For X-ray ptychography, the source of choice is a synchrotron radiation source, which can produce an intense flux of coherent X-ray photons. Details about the principles of synchrotron radiation can be found in [37]. The range of energy varies from

soft X-rays with wavelengths roughly between 1 nm and 10 nm to hard X-rays with wavelengths below 1 nm.

2.2 Ptychography

The information about ptychography in this section can be found in [39], if not otherwise noted.

Over the past years, ptychography has evolved to a reliable and stable imaging modality that produces reconstructions of various types of materials in 2D and 3D [1], [29], [40]–[42]. Additionally, ptychography reconstructs the illuminating wavefield, making ptychography a feasible tool for optics characterization [43]–[45].

A reason for the popularity of ptychography is a magnification beyond the resolution of conventional scanning X-ray microscopy methods. This is achieved by analyzing the 2D diffraction patterns, which measure the intensity at the detector. The intensity is the squared modulus of the incident wavefield and the phase information is lost. Ptychography reconstructs the amplitude and phase of the object and the illumination. The detector and a ptychographic reconstruction algorithm act as a virtual lens, thereby achieve a magnification that is limited by the resolvable scattering vectors \vec{q} in the diffraction pattern and not by the focal size of the X-ray optics.

In the following, it is described how the magnification of a ptychographic reconstruction can be calculated. The opening angle γ between the sample and the detector is

$$\gamma = \tan^{-1} \left(\frac{n_d d}{2s} \right), \quad (2.13)$$

in which the number of pixels along one dimension of the diffraction pattern is described by n_d and the length of one detector pixel is described by d . The distance between the sample and the detector is described by s . The length l of one pixel in a ptychographic reconstruction is then

$$l = \frac{\lambda}{2 \sin(\gamma)}. \quad (2.14)$$

The reconstruction pixel size l is the theoretical lower limit for the spatial resolution. The practical limit is given by maximum resolvable intensity at the scattering vector \vec{q} in the diffraction pattern.

The next section summarizes the general mathematical relations of the standard

ptychographic model. With these prerequisites, four ptychographic reconstruction algorithms are introduced: the extended Ptychographic Iterative Engine (ePIE), the refractive Ptychographic Iterative Engine (refPIE), the Difference Map (DM) and a custom algorithm denoted as parallel extended Ptychographic Iterative Engine (pePIE). Finally, the software used to perform all ptychographic reconstructions in this thesis is presented.

2.2.1 The Ptychographic Model

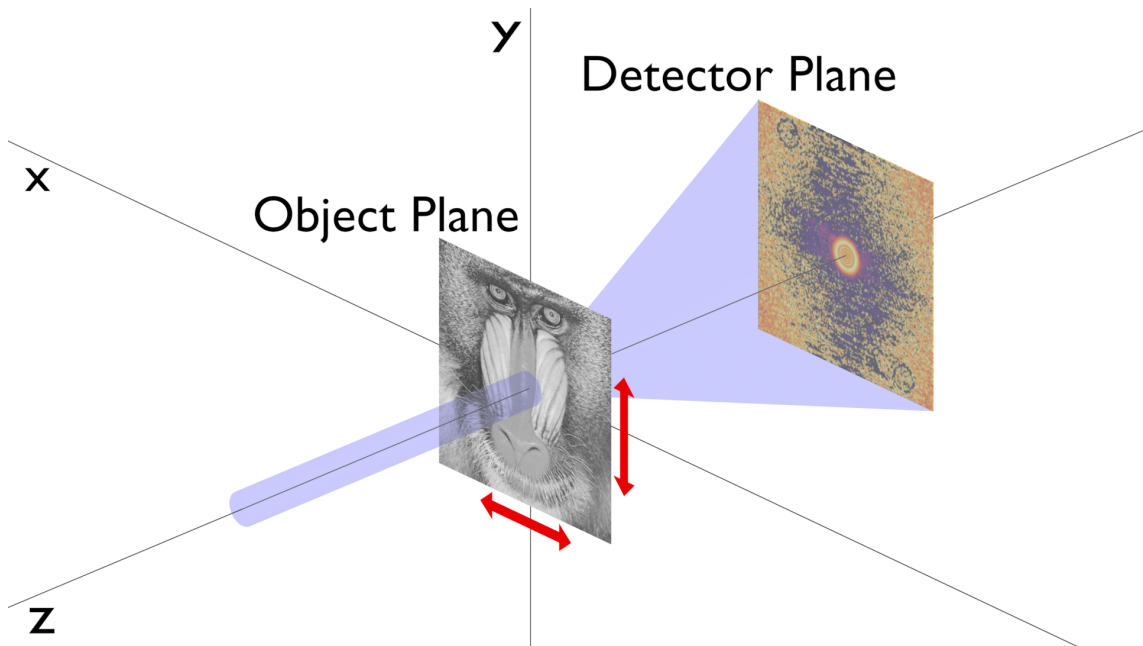


Figure 2.2: An illustration of the experimental procedure for the collection of a ptychographic dataset. The sample is scanned in the (x, y) plane. A coherent and spatially confined illumination propagates along the z axis and interacts with the sample. A 2D detector is located behind the sample to collect the diffraction patterns.

Ptychography aims to reconstruct the phase shift δ and amplitude decrease β of the sample, that is spatially resolved in 2D in the (x, y) plane. A schematic representation of an experimental setup is shown in figure 2.2. The sample is the Baboon test image. During the experiment, the sample is scanned in 2D in the (x, y) plane with a coherent and spatially confined illumination that propagates along the z direction. A 2D detector is located behind the sample to acquire the diffraction patterns that result of the interaction by the sample with the illumination.

A necessity for ptychography is that the illuminated regions of adjacent scan positions overlap, such that the resulting dataset has a certain degree of redundancy.

This is illustrated in figure 2.3. The amplitude and phase of the Baboon sample are shown in a) and d), respectively. The gaussian-shaped amplitude and gaussian-shaped phase of an example illumination is shown in b) and e), respectively. The red dots in a) mark the locations where the illumination is positioned and the illumination amplitude in b) has a red dot in the center for easier correlation.¹ The original object has a square shape with 510 px edge length, the illumination has a square shape with 256 px edge length. The object needs to be enlarged to the left, right, top, and bottom by half the illumination size. This is necessary to model the object illumination interaction at the edge regions of the object. The object and illumination in figure 2.3 a), b), d), and e) have the same pixel size. It is obvious, that the illuminated regions of adjacent scan positions overlap. Bunk, et al., recommend an overlap ratio of 60 % for reliable reconstructions [46].

The sample is represented by the so-called object-transmission function $O(x, y)$

$$O(x, y) = e^{-ik \int \delta(x, y, z) dz} e^{-k \int \beta(x, y, z) dz}, \quad (2.15)$$

in which $k = \frac{2\pi}{\lambda}$ is the wave vector, and δ and β are the real and imaginary part of the complex refractive index decrement, respectively. Both quantities must be integrated along the full propagation path through the material. The spatial coordinates (x, y) are now described by the vector \vec{r} . The illumination is represented by $P(\vec{r})$. Following the thin-object approximation, the interaction of O and P can be described by a multiplication

$$\psi_n(\vec{r}) = P(\vec{r})O(\vec{r} - \vec{r}_n). \quad (2.16)$$

Here, the index n has been introduced and denotes the shift \vec{r}_n of the object and the associated diffraction pattern I_n . The notation by n is valid throughout the entire thesis. The product of O and P represents the wavefield after the illumination P has interacted with the object O , and is described as the exit wavefield ψ_n .

In its essence, equation 2.16 represents the right side of equation 2.4, in which P denotes the first term and O the latter term.

¹Scan positions that lie on a perfect regular grid can cause an artifact in the ptychographic reconstruction. The artifact is commonly denoted as grid pathology and appears as a regular pattern throughout the object reconstruction. However, for the simulations done in this work, grid pathology has not been observed, such that it is fine to place the scan positions on a regular grid.

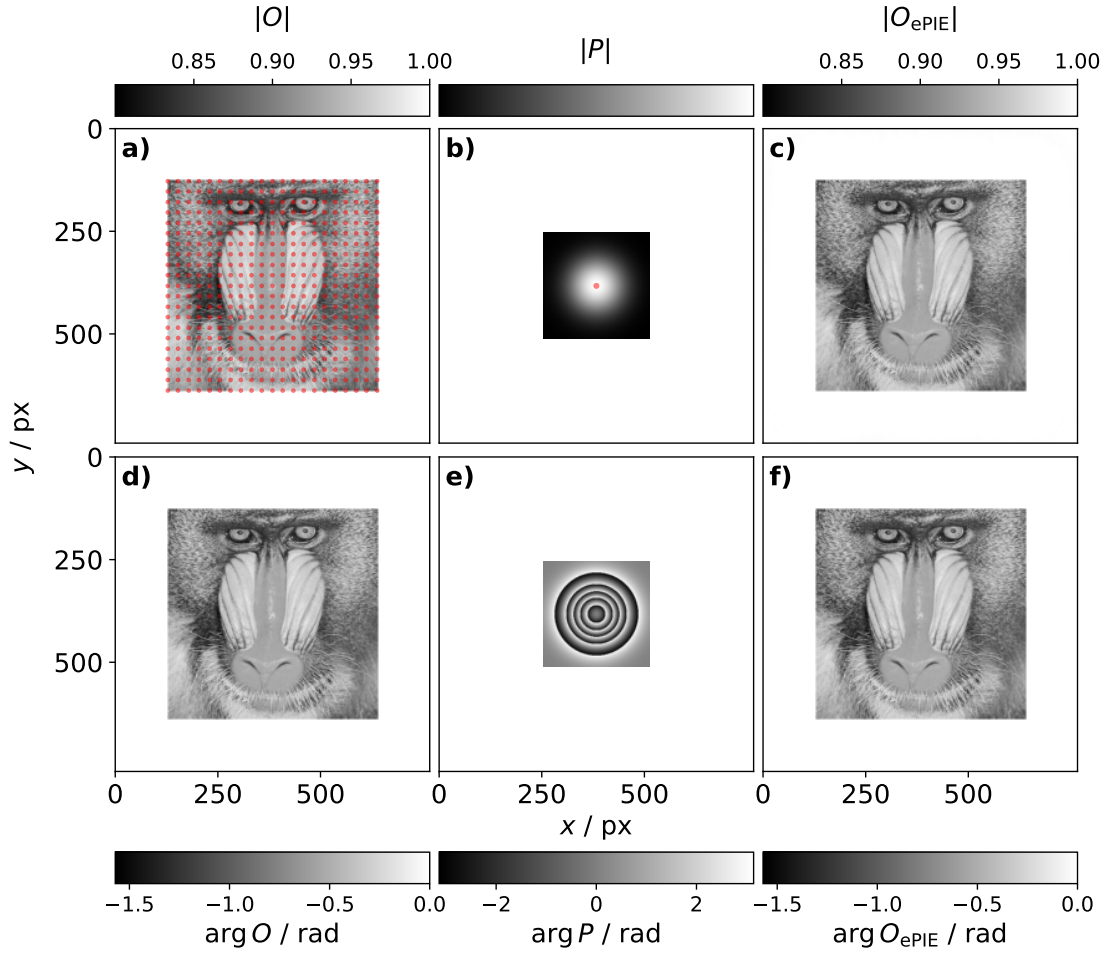


Figure 2.3: An illustration of the quantities that appear in ptychography. a) The amplitude of the exact object-transmission function. The red dots mark the scan positions \vec{r}_n . b) The amplitude of the illumination. The center of the illumination is marked by the red dot to easier correlate where the illumination is positioned in the object. c) The amplitude of an ePIE reconstruction of the object-transmission function. d) The phase of the exact object-transmission function. e) The gaussian-shaped phase of the illumination. f) The phase of an ePIE reconstruction of the object-transmission function. Some minor differences in the value range between the exact object in a) and d) and the reconstructed object in c) and f) can be seen. Overall, the contrast of the object is reconstructed very well.

The exit wavefield ψ_n can be propagated into the detector plane by

$$\Psi_n(\vec{q}) = \mathcal{F}[\psi_n(\vec{r})], \quad (2.17)$$

in which \mathcal{F} represents the Fourier transform for a propagation into the far-field.

All datasets evaluated in this thesis have a far-field experimental geometry. The propagated exit wavefield is denoted by Ψ_n and the reciprocal space coordinate is denoted the vector \vec{q} .

The diffraction patterns measure the intensities I_n that Ψ_n exerts on the detector. Mathematically, the amplitude is the square root of the intensity, so that the modulus of Ψ_n can be updated by

$$|\Psi'_n(\vec{q})| = \sqrt{I_n(\vec{q})}, \quad (2.18)$$

and the phases are kept unchanged. The updated propagated exit wavefield is denoted by Ψ'_n .

An afterwards backpropagation into the object plane is done

$$\psi'_n(\vec{r}) = \mathcal{F}^{-1}[\Psi'_n(\vec{q})], \quad (2.19)$$

in which ψ'_n denotes the updated exit wavefield and \mathcal{F}^{-1} denotes an inverse Fourier transform.

The steps so far represent the relations between the reconstructed and measured quantities and may appear somehow in all ptychographic algorithms that exist. How these relations are used to determine the object O and the illumination P depends on the algorithm. Nowadays, there exist a lot of ptychographic algorithms [47]–[60]. Four of those are presented in the next sections.

2.2.2 extended Ptychographic Iterative Engine

The extended Ptychographic Iterative Engine (ePIE) has been introduced by Maiden and Rodenburg in 2009 [50] and is an extension of the Ptychographic Iterative Engine (PIE) [47]. The problem with PIE is that it is not able to reconstruct the illumination P . However, ePIE is able to recover the probe. The procedure is a cycling through the diffraction patterns I_n in a random order. For each diffraction pattern, the steps in equation 2.16 to 2.19 are pursued and after the backpropagation, the object O and illumination P are updated by

$$O'(\vec{r} - \vec{r}_n) = O(\vec{r} - \vec{r}_n) + \alpha \frac{P^*(\vec{r})}{\|P(\vec{r})\|_{\max}^2} (\psi'_n(\vec{r}) - \psi_n(\vec{r})), \quad (2.20)$$

$$P'(\vec{r}) = P(\vec{r}) + \beta \frac{O^*(\vec{r} - \vec{r}_n)}{\|O(\vec{r} - \vec{r}_n)\|_{\max}^2} (\psi'_n(\vec{r}) - \psi_n(\vec{r})). \quad (2.21)$$

The updated object and illumination are denoted by O' and P' , respectively. The complex conjugates of P and O are denoted by P^* and O^* , respectively. The denominator in the second terms denotes an euclidian norm. The factors α and β denote the update strengths and can be set by the user. One iteration of the ePIE algorithm consists of a cycling through all diffraction patterns. The reconstruction is iterated until O and P converge.

An example ePIE reconstruction of the Baboon test dataset is shown in figure 2.3 c) and f). The object is reconstructed very well. Some minor differences in the value range can be identified, but the contrast of the reconstruction matches the original object in a) and d).

2.2.3 refractive Ptychographic Iterative Engine

The refPIE has been introduced by Wittwer, et al. [52]. In contrast to the before introduced ePIE, refPIE directly reconstructs the complex refractive index decrement ν and not the object-transmission function O . This is beneficial, since the phase shift δ of ν is not 2π periodic and thicker objects can be reconstructed without the common problem of phase wraps. The precise derivation of the refPIE can be obtained from [61] and [52]. Here, only the equations are restated that are necessary to implement the refPIE.

For the processing of one diffraction pattern, the first step is the calculation of the object-transmission function O

$$O(\vec{r}) = e^{ik\nu(\vec{r})}. \quad (2.22)$$

Then, the steps of equations 2.16 to 2.19 are performed. The major difference of refPIE comes now regarding the update of the refractive index decrement ν and the illumination P . The equations are

$$\nu'(\vec{r} - \vec{r}_n) = \nu(\vec{r} - \vec{r}_n) + \frac{\alpha}{k} \frac{(i\psi_n(\vec{r}))^*}{|\psi_n(\vec{r})|_{\max}^2} (\psi'_n(\vec{r}) - \psi_n(\vec{r})), \quad (2.23)$$

$$P'(\vec{r}) = P(\vec{r}) + \beta \frac{e^{-ik\nu^*(\vec{r}-\vec{r}_n)}}{|e^{ik\nu(\vec{r}-\vec{r}_n)}|_{\max}^2} (\psi'_n(\vec{r}) - \psi_n(\vec{r})), \quad (2.24)$$

in which ν' denotes the updated complex refractive index decrement. The refPIE procedure is similar to ePIE: One iteration consists of performing the before mentioned steps for every diffraction pattern. The diffraction patterns are processed in a random order. The reconstruction is iterated until ν and P converge.

2.2.4 Difference Map

Thibault, et al., introduced the Difference Map (DM) algorithm for ptychography in 2009 [51]. During that time, ePIE did not exist yet. The DM algorithm is capable of recovering the probe and hence, the DM in the application of ptychography is seen as a milestone [39]. The DM algorithm differs significantly from the before introduced ePIE and refPIE. It is a projection based algorithm that processes all diffraction patterns simultaneously. Each diffraction pattern I_n is associated with an exit wavefield ψ_n . All exit wavefields are summarized in the state vector Φ .

$$\Phi = \psi_1, \psi_2, \dots, \psi_N \quad (2.25)$$

The DM procedure considers two projections: First, the Fourier projection Π_F that replaces the modulus in each exit wavefield ψ_n by the square root of the diffraction patterns I_n

$$\Pi_F(\psi_n) = \mathcal{F}^{-1}(\sqrt{I_n} e^{i \arg(\mathcal{F}(\psi_n))}). \quad (2.26)$$

Second, the real space projection Π_O , allowing to factorize the exit wavefield ψ_n into the object O and the illumination P .

$$\Pi_O(\psi_n) = P(\vec{r})O(\vec{r} - \vec{r}_n). \quad (2.27)$$

The real space projection can be carried out numerically, by varying O and P , so that the following equation is minimized

$$\|\psi(\vec{r}) - \psi^0(\vec{r})\|^2 = \sum_n \sum_r |\psi_n(\vec{r}) - P(\vec{r})O(\vec{r} - \vec{r}_n)|^2. \quad (2.28)$$

Alternatively, a gradient-based determination of the real space constraint can be done

$$O'(\vec{r} - \vec{r}_n) = \frac{\sum_n P^*(\vec{r})(\psi_n(\vec{r}))}{\sum_n |P(\vec{r})|^2}, \quad (2.29)$$

$$P'(\vec{r}) = \frac{\sum_n O^*(\vec{r} - \vec{r}_n)(\psi_n(\vec{r}))}{\sum_n |O(\vec{r} - \vec{r}_n)|^2}. \quad (2.30)$$

With these projections, the iterative procedure follows

$$\Phi_{i+1} = \Phi_i + \Pi_F(2\Pi_O(\Phi_i) - \Phi_i) - \Pi_O(\Phi_i), \quad (2.31)$$

in which i denotes the iteration index. The reconstruction is iterated until Φ converges.

2.2.5 parallel extended Ptychographic Iterative Engine

The parallel extended Ptychographic Iterative Engine (pePIE) follows the ePIE, except that the object O and the illumination P are updated by all diffraction patterns simultaneously

$$O'(\vec{r}) = O(\vec{r}) + \sum_n \frac{P^*(\vec{r} + \vec{r}_n)(\psi'_n(\vec{r}) - \psi_n(\vec{r}))}{\sum_n |P(\vec{r} + \vec{r}_n)|^2}, \quad (2.32)$$

$$P'(\vec{r}) = P(\vec{r}) + \sum_n \frac{O^*(\vec{r} - \vec{r}_n)(\psi'_n(\vec{r}) - \psi_n(\vec{r}))}{\sum_n |O(\vec{r} - \vec{r}_n)|^2}. \quad (2.33)$$

The notable difference is the denominator. While in the ePIE updates in equations 2.20 and 2.21, the denominator is given as the maximum value of the squared modulus, here, the denominator is just the squared modulus.

The pePIE can yield smoother reconstructions. This is due to the simultaneous refinement against all diffraction patterns, such that the reconstructed object is less influenced by local changes of individual diffraction pattern. Typically, the pePIE is applied after a regular ePIE reconstruction.

The simultaneous processing of the diffraction patterns is a similarity to DM. However, the pePIE is a different algorithm than DM and follows a very different procedure.

2.2.6 Software

Nowadays, there exists a variety of software to do ptychography [62]–[70]. Although such a great amount of software is available, it is still common that experimentalists implement their own reconstruction procedures. All developments in this work are implemented to the software `ptycho`. It is a custom software that exists for more than a decade. The software is written in C++. It has been developed and extended by several researchers in the past. The most thorough explanation of it is given by

Robert Hoppe in his PhD thesis [71].

All calculations are performed on a GPU. The mathematical operations are implemented by the utilization of the CUDA software, so that `ptycho` can only run on Nvidia GPUs. The majority of the matrix operations are implemented with custom written kernels. In some cases, Thrust is used to implement simple mathematical operations. The Fourier transform is utilized from the CuFFT library. By the time of writing this thesis, `ptycho` runs on a single GPU and has no options to use multiple GPUs.

The three ptychographic reconstruction algorithms ePIE, refPIE, and pePIE can be utilized with `ptycho`. At this point, a misconception is discussed. In the configuration file of `ptycho` and in PhD thesis of Robert Hoppe, the pePIE is denoted as DM [71]. The pePIE and the DM have the similarity that both process all diffraction patterns simultaneously. However, the DM is a different algorithm that may give different results as pePIE. This misconception has propagated to mistakes in existing publications, such as the authors contribution to the SPIE Conference Proceedings in 2022 [72].

Further features of `ptycho` are constraining of the reconstructed object O by its amplitude and phase, constraining the reconstructed illumination amplitude $|P|$, momentum acceleration [49], background correction [71], multi-beam [73], [74], up-scaling [75], multi-slicing [76], [77] and the utilization of a beamstop. Furthermore, `ptycho` can refine the scan positions during the reconstruction, which is described in more detail in section 2.2.6 [78].

The described features make `ptycho` a reliable software to reconstruct the datasets acquired at the Ptychographic Nano-Analytical Microscope (PtyNAMI) [22] at the nanoprobe endstation of beamline P06 [79], PETRA III, Deutsches Elektronen-Synchrotron (DESY).

Position Refinement

Scan position refinement is an essential part of ptychography, especially when the microscope cannot yield a stability similar to the resolution of the ptychographic reconstruction. There are several well established approaches for position refinement [80]–[82].

The scan position refinement used in this work is a custom procedure by Schropp, et al., and has been briefly mentioned in [78]. The approach is a brute-force attempt to find the scan position \vec{r}_n that matches best the corresponding measured diffraction pattern I_n .

For a given scan position \vec{r}_n , a set of positions \vec{r}_p around \vec{r}_n is set up. For each \vec{r}_p , the least squares error $\epsilon_{n,p}$ is calculated by the following:

$$\epsilon_{n,p} = \sum_{\vec{q}} |I_n(\vec{q}) - |\mathcal{F}\{P(\vec{r})O(\vec{r} - \vec{r}_n - \vec{r}_p)\}|^2|^2 \quad (2.34)$$

The refinement minimizes $\epsilon_{n,p}$ to determine the position shift \vec{r}_p . The scan position \vec{r}_n is then updated by

$$\vec{r}_n = \vec{r}_n + \vec{r}_p. \quad (2.35)$$

The set of positions \vec{r}_p is specified as a square grid with the spread r_p . For $r_p = 1$, the x_p and y_p components of the set of \vec{r}_p are $x_p = y_p = \{-1, 0, 1\}$, such that 9 different \vec{r}_p are utilized in total. A $r_p = 2$ gives 25 different \vec{r}_p , and so forth.

2.3 Tomography

The information about tomography in this section can be found in [83], if not otherwise noted. Additionally, some of the figures have been created with inspiration from [7].

Tomography describes the full spatial reconstruction of an object f from a set of projections D_Ω . A projection is an integrated view of the object from a specific perspective. In section 2.3.1, the general mathematical relations of tomography are given. Section 2.3.2 introduces the concept of a sinogram, which is a useful description especially for parallel-beam tomography, the type of tomography treated in this thesis. A first illustrative approach to solve the tomographic problem, referred to as the standard Backprojection (BP), is introduced in section 2.3.3, and it will be shown that this approach creates artifacts in the reconstructed object. Hence, in section 2.3.4, the Filtered Backprojection (FBP) along with the Fourier slice theorem is introduced, which explains the artifacts caused by the BP and gives an analytical solution of the tomographic problem. In sections 2.3.5 and 2.3.6, two popular numeric approaches for solving the tomographic problem are introduced, the Simultaneous Iterative Reconstruction Technique (SIRT) and the Conjugate Gradient Least Squares (CGLS).

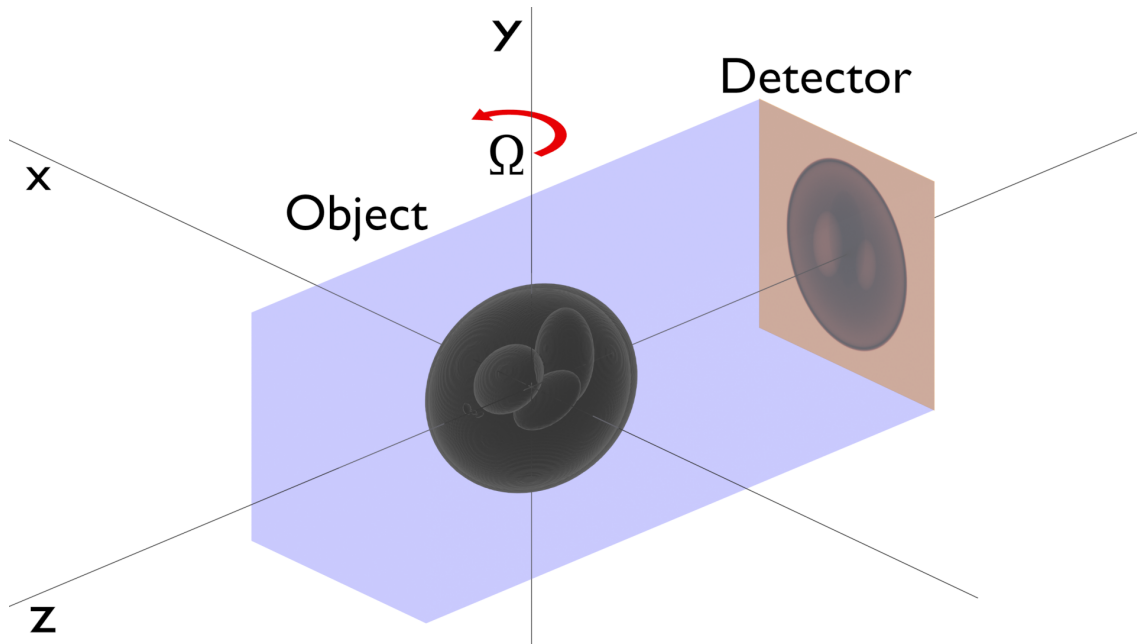


Figure 2.4: A schematic drawing of the data acquisition of full-field parallel-beam absorption tomography. The sample is a 3D Shepp Logan phantom. The illumination is shown in blue and consists of photons that are all directed perfectly parallel. Behind the sample is a 2D detector located that captures the resulting projection. During the experiment, either the sample, or the illumination and the detector, are rotated around the y -axis by the angle Ω .

2.3.1 The Tomographic Model

In this work, tomography is only done in parallel-beam geometry. A schematic drawing of a parallel-beam absorption tomography experiment is shown in figure 2.4. The sample is a 3D Shepp Logan phantom. The illumination is drawn in blue and propagates along the z -axis. Parallel-beam tomography means that all photons of the illumination are directed perfectly parallel. A 2D detector is located behind the sample and collects the projections that result due to the absorption of the sample with the illumination. During the data acquisition, either the sample, or the illumination and the detector, are rotated around the y -axis by the angle Ω .

Tomography can be done in 2D and 3D. For parallel-beam tomography, the 3D reconstruction is just a set of 2D reconstructions in the (x, z) plane. The explanation given here is for 2D only and the y coordinate is moved to the subscript of the object f_y and the projection $D_{y,\Omega}$.

Consider the object $f_y(x, z)$ visible in figure 2.5 a), this is one of the central (x, z) slices of the Shepp Logan phantom in figure 2.4. The reconstruction of this object

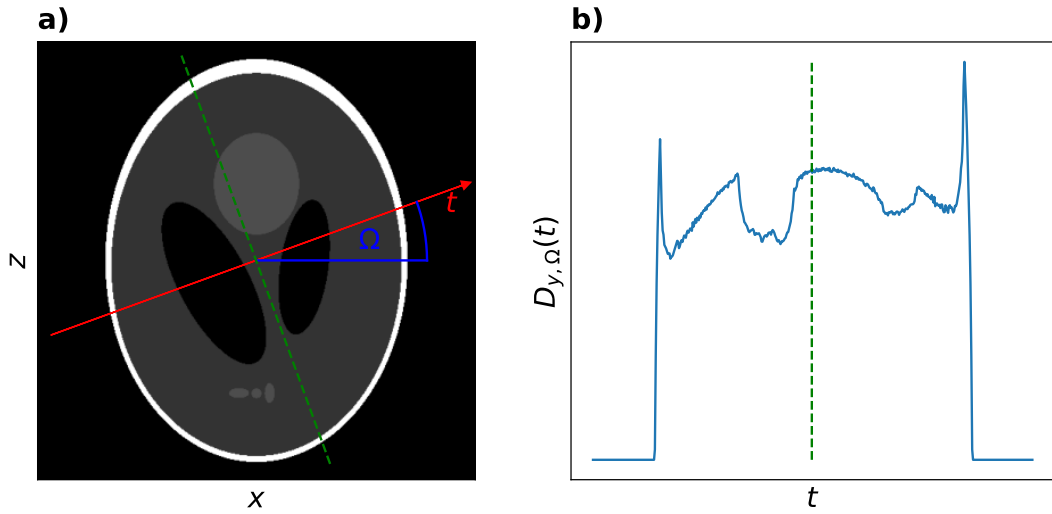


Figure 2.5: An illustration how a projection $D_{y,\Omega}$ is calculated from the object $f_y(x, z)$. Every projection is associated with the projection angle Ω . In this illustration, the surrounding frame is rotated. The red line in the left image marks the projection axis t after rotating around Ω . For each value of t , the line integral marked by the dashed green line is calculated. The right image shows the resulting projection.

$f_y(x, z)$ is exactly the aim of tomography. However, the only information available are the projections $D_{y,\Omega}$. One projection $D_{y,\Omega}$ for $\Omega = 30^\circ$ is shown in figure 2.5 b). The projection angle Ω is marked in blue in figure 2.5 a). From here on, it is assumed that it is the illumination and detector that is rotated, and the object stays fixed. The projection is a set of line integrals. The position of the line integral in the projection is specified by the projection coordinate t , which is calculated by

$$t = x \cos \Omega + z \sin \Omega. \quad (2.36)$$

The axis of the projection coordinate t is shown in red in figure 2.5 a). The line integral is calculated by

$$D_{y,\Omega}(t) = \int_{(\Omega,t)} f_y(x, z) ds, \quad (2.37)$$

in which s denotes the path of the line, i.e. the dashed green line in figure 2.5 a).²

²For the absorption tomography setup depicted here, the projections measure the transmission. The transmission is not linearly integrable over the object space, such that equation 2.37 is violated and the transmission is not suitable for a tomographic reconstruction. However, the absorption β can be calculated from the transmission using the Lambert-Beer law and β is linearly integrable over the object space.

A more convenient description is obtained by replacing the integration variable s with (x, z) . This can be done utilizing a delta-function $\tilde{\delta}$ and the definition of t in equation 2.36.³

$$D_{y,\Omega}(t) = \int_{-\infty}^{+\infty} \int_{-\infty}^{+\infty} f_y(x, z) \tilde{\delta}(t - (x \cos(\Omega) + z \sin(\Omega))) dx dz \quad (2.38)$$

This expression has been introduced by Johann Radon and is called the Radon transformation [84]. The equation describes how a projection $D_{y,\Omega}(t)$ is created from the real object $f_y(x, z)$ under a certain projection angle Ω . Equation 2.38 describes the forward process, however, the scientific interested is in the backward process. The backward process meets exactly the problem that has been depicted so far, namely the reconstruction of an object $f_y(x, z)$ from a set of projections $D_{y,\Omega}$.

2.3.2 Sinogram

A sinogram is the measured projection $D_{y,\Omega}$ drawn against the projection angle Ω . The sinogram for the Shepp Logan phantom for an angular range of 180° is shown in figure 2.6. For parallel-beam tomography, the sinogram contains all information necessary to reconstruct the object $f_y(x, z)$. This makes the sinogram a feasible tool when assessing the quality of a tomographic dataset. In figure 2.6, the visible structures are very smooth without any discontinuities, indicating the good quality of the test dataset.

2.3.3 Standard Backprojection

A concept is now introduced which is referred to as the standard Backprojection (BP). It is an illustrative attempt to solve the tomographic problem, but it is stressed that it is not a solution. Nevertheless, it will have an impact for the developments in chapter 5.

Each $D_{y,\Omega}$ is simply put back into $f_y(x, z)$ with the definition of t

$$f_y(x, z) = \int_0^{2\pi} \int_{-\infty}^{+\infty} D_{y,\Omega}(t) \tilde{\delta}(t - (x \cos(\Omega) + z \sin(\Omega))) dt d\Omega. \quad (2.39)$$

One realizes that this approach is ambiguous. Following the definition of $D_{y,\Omega}$ in

³The delta function is denoted by $\tilde{\delta}$ and not δ . The δ symbol already denotes the phase shift of the complex refractive decrement ν in equation 2.5.

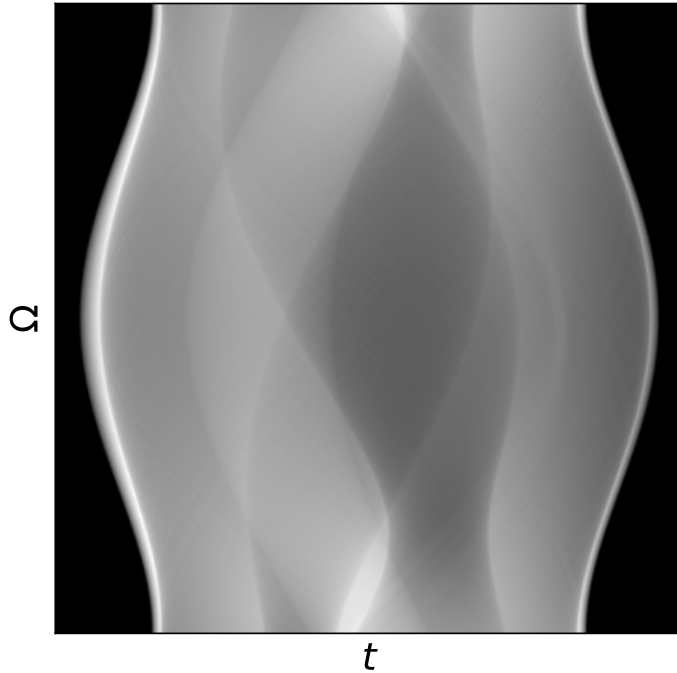


Figure 2.6: The sinogram of the Shepp Logan test dataset. The projection coordinate t is given on the horizontal axis and the projection angle Ω is given on the vertical axis. For parallel-beam geometry, the sinogram contains all information to perform the tomographic reconstruction of $f_y(x, z)$.

equation 2.38, the integration is happening over x and z , and hence, $D_{y,\Omega}$ has no information which pixels in $f_y(x, z)$ actually contribute to $D_{y,\Omega}$. This means that a pixel in $D_{y,\Omega}$ is reconstructed as a straight line in $f_y(x, z)$. However, since there is not only a single $D_{y,\Omega}(t)$, but a series for different Ω , many lines are drawn and overlap, so that it is possible to reconstruct an approximation of $f_y(x, z)$. The result of the standard BP for the sinogram in figure 2.6 is shown in figure 2.7. The reconstructed object can be identified, but comparing the original image in figure 2.5 a) and the reconstruction in figure 2.7 clearly shows that the reconstruction is blurred. The blurring is a natural result of the standard BP. In the next section, the FBP is introduced, which description explains why the blurring occurs.

2.3.4 Filtered Backprojection

The Filtered Backprojection (FBP) is an analytic solution to the tomographic problem and is derived in this section. The derivation is started by introducing the Fourier Slice Theorem, which states that the Fourier transform of a projection is

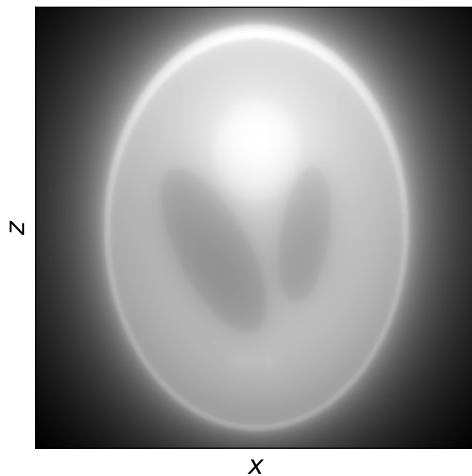


Figure 2.7: A reconstruction of the Shepp Logan test dataset using the BP. The reconstruction is significantly blurred.

the same as a line rotated by Ω in the 2D Fourier transform of the object. The Fourier transform of the projection $D_{y,\Omega}$ is calculated by

$$S_{y,\Omega}(q) = \int_{-\infty}^{\infty} P_{y,\Omega}(t) e^{-i2\pi qt} dt, \quad (2.40)$$

in which $S_{y,\Omega}$ denotes the Fourier transformed projection and q denotes the spatial frequency corresponding to t . The 2D Fourier transform of the object F_y is given by

$$F_y(u, w) = \int_{-\infty}^{+\infty} \int_{-\infty}^{+\infty} f_y(x, z) e^{-i2\pi(ux+wz)} dx dz, \quad (2.41)$$

in which (u, w) are the spatial frequencies that correspond to the spatial coordinates (x, z) . The frequencies (u, w) can be calculated from (q, Ω) by

$$u = q \cos(\Omega), \quad (2.42)$$

$$w = q \sin(\Omega). \quad (2.43)$$

Figure 2.8 a) shows the Fourier transformed projection $S_{y,\Omega=30^\circ}$ drawn in the 2D frequency space of the object. When performing this step for a sufficient amount of projections with different Ω , then the Fourier space is sufficiently sampled and the object $f_y(x, z)$ can be determined by calculating the inverse 2D Fourier transform

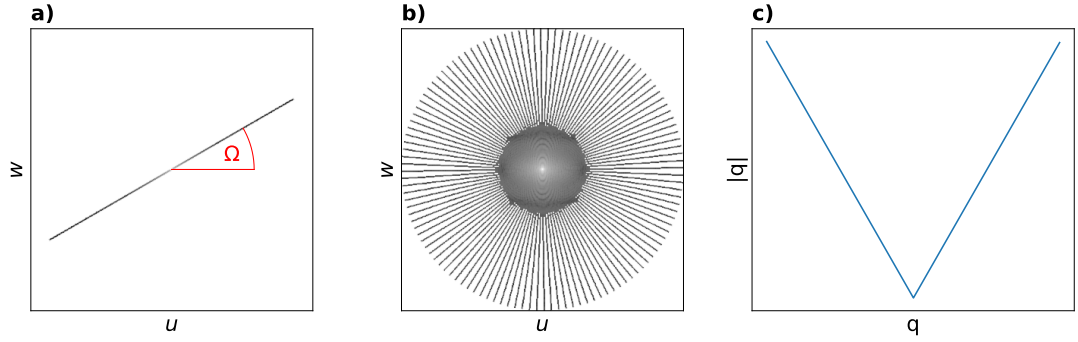


Figure 2.8: a) A Fourier transform of one projection $S_{y,\Omega}(q)$ drawn in the frequency space of the object. b) The Fourier transforms of 60 projections over an angular range of 180° . c) The ramp filter $|q|$ used as the filter in Fourier space for the FBP.

of $F_y(u, w)$

$$f_y(x, z) = \int_{-\infty}^{+\infty} \int_{-\infty}^{+\infty} F_y(u, w) e^{i2\pi(ux+wz)} du dw. \quad (2.44)$$

To derive the FBP, equation 2.44 needs to be reformulated to utilize the projections $S_{y,\omega}$ instead of F_y . Since the projections in frequency space are defined by (q, Ω) , polar coordinates are introduced into equation 2.44. With the relations in equation 2.42 and 2.43, the integration variables can be rephrased to

$$du dw = q dq d\Omega. \quad (2.45)$$

Inserting equation 2.42, 2.43 and 2.45 into equation 2.44 gives

$$f_y(x, z) = \int_0^{2\pi} \int_0^{+\infty} F_y(q, \Omega) e^{i2\pi q(x \cos(\Omega) + z \sin(\Omega))} q dq d\Omega, \quad (2.46)$$

In the following, a reformulation of equation 2.46 is applied that explains why the blurring occurs and why an angular range of 180° is sufficient to reconstruct a parallel-beam tomography dataset. With basic trigonometry, equation 2.46 can be

rephrased to

$$f_y(x, z) = \int_0^\pi \int_{-\infty}^{+\infty} F_y(q, \Omega) |q| e^{i2\pi q(x \cos(\Omega) + z \sin(\Omega))} dq d\Omega. \quad (2.47)$$

The reformulation can be found in [83] in smaller steps and with more details.

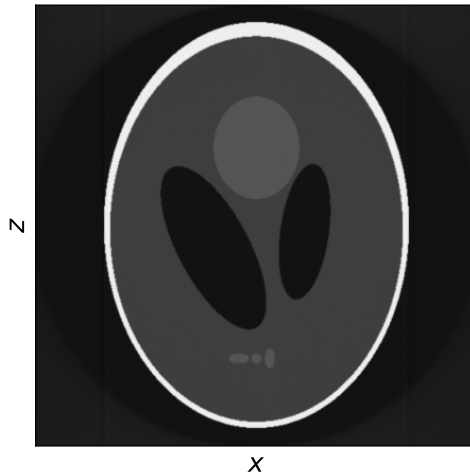


Figure 2.9: The FBP reconstruction of the Shepp Logan test dataset. In contrast to the BP reconstruction, the FBP reconstruction is not blurred.

Now, without any loss of generality, $F_y(q, \Omega)$ can be replaced by $S_{y,\Omega}(q)$, yielding

$$f_y(x, z) = \int_0^\pi \int_{-\infty}^{+\infty} S_{y,\Omega}(q) |q| e^{i2\pi qt} dq d\Omega. \quad (2.48)$$

This is the analytic inversion of equation 2.37 and known as the inverse Radon transformation. It states that the object $f_y(x, z)$ can be reconstructed from an infinite amount of Fourier transformed projections $S_{y,\Omega}(q)$ over an angular range of 180° . What is different to the standard BP in equation 2.39 is the filtering by the factor $|q|$, which is known as the ramp filter and shown in figure 2.8 c). The necessity of this operation is due to the fact that the low spatial frequencies are much higher sampled than the high spatial frequencies, which can be seen in figure 2.8 b). While the central low frequency regions are already densely sampled for an amount of only 60 projections, the outer high frequency regions are not dense sampled at all. The oversampling of the low spatial frequencies causes the blurring visible in the BP reconstruction in figure 2.7. Smooth features correspond to lower spatial frequen-

cies and sharp features to higher spatial frequencies. The filtering by $|q|$ equalizes the sampling of the low and high spatial frequencies, such that the FBP yields a properly reconstructed object $f_y(x, z)$ shown in figure 2.9.

In the next sections, two iterative tomographic reconstruction algorithms are introduced: the SIRT and the CGLS.

2.3.5 Simultaneous Iterative Reconstruction Technique

The iterative approaches are also described as algebraic approaches, because they solve the tomographic problem as a set of linear equations. In contrast to the analytic description of the BP and FBP in section 2.3.3 and 2.3.4, respectively, the algebraic approaches solve the tomographic problem on a finite pixel grid. The finiteness of the object and projection space is always given for experimental datasets, due to the fact that detectors contain a pixel array by which the projections are acquired.

First, the forward projection in equation 2.38 is reformulated for finite sizes

$$D_{y,\Omega,t} = \sum_x \sum_z f_{y,x,z} \Theta_{\Omega,t,x,z}. \quad (2.49)$$

To calculate the forward projection, the entire object f is iterated. The coordinates (x, z) are now the positions on the pixel grid and hence, the integrals have been replaced by sums. The delta function $\tilde{\delta}$ has been replaced by a 4D matrix Θ , that relates which pixel $f_{y,x,z}$ of the object constitutes to which value $D_{y,\Omega,t}$ in the projection.

Consider the ray paths shown in figure 2.10. The yellow path is well aligned with the coordinate system, which refers to $\Omega = 0^\circ$. The most left position of the yellow ray path refers to $t = 0$. This gives $\Theta_{\Omega,t,x,z} = 1$ for all z with $x = 0$. All positions with $z > 0$ have $\Theta_{\Omega,t,x,z} = 0$.

The situation is more complicated for ray paths that are not well aligned with the coordinate system, such as the green path in figure 2.10. The exact fractional area of a specific pixel in the ray path is denoted as A^{ray} , such as the black marked area in figure 2.10. The total area of one pixel is denoted by A^{pixel} . The value $\Theta_{\Omega,t,x,z}$ can be calculated by

$$\Theta_{\Omega,t,x,z} = \frac{A_{\Omega,t,x,z}^{\text{ray}}}{A^{\text{pixel}}}. \quad (2.50)$$

However, the exact calculation of $A_{\Omega,t,x,z}^{\text{ray}}$ is tedious and $\Theta_{\Omega,t,x,z}$ is often approximated. The procedure of SIRT is as follows.

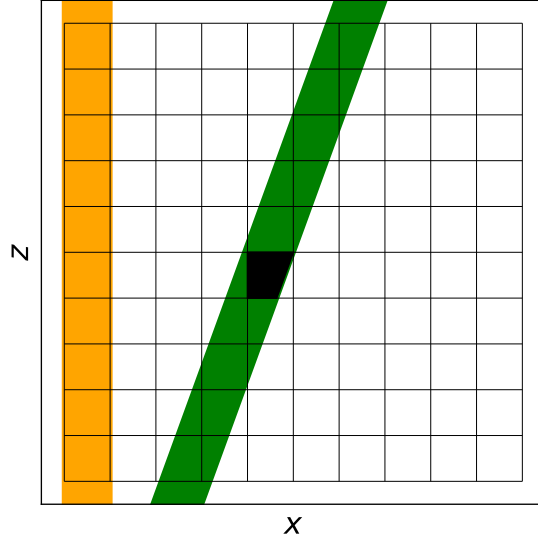


Figure 2.10: An illustration of the ray paths in tomography. The yellow path is perfectly aligned with the coordinate system and the weights $\Theta_{\Omega,t,x,z}$ can be calculated trivially. The green ray path is misaligned with the coordinate system and the calculation of $\Theta_{\Omega,t,x,z}$ is more elaborate. The black area must be calculated to determine the exact $\Theta_{\Omega,t,x,z}$.

A forward projection $\vec{G}_{y,\Omega}$ of the reconstructed object \mathbf{f}_y is done using equation 2.49. The difference between the measured projection $\vec{D}_{y,\Omega}$ and $\vec{G}_{y,\Omega}$ is calculated, which is then backprojected into the reconstructed object \mathbf{f}_y . The key criteria of SIRT is that the object is only updated by the average difference obtained from all projections.⁴ Putting this into one equation gives the following

$$f_{y,x,z}^{l+1} = f_{y,x,z}^l + \sum_{\Omega,t} \frac{D_{y,\Omega,t} - G_{y,\Omega,t}}{\sum_{\Omega,t} \Theta_{\Omega,t,x,z}^2} \Theta_{\Omega,t,x,z}, \quad (2.51)$$

in which the superscript l denotes the iteration index. The numerator is normalized by the the sum of the squared weights $\Theta_{\Omega,t,x,z}^2$ of the respective object pixel $f_{y,x,z}$.

A converged reconstruction utilizing SIRT of the Shepp Logan test dataset is shown in figure 2.11. The Shepp Logan phantom is reconstructed very well.

⁴Performing the update of the object \mathbf{f}_y after each projection pixel would yield the Algebraic Reconstruction Technique (ART) algorithm. Performing the update of the object after all pixels of one projection yields the Simultaneous Algebraic Reconstruction Technique (SART) algorithm. [83]

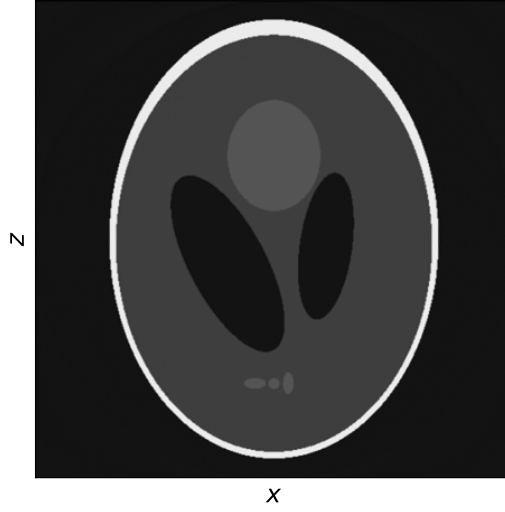


Figure 2.11: The SIRT reconstruction of the Shepp Logan test dataset of 1000 iterations.

2.3.6 Conjugate Gradient Least Squares

Lastly, the CGLS algorithm is introduced as another iterative approach to address the tomographic problem. The description is reproduced from [85]. The tomographic problem first needs to be reformulated to

$$\mathbf{A}\vec{c} = \vec{b}, \quad (2.52)$$

in which \vec{c} is a 1D vector representing the flattened reconstructed image \mathbf{f}_y , \vec{b} is a 1D vector holding the pixel values of all projections \mathbf{D}_y . The 2D matrix \mathbf{A} relates the pixels in the flattened reconstructed image \vec{c} to the pixels in projections \vec{b} , similar as Θ does in section 2.3.5.

Having the tomographic problem properly formulated in equation 2.52, the CGLS algorithm proceeds as follows:

First, an initial guess \vec{c}_0 of the solution vector \vec{c} is done. If no prior knowledge about \vec{c} is known, then \vec{c}_0 can be zero. Two more vectors are introduced, the residual \vec{r} and the step \vec{d} . Both have an initial guess \vec{r}_0 and \vec{d}_0 , which are calculated by the following

$$\vec{d}_0 = \vec{r}_0 = \vec{b} - \mathbf{A}\vec{c}_0. \quad (2.53)$$

Next, the gradient $\vec{\alpha}$ of the conjugated residual \vec{r} is calculated

$$\vec{\alpha}_i = \frac{\vec{r}_i^T \vec{r}_i}{\vec{d}_i^T \mathbf{A} \vec{d}_i}, \quad (2.54)$$

which is the reason why the algorithm is called Conjugate Gradient Least Squares. With $\vec{\alpha}$, the object \vec{c} is updated by

$$\vec{c}_{i+1} = \vec{c}_i + \vec{\alpha}_i \vec{d}_i. \quad (2.55)$$

The new residual \vec{r}_{i+1} is then calculated by

$$\vec{r}_{i+1} = \vec{r}_i - \vec{\alpha}_i \mathbf{A} \vec{d}_i. \quad (2.56)$$

And, the new step \vec{d}_{i+1} is calculated by

$$\vec{d}_{i+1} = \vec{r}_{i+1} + \frac{\vec{r}_{i+1}^T \vec{r}_{i+1}}{\vec{r}_i^T \vec{r}_i} \vec{d}_i. \quad (2.57)$$

The algorithm is iterated until the reconstruction converges.

2.3.7 Software

All tomographic operations within this work are done utilizing the ASTRA-Toolbox, which is an open source library dedicated to perform tomographic reconstructions [86]. Although most commonly used by either Python or Matlab bindings, its functionalities are written in C++/CUDA.

The ASTRA-Toolbox provides parallel-beam and cone-beam geometry in 2D and 3D. Throughout this work, only the parallel-beam geometry is applicable. The applicable GPU-accelerated 3D reconstruction algorithms are the standard BP, the SIRT, and the CGLS. The algorithms run on a single GPU.⁵

⁵Distributing parallel-beam tomography on multiple GPUs is trivial. The object \mathbf{f} and the projections \mathbf{D}_Ω can be easily split up and distributed among several GPUs.

2.4 Ptychographic Tomography

After ptychography and tomography have been introduced in sections 2.2 and 2.3, respectively, this section is dedicated to the combination of ptychography and tomography. In section 2.4.1, it is elaborated how a ptychographic tomographic dataset is acquired. The first reconstruction approach is introduced in section 2.4.2 and is the straight-forward and intuitive approach for combining ptychography and tomography. It does a two-step procedure, which first reconstructs a set of ptychographic projections, that are used for an afterwards tomographic reconstruction. Section 2.4.3 introduces a more recent approach that has been introduced in 2017 and formulates the ptychographic tomographic reconstruction as a single mathematical description [28].

2.4.1 Data Acquisition

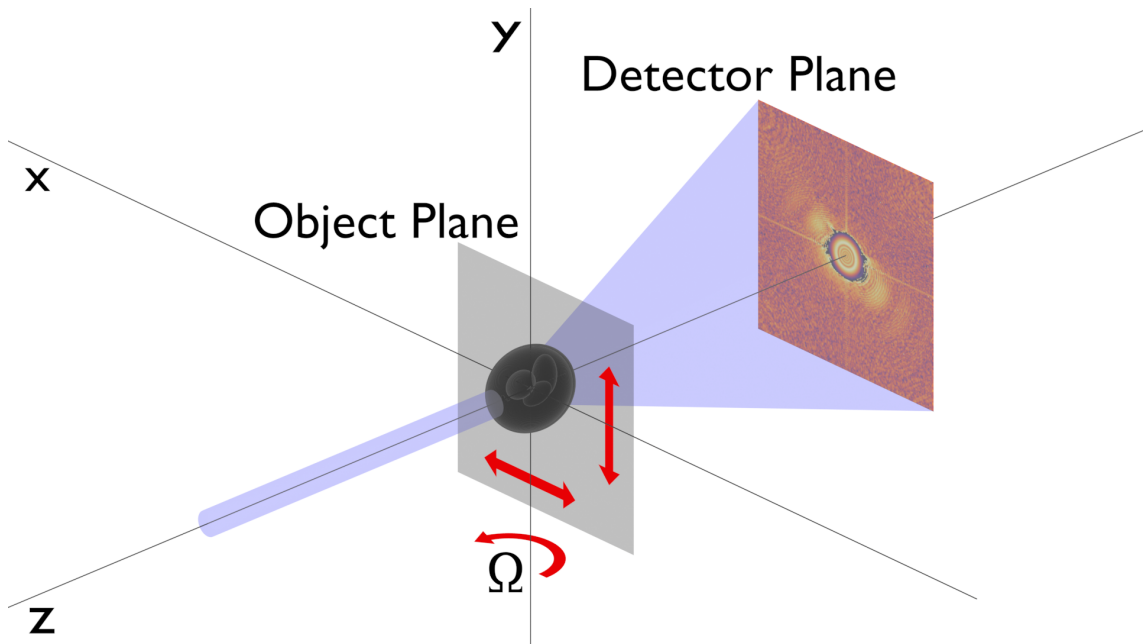


Figure 2.12: An illustration of the experimental setup for ptychographic tomography. The sample is a 3D Shepp Logan phantom. The illumination propagates along the z dimension and interacts with the sample. A 2D detector is located downstream to collect the diffraction patterns. During the experiment, the sample is scanned in the (x, y) plane for a series of projection angles Ω . Either the sample, or the illumination and detector, are rotated around the y -axis.

The experiment proceeds by acquiring a set of ptychographic projections for an angular range of at least 180° . A schematic representation of an experimental setup

is shown in figure 2.12. For each projection angle Ω , the sample is scanned in the (x, y) plane with a coherent and spatially confined illumination. A 2D detector is located downstream to collect the diffraction patterns. The resulting dataset is 5D and has the shape $(n_\Omega, n_y, n_x, n_v, n_u)$. The number of projection angles is denoted by n_Ω . The number of scanning steps in the vertical and horizontal direction is denoted by n_y and n_x , respectively. The number of detector pixels along the vertical and horizontal dimension is denoted by n_v and n_u , respectively.

2.4.2 Ptychographic X-ray Computed Tomography

Ptychographic X-ray Computed Tomography (PXCT) is the utilization of ptychographic projections for a subsequent tomographic reconstruction. The approach exists almost as long as ptychography and is well established in literature [1], [3], [24], [40], [87]. Ptychographic projections are perfectly suited for the tomographic model. In equation 2.37, the tomographic model requires that the modality of interest is linearly integrable over the object space. In most ptychographic algorithms, it is the projected object-transmission function O_Ω that is calculated and O_Ω is not linearly integrable over the object space. However, from O_Ω , the projected complex refractive index decrement ν_Ω can be calculated by reformulating equation 2.15 to

$$\nu_\Omega(r) = -\frac{i}{k} \log(O_\Omega(r)), \quad (2.58)$$

and ν_Ω is linearly integrable.

In practice, one would first reconstruct all projections with a ptychographic algorithm of choice, e.g. one of the presented algorithms in section 2.2.2 to 2.2.5. All projections must represent the projected complex refractive index decrement ν_Ω .

The projections ν_Ω are then the input for any of the tomographic algorithms presented in section 2.3.4 to 2.3.6. The only noticeable difference to the description of tomography in section 2.3 is that the contrast is now a complex number. The projections ν_Ω are analytically just

$$\nu_\Omega(t, y) = \int_{(\Omega, t)} \nu(x, y, z) ds \quad (2.59)$$

$$\nu_\Omega(t, y) = \int_{(\Omega, t)} -\delta(x, y, z) + i\beta(x, y, z) ds \quad (2.60)$$

Since the phase shift δ and the absorption β of ν are additive, the integration can be done separately.

$$\nu_{\Omega}(t, y) = - \int_{(\Omega, t)} \delta(x, y, z) \, ds + i \int_{(\Omega, t)} \beta(x, y, z) \, ds \quad (2.61)$$

$$-\delta_{\Omega}(t, y) + i\beta_{\Omega}(t, y) = \int_{(\Omega, t)} -\delta(x, y, z) \, ds + i \int_{(\Omega, t)} \beta(x, y, z) \, ds \quad (2.62)$$

The projected complex refractive index ν_{Ω} has been split up into scattering $-\delta_{\Omega}$ and absorption β_{Ω} . A tomographic algorithm can be applied separately to the set of $-\delta_{\Omega}$ and the set of β_{Ω} .

2.4.3 Coupled Ptychographic Tomography

Coupled Ptychographic Tomography (CPT) performs the ptychographic and tomographic reconstruction simultaneously. This is in contrast to PXCT, which does a subsequent tomographic reconstruction of the converged ptychographic projections. The CPT procedure presented here has been first introduced and tested on simulated data by Gursöy in 2017 [88]. Kahnt, et al., have successfully applied it on experimental data in 2019 [29].

The CPT reconstruction starts by first defining a volume that holds the 3D complex refractive index decrement $\nu(x, y, z)$

$$\nu(x, y, z) = -\delta(x, y, z) + i\beta(x, y, z). \quad (2.63)$$

In case of no prior knowledge about the sample, the volume ν can be initialized as zero. Then, the existing volume is projected into 2D with the Radon transformation defined in equation 2.38.

$$\nu_{\Omega}(t, y) = \int_{(\Omega, t)} \nu(x, y, z) \, ds. \quad (2.64)$$

This yields the forward projection ν_{Ω} , with which the projected object-transmission function O_{Ω} can be calculated

$$O_{\Omega}(t, y) = e^{-ik\delta_{\Omega}(t, y)} e^{-k\beta_{\Omega}(t, y)}. \quad (2.65)$$

Furthermore, each ptychographic projection refines an individual illumination P_{Ω} . The forward projected object-transmission function O_{Ω} and the illumination P_{Ω} are

updated by one iteration of a ptychographic reconstruction algorithm \mathcal{P}

$$O'_\Omega(t, y) = \mathcal{P}_O[P_\Omega(t, y), O_\Omega(t, y)], \quad (2.66)$$

$$P'_\Omega(t, y) = \mathcal{P}_P[P_\Omega(t, y), O_\Omega(t, y)] \quad (2.67)$$

in which O'_Ω denotes the updated projected object-transmission function and P'_Ω denotes the updated illumination. In principle, the ptychographic update can be performed utilizing an arbitrary algorithm, e.g. one of the algorithms introduced in 2.2.2 to 2.2.5.⁶ The updated projected complex refractive index decrement ν'_Ω is calculated

$$\nu'_\Omega(t, y) = -\frac{i}{k} \log(O'_\Omega(t, y)). \quad (2.68)$$

Lastly, the 3D complex refractive index decrement is updated by ν'_Ω using a tomographic reconstruction algorithm \mathcal{T}_Ω

$$\nu'(x, y, z) = \mathcal{T}_\Omega(\nu'_\Omega(t, y)). \quad (2.69)$$

The updated volume of the complex refractive index decrement is denoted by ν' . Candidates for the tomographic update \mathcal{T}_Ω are especially the iterative approaches presented in sections 2.3.5 and 2.3.6.

One iteration of the CPT procedure consists of processing each projection once. The projections are processed sequentially. The reconstruction is iterated until the contrast of the reconstruction converges.

In principle, the FBP can be utilized for the tomographic update, too, but it comes with some extra work. The tomographic update of ν' by an FBP is a result of an inverse Fourier transform. Within CPT, it is essential that the existing volume ν is considered during the tomographic update. To achieve this consideration, one would need to do a forward projection of all other projection angles Ω and perform the FBP of all projections. For this situation, it may be favorable to perform the ptychographic update of all projections simultaneously, to not incorporate a performance overhead.

⁶When using `refPIE` as the ptychographic reconstruction algorithm, equation 2.65 and 2.68 do not need to be applied, since `refPIE` directly operates on the complex refractive index decrement ν_Ω .

3 Ensemble Refinement

This chapter introduces the Ensemble Refinement (ER), which is an approach for ptychography to algorithmically correct for vibrations that occur during the data acquisition.

The ptychographic data acquisition consists of scanning the sample transversally to the direction of the illumination, as shown in figure 2.2. The step sizes used for such a scan at PtyNAMi are typically between 50 nm and 500 nm and the typical exposure time at PtyNAMi is between 50 ms and 1000 ms [22]. The ideal ptychographic model assumes that there is no relative movement between the illumination and the sample during the exposure of a scan position \vec{r}_n .

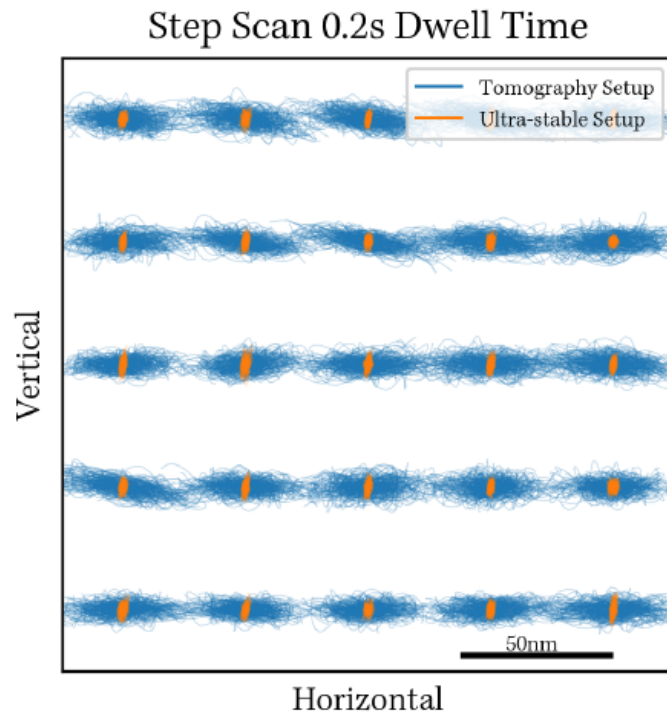


Figure 3.1: The result of the vibration characterization at PtyNAMi conducted by Martin Seyrich. The movement of the object is shown for each scan position \vec{r}_n for a step scan with 0.2s exposure time. The blue curves refer to the setup used for the acquisition of the datasets evaluated in this work. The orange curves refer to a setup that is not used in this work. [89]

In figure 3.1, Martin Seyrich has characterized the vibrations that occur at PtyNAMi utilizing a set of optical interferometers [89]. The blue curves show the relative move-

ment between object and illumination for the mechanical setup utilized to collect the datasets evaluated in this work. The orange curves refer to a setup that is not utilized throughout this work. The vibrations at PtyNAMi during a 0.2 s exposure may be roughly up to 50 nm horizontally and 20 nm vertically. The typical real space pixel size of ptychographic datasets collected at PtyNAMi is between 10 nm and 20 nm.

The vibrations can cause a blurring of the reconstructed object. Assuming that a dataset has a real space pixel size of 10 nm, then a diffraction pattern I_n corresponds up to 5 px horizontally and up to 2 px vertically. The approach in this chapter follows the idea, that the vibrations per scan position can be modeled as a incoherent superposition of a slightly shifted object in the measured diffraction pattern I_n .

In section 3.1 the extension to the ptychographic model with ePIE as reconstruction algorithm is introduced that can account and correct for the before mentioned vibrations. This novel model is referred to as the Ensemble Refinement (ER). Section 3.2 performs preliminary tests on a simulated dataset to verify the general working principle of the ER. Then, the ER is applied to two experimental datasets in sections 3.3 and 3.4. The approach presented here yields a significantly reduced performance, which is elaborated in section 3.5. A conclusion is given in section 3.6.

3.1 Adaption of the Ptychographic Model

The approach described in this section originates from Christian G. Schroer.

First, an additional vector $\vec{r}_{n,\nu} = (x_{n,\nu}, y_{n,\nu})$ is introduced, which describes the relative movement between object and illumination during exposure. The index ν denotes the index of the vibration position. The exit wavefield $\psi_{n,\nu}$ for a specific scan position \vec{r}_n and a specific vibration position $\vec{r}_{n,\nu}$ is

$$\psi_{n,\nu}(\vec{r}) = O(\vec{r} - \vec{r}_n - \vec{r}_{n,\nu})P(\vec{r}), \quad (3.1)$$

in which O is the object and P is the illumination. It is emphasized that the result is not altered whether the additional shift is included in O or P . Furthermore, the model assumes that the illumination is the same for every scan position \vec{r}_n and every vibration position $\vec{r}_{n,\nu}$.

The propagation of $\psi_{n,\nu}$ to the detector plane is the same as for the standard ptychographic model. This work evaluates only datasets with far-field geometry,

such that the propagation is modeled by a Fourier transform \mathcal{F}

$$\Psi_{n,\nu}(\vec{q}) = \mathcal{F}[\psi_{n,\nu}(\vec{r})]. \quad (3.2)$$

The propagated exit wavefield is denoted by $\Psi_{n,\nu}$ and the vector pointing in the reciprocal space is denoted by \vec{q} . During exposure, there may be several vibration positions $\vec{r}_{n,\nu}$, which gives several exit wavefields $\psi_{n,\nu}$ and each wavefield is propagated individually to the detector plane. The detected intensity I_n is modeled as the incoherent sum of the intensity of each propagated wavefield $\Psi_{n,\nu}$

$$I_n(\vec{q}) = \sum_{\nu} \rho_{n,\nu} |\Psi_{n,\nu}(\vec{q})|^2. \quad (3.3)$$

The weighting factor $\rho_{n,\nu}$ can be understood as the fractional exposure time of the relative movement $\vec{r}_{n,\nu}$ between the object O and illumination P . Therefore, $\rho_{n,\nu}$ can only be positive, since there is no physical interpretation for a negative exposure time. The $\rho_{n,\nu}$ must be determined. Equation 3.3 is reformulated to

$$\arg \min_{\rho} \left| I_n(\vec{q}) - \sum_{\nu} \rho_{n,\nu} |\Psi_{n,\nu}(\vec{q})|^2 \right|^2, \quad (3.4)$$

which is a least squares problem of the form $\mathbf{A}\vec{x} = \vec{b}$. The shifts $\vec{r}_{n,\nu}$ can be guessed, for instance as a regular grid. Then, $\rho_{n,\nu}$ is the only unknown in equation 3.4 and can be determined with a non-negativity constrain. From here on, the optimization of equation 3.4 is referred to as the Non-Negative Least Squares (NNLS) fit. The mathematical algorithm that is used for all NNLS fits in this work originates from Lawson and Hanson [90].

The modulus of each propagated wavefield $|\Psi_{n,\nu}|$ is updated by the intensities I_n of the measured diffraction pattern

$$|\Psi'_{n,\nu}(\vec{q})| = \sqrt{|\Psi_{n,\nu}(\vec{q})|^2 \sum_{\mu} \rho_{n,\mu} + I_n(\vec{q}) - \sum_{\mu} \rho_{n,\mu} |\Psi_{n,\mu}(\vec{q})|^2}, \quad (3.5)$$

in which $\Psi'_{n,\nu}$ denotes the updated propagated wavefield. The squared modulus $|\Psi_{n,\nu}(\vec{q})|^2$ of each wavefield is scaled by the sum of the weighting factors $\sum_{\mu} \rho_{n,\mu}$. This is necessary since the sum of $\rho_{n,\nu}$ does not necessarily equal 1. Then, the residual $I_n(\vec{q}) - \sum_{\mu} \rho_{n,\mu} |\Psi_{n,\mu}(\vec{q})|^2$ is added to the rescaled squared modulus $|\Psi_{n,\nu}(\vec{q})|^2 \sum_{\mu} \rho_{n,\mu}$.

The updated wavefields $\Psi'_{n,\nu}$ are propagated back into the object plane utilizing

the inverse Fourier transform \mathcal{F}^{-1}

$$\psi'_{n,\nu}(\vec{r}) = \mathcal{F}^{-1}[\Psi'_{n,\nu}(\vec{q})]. \quad (3.6)$$

The backpropagated updated wavefield is denoted by $\psi'_{n,\nu}$.

Then, the object O and illumination P are updated by

$$O'(\vec{r} - \vec{r}_n) = O(\vec{r} - \vec{r}_n) + \alpha \sum_{\nu} \frac{\rho_{n,\nu}}{\sum_{\mu} \rho_{n,\mu}} \frac{P^*(\vec{r} + \vec{r}_{n,\nu})}{\|P(\vec{r} + \vec{r}_{n,\nu})\|_{\max}^2} (\psi'_{n,\nu}(\vec{r}) - \psi_{n,\nu}(\vec{r})), \quad (3.7)$$

$$P'(\vec{r}) = P(\vec{r}) + \beta \sum_{\nu} \frac{\rho_{n,\nu}}{\sum_{\mu} \rho_{n,\mu}} \frac{O^*(\vec{r} - \vec{r}_n - \vec{r}_{n,\nu})}{\|O(\vec{r} - \vec{r}_n - \vec{r}_{n,\nu})\|_{\max}^2} (\psi'_{n,\nu}(\vec{r}) - \psi_{n,\nu}(\vec{r})), \quad (3.8)$$

in which O' and P' are the updated object and illumination, respectively, and O^* and P^* denote the complex conjugates of O and P , respectively. The weighting factors $\rho_{n,\nu}$ are normalized so that their sum equals unity. One iteration consists of processing each diffraction pattern I_n . The diffraction patterns I_n are processed in a random order. The procedure is iterated until the reconstruction converges.

During the next sections, different combinations for $\vec{r}_{n,\nu}$ will be tested. In this work, the set of $\vec{r}_{n,\nu}$ will always span a square shaped grid defined by the spread r_e . The $x_{n,\nu}$ and $y_{n,\nu}$ components of a set with $r_e = 1$ are $x_{n,\nu} = y_{n,\nu} = \{-1, 0, 1\}$, yielding 9 different $\vec{r}_{n,\nu}$ in total. A set with $r_e = 2$ has 25 different $\vec{r}_{n,\nu}$, and so forth. From here on, a set of $\vec{r}_{n,\nu}$ with its corresponding weights $\rho_{n,\nu}$ is described as an ensemble.

3.2 Simulation Study

To begin, some preliminary tests in regard to the basic functionality of the ER are done.

A test dataset is simulated using the Baboon test image as the object. The amplitude and phase of the exact object-transmission function is shown in figure 3.2 a) and b), respectively. The dimensions of the object are 806 px vertically and horizontally. The dimensions include already the obligatory padding by the size of the illumination. Furthermore, 20 pixels have been added to the top, bottom, left and right to incorporate the ensemble shifts $r_{n,\nu}$ of the scan positions r_n closest to the object edges.

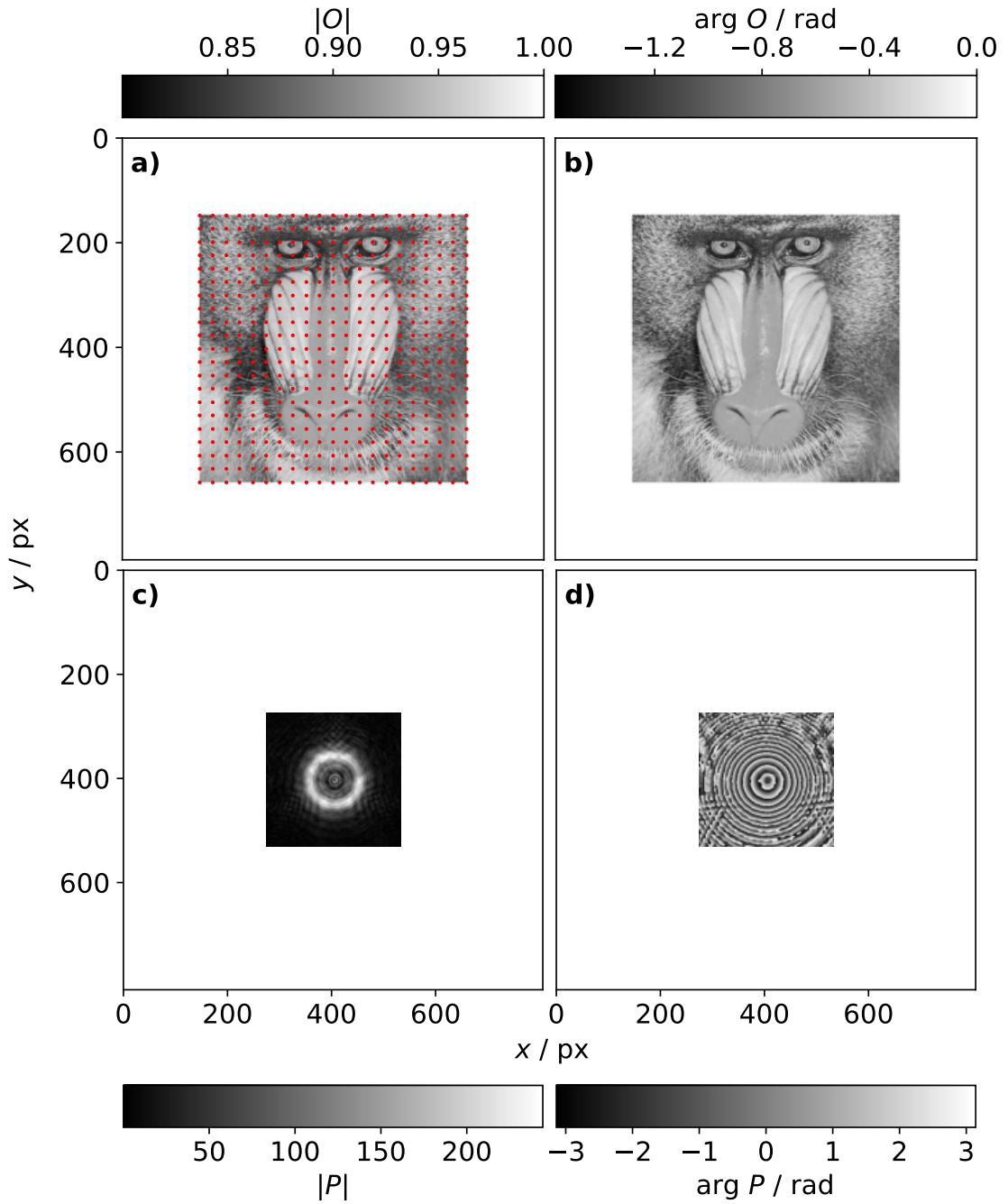


Figure 3.2: An illustration of the dataset used for the simulation study of the ER. a) The amplitude of the object-transmission function. The red dots mark the scan positions \vec{r}_n . b) The phase of the object-transmission function. c) The amplitude of the illumination. d) The phase of the illumination.

The amplitude and phase of the illumination is shown in figure 3.2 c) and d), respectively. The illumination originates from the experimental data presented in sections 3.4 and 5.2. This illumination was created by a Fresnel Zone Plate (FZP)

with a focus size of 70 nm. The illumination used here is located 1.0 mm behind the focal plane of the FZP, yielding an illumination size of 1.8 μm . The energy of the illumination is 9.0 keV. The geometry is simulated such that the detector is located 2.13 m behind the sample and the detector has a pixel size of 75 $\mu\text{m} \times 75 \mu\text{m}$. However, the discussion in this section will be done with pixel coordinates. The reason to choose an experimental illumination for the simulations is that the illumination has significant influence on the behavior of the ER. Using an experimental illumination may best represent a practical scenario.

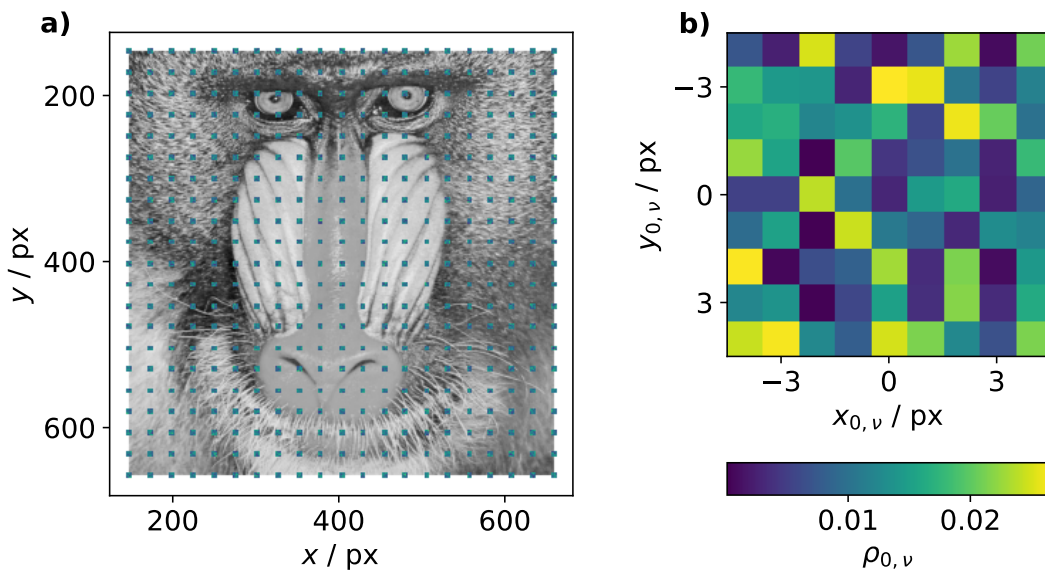


Figure 3.3: a) The ensembles of the Baboon test drawn in the object space. Each ensemble has a spread of $r_e = 4$. b) The ensemble of the upper left scan position \vec{r}_0 in a magnified view.

Using the test object and illumination, a dataset is simulated with 21 scan positions along the horizontal and vertical direction, such that the dataset has 441 diffraction patterns in total. For each scan position \vec{r}_n , the vibrations are simulated by an ensemble with a spread $r_e = 4$. The detector values are calculated using equation 3.3 and Poisson noise is added. A summary image of the ensembles is shown in the magnified view of the object phase in figure 3.3 a). The ensemble for $n = 0$, which is the most upper left scan position, is shown in figure 3.3 b). The weights $\rho_{n,\nu}$ are chosen randomly with the constraint that the sum of the weights of each ensemble equals unity, i.e. $\sum_{\nu} \rho_{n,\nu} = 1$. The retrieved phase contrast of the object of an ePIE reconstruction is shown in figure 3.4 b) and f). The ePIE reconstruction is significantly blurred compared to the exact object in figure 3.4 a) and e).

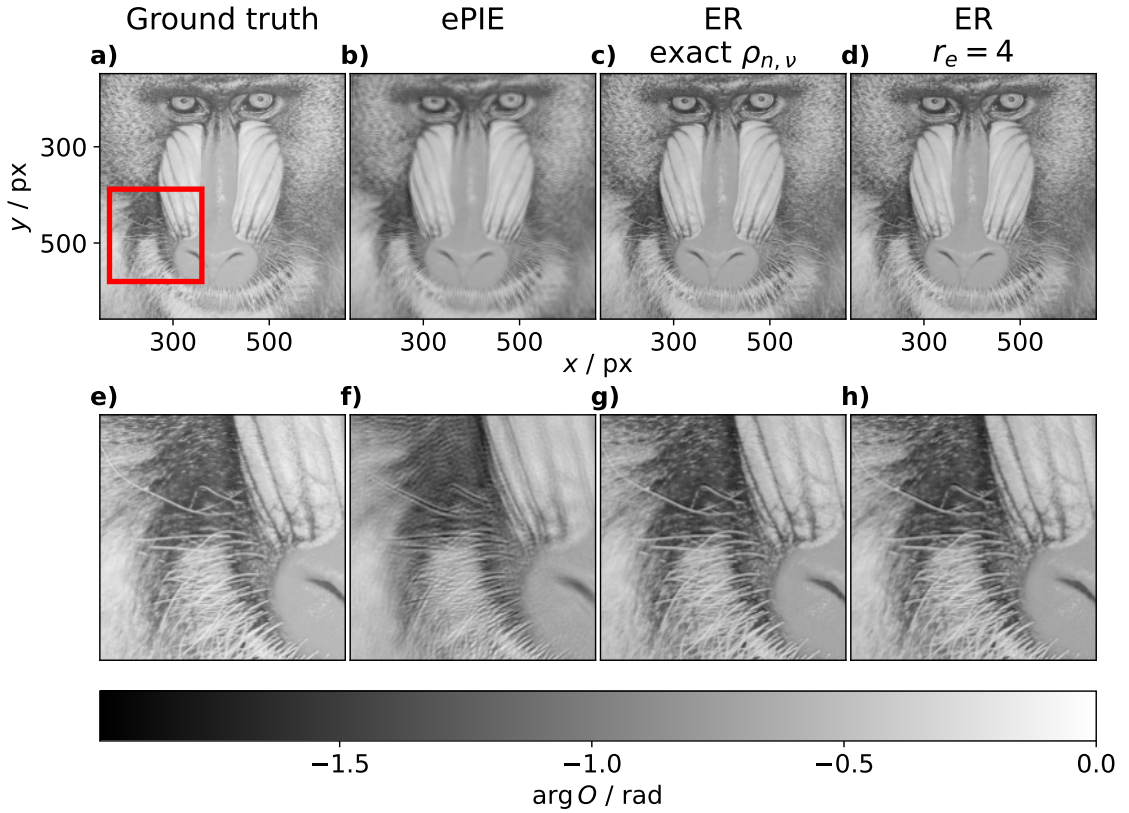


Figure 3.4: An illustration of the effect of a vibration disturbed dataset on the corresponding ptychographic reconstruction. a) The exact phase shift of the Baboon test image. b) An ePIE reconstruction of the 4 px vibrating Baboon test dataset. The reconstructed object is significantly blurred. c) The ER has been applied utilizing the exact ensembles and circumventing the NNLS fit. The object is reconstructed with higher quality. d) The ER with $r_e =$ has been applied, the weights $\rho_{n,\nu}$ have been determined during the reconstruction by using the NNLS fit in equation 3.4. e) to g) A magnified view of the corresponding upper image. The magnified region is marked by the red square in a).

3.2.1 Verification of the Model and the Implementation

First, it is verified if the model can correct for vibrations that occur during the experiment. For this, an ER reconstruction of the test dataset is done, but the exact weights $\rho_{n,\nu}$ shown in figure 3.3 a) are utilized and no NNLS fit is applied during the reconstruction. A converged ePIE reconstruction is used as an initial guess for the object. Furthermore, the exact illumination is utilized during the reconstruction and the illumination is not updated, such that $\beta = 0$ in equation 3.8. The reconstruction ran for 400 iterations, after which no further change in the reconstructed object could be observed with more iterations. The phase of the reconstructed object is shown in

figure 3.4 c). For reference, the ePIE reconstruction is shown in b). Clearly, the ER corrects the vibrations when the shifts $r_{n,\nu}$ and weights $\rho_{n,\nu}$ are known. Furthermore, this test verifies that the ER is implemented properly.

3.2.2 Uncertainties of the Non-Negative Least Squares Fit

In a practical scenario, the weights $\rho_{n,\nu}$ are not known and must be determined by the NNLS fit. However, the exact object O and illumination P are not known either, making it more difficult for the NNLS fit. The diffraction pattern may not only contain the coherent scattering signal, but also scattering from other components along the optical path. Furthermore, every measurement at the detector is disturbed by Poisson noise. The diffraction pattern may also deviate due to partial coherence.

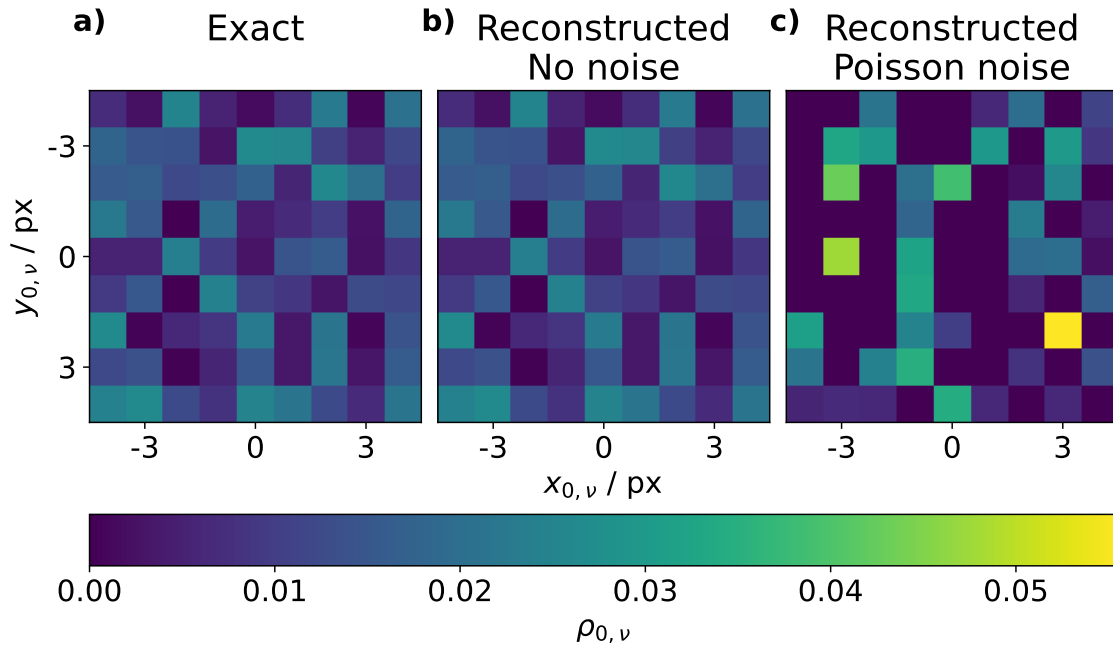


Figure 3.5: An illustration of the influence of Poisson noise on the NNLS fit. a) The exact ensemble of the upper left scan position in figure 3.3. b) The NNLS fit has been applied for a simulated diffraction pattern without noise. The fitted ensemble equals the exact ensemble. c) The NNLS fit has been applied for a simulated diffraction pattern with Poisson noise. The fitted ensemble deviates significantly from the exact ensemble.

For the following, it is assumed that the exact object O and illumination P are given and the simulated diffraction pattern is the exact result of this, such that no Poisson noise has been added. It is attempted to determine the weights with the NNLS fit. The resulting ensemble of the NNLS fit is shown in figure 3.5 b) and it

does equal the exact ensemble. The exact ensemble is shown for reference in figure 3.5 a).

While this example appears trivial, it is actually not, considering how similar the forward modeled diffraction patterns are. Remember that the forward modeled diffraction patterns differ only by up to ± 4 px of the object. The forward modeled diffraction patterns are not shown here, as it would look like a set of equal diffraction patterns.

Now, Poisson noise is added to the simulated diffraction pattern and the NNLS fit is again done utilizing the exact object O and illumination P . The result is shown in figure 3.5 c) and it deviates significantly from the exact ensemble in figure 3.5 a).

3.2.3 A First Reconstruction

A first reconstruction is attempted for the Poisson noise disturbed vibrating Baboon dataset shown in figure 3.3. To simplify the setting, the reconstruction is started with the exact illumination shown in figure 3.2 c) and d). Furthermore, the illumination is not updated during the reconstruction, i.e. $\beta = 0$ in equation 3.8. A converged ePIE reconstruction is used as an initial guess for the object. The ER reconstruction ran for 400 iterations, after which no further change in the reconstructed object could be observed. The phase of the reconstructed object is shown in figure 3.4 d) and h). The blurring is corrected and even the sharp features in the lower left and lower right region can be recognized.

The example still does not represent a practical scenario. Typically, the ensemble shifts $r_{n,\nu}$ are not known. If the ptychographic microscope is characterized well, a good guess can be made for the shifts. However, stability cannot be guaranteed in the long term.

In the following, it is investigated how the ER performs when the ensemble shifts $r_{n,\nu}$ are guessed. Figure 3.6 c) to h) show ER reconstructions for $1 \leq r_e \leq 6$. Each reconstruction ran for 400 iterations, after which no further change in the reconstructed object could be observed. For reference, the exact object and the ePIE reconstruction are shown in figure 3.6 a) and b), respectively.

It appears that the vibrations are reliably corrected for every value of $r_e > 3$. Interestingly, even for $r_e = 3$ the vibrations seem to be corrected and the reconstruction looks fine. This is a great result, as it indicates that the ensemble shifts $r_{n,\nu}$ can be guessed generously and the result is not affected by it.

To summarize, the preliminary tests indicate a reliable working principle of the ER. In the next sections, the ER is applied to two experimental datasets.

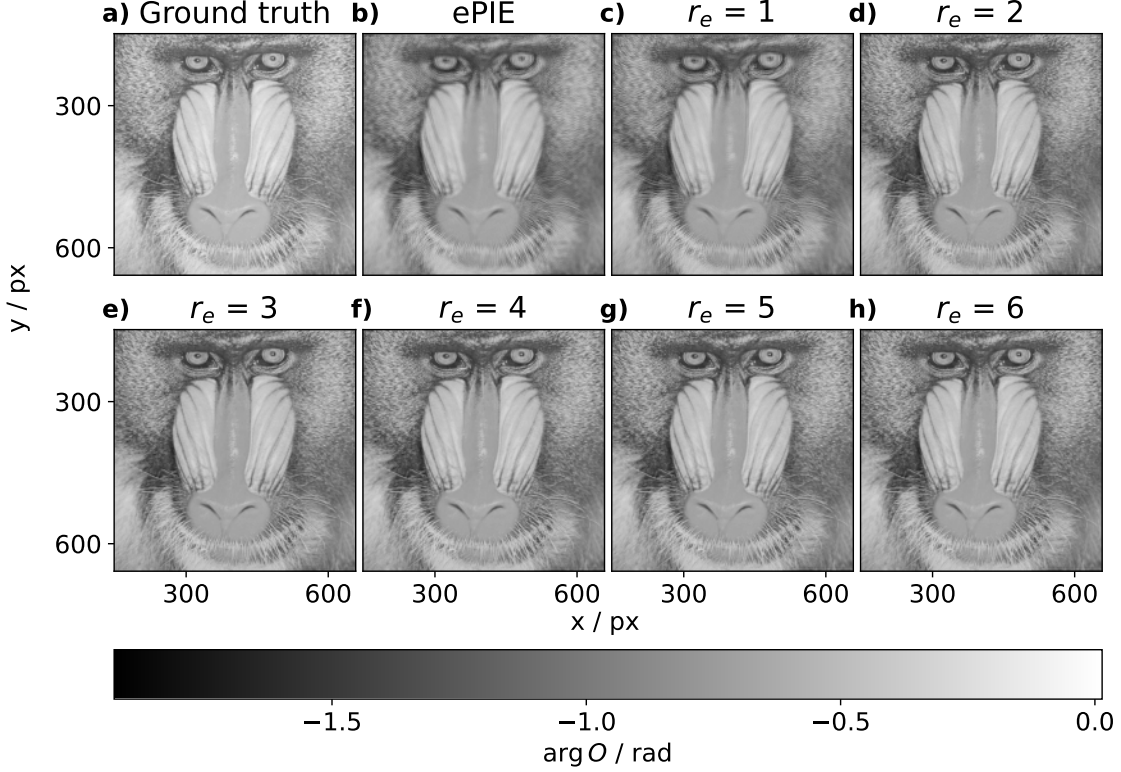


Figure 3.6: ER reconstructions for the Poisson noise disturbed vibrating Baboon test dataset with ensemble spread $r_e = 4$. a) The phase of the exact object. b) The phase of the reconstructed object by 1000 ePIE iterations. These serve as a reference to assess the ER reconstructions. From c) to h), the ER is applied with an ensemble size of $r_e = 1$ to $r_e = 6$. Each reconstruction ran for 400 iterations. The object is properly reconstructed when $r_e \geq 4$.

3.3 Siemens star

3.3.1 Dataset

A ptychographic dataset of a Siemens star test object has been acquired at the microprobe endstation of beamline P06 at PETRA III in 2023. The incoming synchrotron beam had an energy of 25 keV and was focused with a stack of Compound Refractive Lenses (CRLs) to a circular shape with 200 nm diameter. The Siemens star was positioned 2 mm behind the focal plane of the CRLs, giving an illumination size in the object plane of roughly 1 μm . The distance between the sample and the detector was 8.185 m. The detector is an Eiger X1M CdTe with a pixel size of 75 $\mu\text{m} \times 75 \mu\text{m}$. Most of the propagation path between sample and detector is evacuated by a vacuum tube. The diffraction patterns are cropped to a square shape with

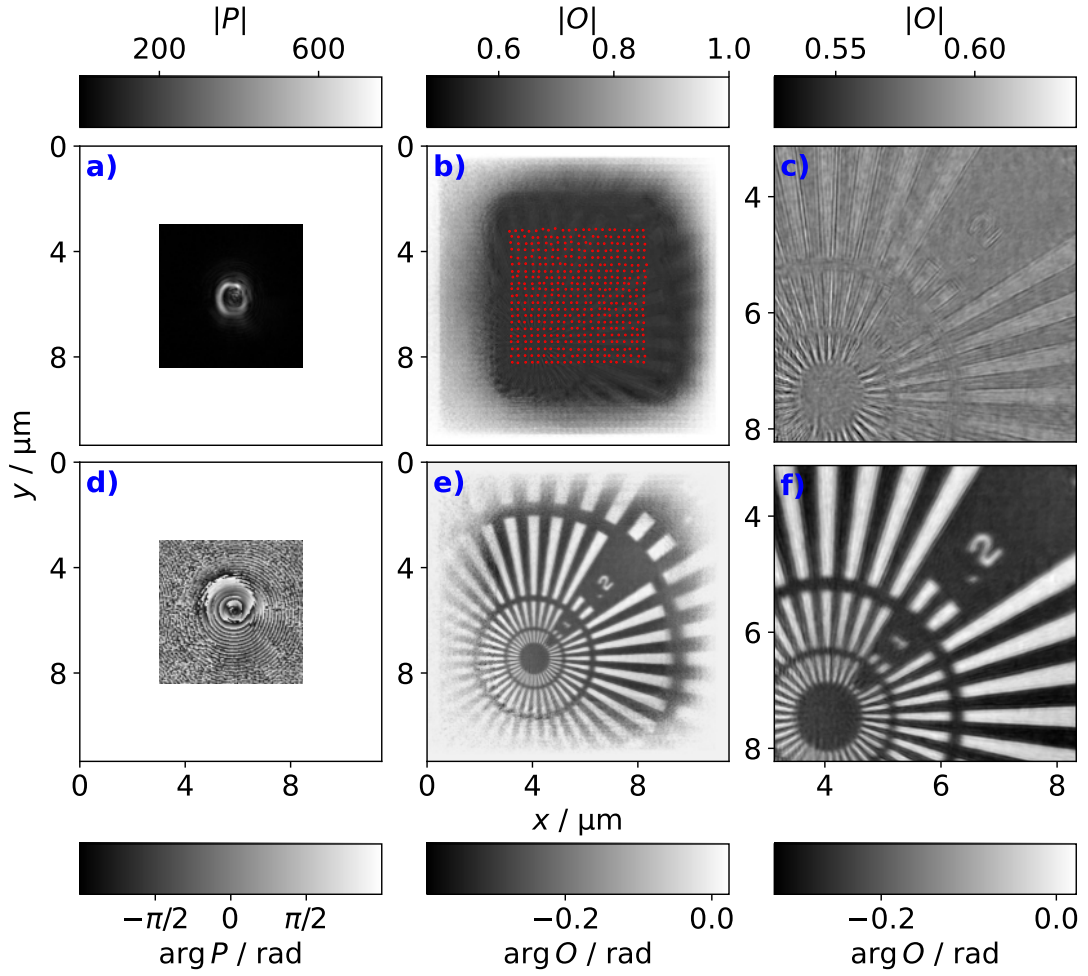


Figure 3.7: An ePIE reconstruction of the Siemens star dataset to illustrate the object and the illumination. a) The amplitude of the illumination. b), the amplitude of the object. The red dots mark the scan positions \vec{r}_n . c) The amplitude of the object cropped by the object enlargement and half the illumination size. d) The phase of the illumination. e) the phase of the object. f) The phase of the object cropped by the object enlargement and half the illumination size.

256 px edge length to reduce the amount of data and have a better performance during the reconstruction. The experimental geometry yields a real space pixel size of 21.14 nm. The sample was translated on a square grid with 21 steps along both the horizontal and vertical dimension. The step size was 250 nm horizontally and vertically, yielding a nominal scan window of $5 \mu\text{m} \times 5 \mu\text{m}$.

To further illustrate the dataset of the Siemens star, a regular ePIE reconstruction is done and shown in figure 3.7. The illumination amplitude has been initialized as a circular profile with a diameter of $1 \mu\text{m}$. The phase of the illumination has been

initialized by propagating a planar phase profile for 2 mm. The amplitude of the object has been constrained to have values between 0 and 1. The phase of the object has been constrained to have values between $-\pi$ and 0. The amplitude and phase of the reconstructed illumination are shown in figure 3.7 a) and d), respectively. The amplitude and phase of the reconstruct object are shown in figure 3.7 b) and e), respectively. The object has been enlarged by 20 px to have a common object shape with the later ER reconstructions. The scan positions \vec{r}_n are marked by the red dots in 3.7 b). The illumination and object reconstruction in 3.7 a), b), d), and e), are drawn with equal pixel sizes to illustrate the high amount of overlap that this dataset has.

The cropped amplitude and phase of the object are shown in 3.7 c) and f), respectively. Half the illumination size and the 20 px object enlargement are cropped from the left, right, top, and bottom of the object to only show the scan window. The contrast is much better for the phase, which is typical for hard X-rays, so that the following analysis and discussion will be carried out for the recovered phase. In 3.7 f), it can be seen that the features of the object are blurred, caused by the vibrations during the experiment. Especially the small features in the lower left region are severely blurred.

Furthermore, for all reconstructions of the Siemens star dataset, a prior ePIE reconstruction has been performed with the position refinement described in section 2.2.6. Prior to the position refinement, 100 initial ePIE iterations were performed. The position refinement was then applied every 10 iterations. The reconstruction ran for 1000 iterations in total, such that every scan position was refined 90 times. During the reconstruction, the change of the positions was monitored by visual inspection, to ensure that that refined positions are converged. The refined positions are used for all reconstructions in this section, including already the reconstruction shown in figure 3.7.

3.3.2 Reconstruction

Now, ER reconstructions are done for the Siemens star dataset. The exact vibrational shifts $r_{n,\nu}$ are not known and just guessed. Reconstructions are done for $1 \leq r_e \leq 11$ and shown in figure 3.8 b) to l). Each reconstruction has been started with the object and illumination shown in figure 3.7 as initial guesses. The ER reconstructions ran for 200 iterations, after which no further correction of the blurring could be observed. The converged ePIE reconstruction is shown in figure 3.8 a) for reference.

Starting from $r_e = 1$, a modest improvement of the blurring can be observed. The

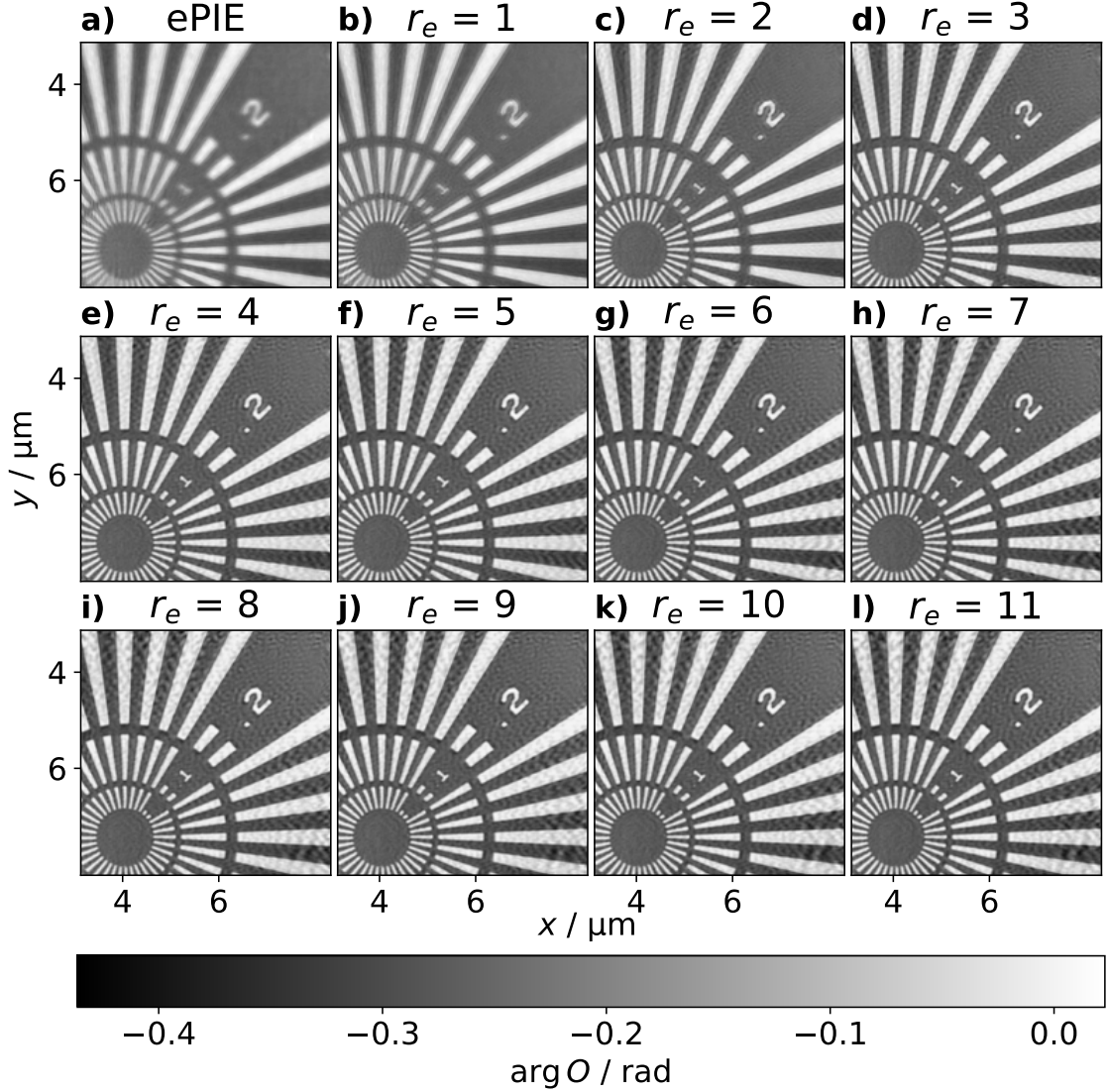


Figure 3.8: ER reconstructions for the Siemens star dataset. Each reconstruction has been cropped by the object enlargement and half the illumination size. a) A regular ePIE reconstruction of 1000 iterations. b) to l) ER reconstructions for $r_e = 1$ to $r_e = 11$. Each reconstruction ran for 200 iterations, after which no further change in the reconstructed object could be observed by visual inspection.

improvement increases with ensemble spread r_e and around $r_e = 4$, the blurring appears to be minimal. However, a background pattern is introduced in the upper and right region of the object for large r_e . In the following, the background pattern is explained by taking a closer look on the ensembles.

Figure 3.9 a) shows the ER reconstruction with $r_e = 11$ and the colored dots mark five different scan positions \vec{r}_n . The corresponding ensembles are shown in figure 3.9

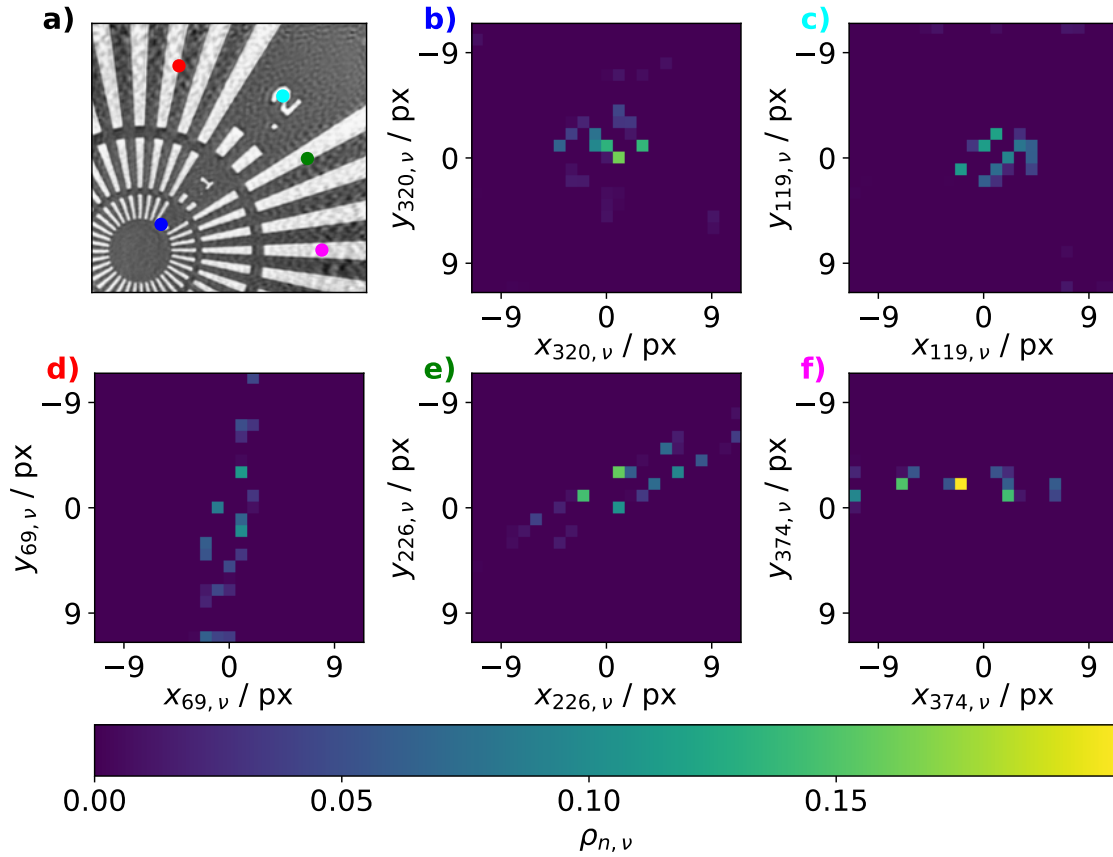


Figure 3.9: An illustration how the weights $\rho_{n,\nu}$ of different scan positions \vec{r}_n look like. a) The ER reconstruction of the Siemens star for $r_e = 11$ is shown. The five colored dots mark the scan positions to which the ensembles in b) to f) correspond. The colored title notation in b) to f) corresponds to the colored dots in a). For b) and c), the ensembles look reasonable and indicate a vibration that is stronger along the horizontal dimension than the vertical dimension. For d) to f), the ensembles have a preferred orientation that is similar to the orientation of the bright stripes of the Siemens star. This is an artifact that does not represent the actual sample vibrations during the experiment.

b) to f), which is indicated by the the coloring of the panel denotation. For figure 3.9 b) and c), the ensembles have a reasonable shape that indicate a stronger vibration along the horizontal dimension than the vertical dimension.

For figure 3.9 d) to f), the ensembles have a preferred orientation similar to the orientation of the bright stripes of the Siemens star. This is an artifact, and the reconstructed ensembles do not represent the actual vibrations of the sample. The ER is a mathematical determination to find the set of positions $\vec{r}_{n,\nu}$ and weights $\rho_{n,\nu}$ that matches best the measured diffraction pattern following equation 3.4. For the scan positions in figure 3.9 d) to f), the samples morphology is approximately

invariant against a translation in the direction of the stripe orientation. The NNLS determines a set of positions $\vec{r}_{n,\nu}$ and weights $\rho_{n,\nu}$ that yields the smallest local error, and these $\vec{r}_{n,\nu}$ and $\rho_{n,\nu}$ do not reflect the actual vibration of the sample during the experiment. This is an intrinsic uncertainty of the ER model and may always occur for object shapes with a translation invariancy.

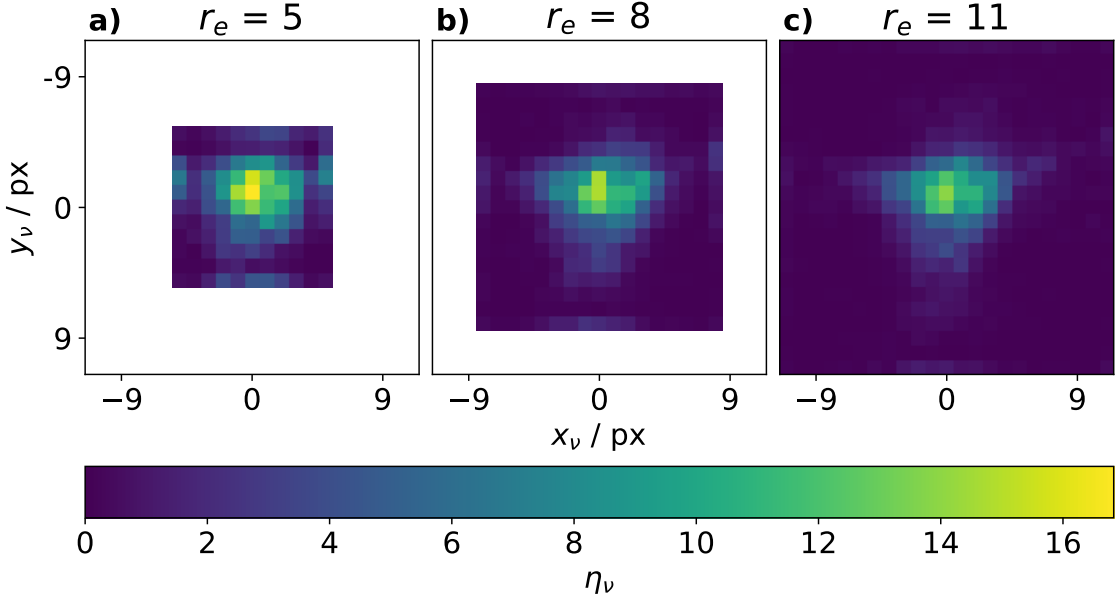


Figure 3.10: An illustration how the integrated ensembles η_ν are influenced by the size of the ensemble r_e . a) to c) The integrated ensembles η_ν are shown for r_e values of 5, 8, and 11.

To conclude, the ensembles of all scan positions r_n are summed up

$$\eta_\nu = \sum_n \rho_{n,\nu}, \quad (3.9)$$

in which η_ν is referred to as integrated weights. In figure 3.10, the integrated weights η_ν are shown for the ER reconstructions with $r_e = 5$, $r_e = 8$, and $r_e = 11$. It is visible that there is a continuous distribution of ensemble members in the central region. The distribution has a wider spread along the horizontal dimension than the vertical dimension. The integrated weights for $r_e = 5$ has a population of ensemble members at the ensemble edges. This is an artifact indicating the ensemble is chosen too small. For the larger ensembles in b) and c), the distribution at the edge is significantly reduced.

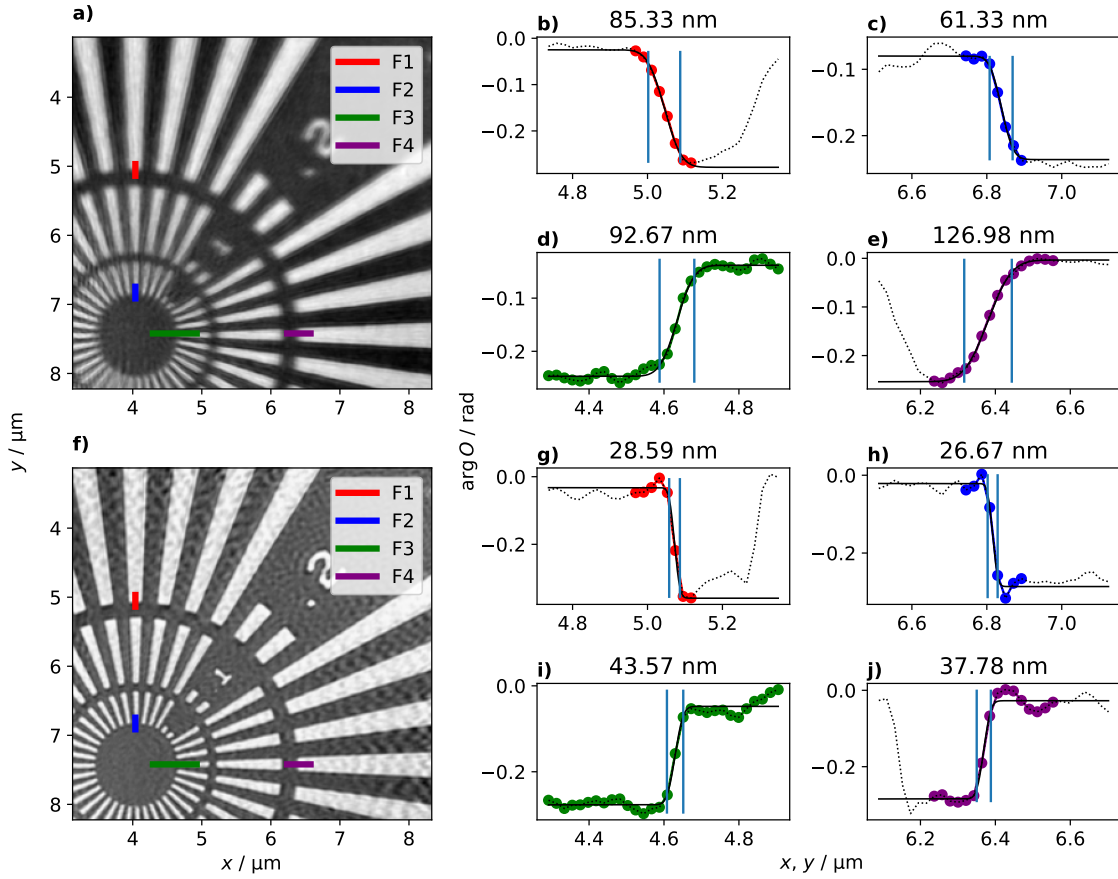


Figure 3.11: Line profiles for the Siemens star dataset to determine the improvement in the spatial resolution. a) The ePIE reconstruction with four features marked by the colored lines. b) to e) The line profiles of the features are shown. The color of the dots matches the color of the lines in a). The colored dots indicate the pixels that have been used to fit the error function. The dotted line in some of the plots shows further pixel values that have not been used to fit the error function. The blue vertical lines mark the positions of the 10 % and 90 % of the maximum value of the error function. The spatial resolution is defined as the distance between the two vertical lines and given in the title. f) The ER reconstruction for $r_e = 5$. The same features of a) are marked by the colored lines. g) to j) The respective error function fits of the line profiles. The resolution of all features is improved by the ER.

3.3.3 Spatial Resolution

The features of the Siemens star have sharp edges. This makes the object well suited for a characterization of the spatial resolution by line profiles. Figure 3.11 a) and f) show the ePIE and the ER $r_e = 5$ reconstruction. In both reconstructions, four different features are highlighted by colored lines. These features are used for the

line profiles, which are shown in b) to e) for the ePIE reconstruction and in g) to j) for the ER reconstruction.

The spatial resolution is defined as the distance between the 10% and 90% of the maximum value of the fitted error function. For the ePIE reconstruction, the resolutions vary between 61.33 nm and 126.98 nm, which is roughly the size of 3 to 6 object pixel. For the ER reconstruction, the resolutions vary between 27.55 nm and 38.41 nm, which is roughly the size of 1 to 2 object pixel. For all features, the ER reconstruction has a significantly improved spatial resolution of at least a factor 2.

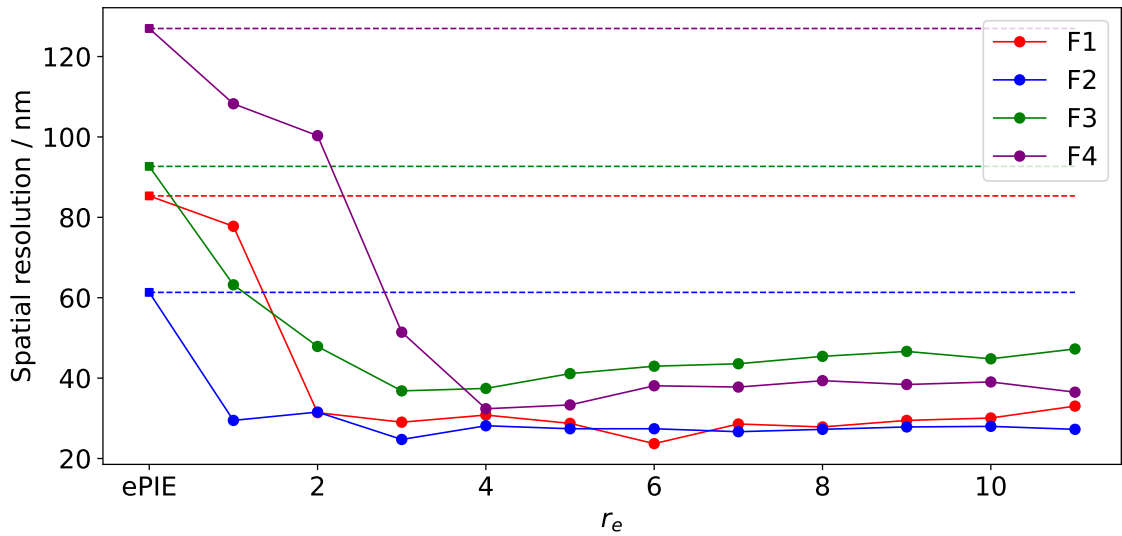


Figure 3.12: The spatial resolutions of the four features marked in figure 3.11 a) and f) vs. the ensemble size r_e of the reconstruction. The most left square points and the dashed lines mark the resolution of the ePIE reconstruction.

The features marked in figure 3.11 are used for an error function fit of the ER reconstructions with $1 \leq r_e \leq 11$. The spatial resolutions vs. the ensemble size r_e are shown in figure 3.12. The most left square points and the dashed lines mark the resolution determined for the ePIE reconstruction.

It can be seen that the best possible spatial resolution is only reached when the adjusted r_e reaches a certain value. For the blue feature, the best spatial resolution is reached at $r_e = 3$, while for the purple feature, the best possible resolution is achieved at $r_e = 4$. It is concluded that the best improvement of the blurring is reached at $r_e = 4$. Especially the curves of the green, purple and red feature indicate that the spatial resolution reaches a minimum around $r_e = 3$ and increases afterwards with increasing ensemble size r_e . However, the increase of the spatial resolution with higher r_e is comparatively small and well below the object pixel size of 21.14 nm. A

direct comparison of the ePIE and ER $r_e = 4$ reconstruction is shown in figure. In the next section, the ER is tested on a second experimental dataset.

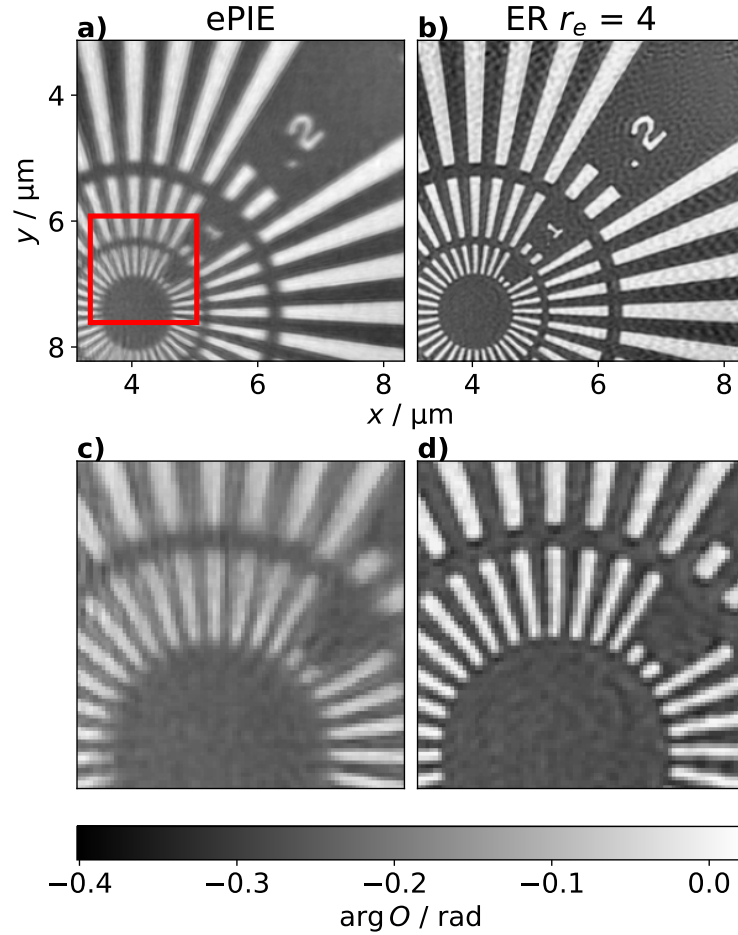


Figure 3.13: A comparison of the reconstructions obtained by ePIE and ER. a) The ePIE reconstruction. The red square marks the position of a subregion that is shown in c) and d). b) The ER $r_e = 4$ reconstruction. c) The subregion of the ePIE reconstruction. d) The subregion of the ER reconstruction.

3.4 Zeolite

3.4.1 Dataset

A dataset of a macroporous zeolite particle was acquired at PtyNAMi in 2018 [29], [91]. The particle is shown in the Scanning Electron Microscopy (SEM) image in figure 3.14 a). The sample was prepared by Focused Ion Beam (FIB). A platinum pedestal has been deposited on the aluminum sample holder. The zeolite particle is mounted onto the platinum pedestal. The illumination had an energy of 9 keV and was focused by a FZP to a circular spot size of 70 nm. The sample was positioned 1.0 mm behind the focal plane of the FZP, giving an illumination size of about $1.8\ \mu\text{m}$ in the object plane. The detector is an Eiger X4M that was positioned 2.13 m behind the sample. The detector pixels have a size of $75\ \mu\text{m} \times 75\ \mu\text{m}$. The diffraction patterns are cropped to a shape of $256\ \text{px} \times 256\ \text{px}$. This experimental geometry yields a reconstruction pixel size of 16.57 nm. The object was scanned on a grid with 11 steps horizontally and vertically. The step size was 400 nm horizontally and vertically, giving a nominal scan window of $4\ \mu\text{m} \times 4\ \mu\text{m}$.

To further illustrate the dataset, a converged ePIE reconstruction of 1000 iterations is shown in figure 3.14. The illumination amplitude has been initialized as a circular profile with $1.8\ \mu\text{m}$ diameter and the illumination phase by propagating a planar phase for 1.0 mm. The object has been enlarged by 20 px to the left, right, top, and bottom, to incorporate the ensemble shifts $r_{n,\nu}$ later in this section. The reconstructed amplitude and phase of the illumination are shown in figure 3.14 b) and e), respectively. The reconstructed amplitude and phase of the object are shown in figure 3.14 c) and f), respectively. The scan positions \vec{r}_n are marked by the red dots in figure 3.14 c). The evaluation in this chapter is carried out for the recovered phase, which has a better contrast than the amplitude. The illumination and object in figure 3.14 b), c), e) and f) are drawn with equal sizes to illustrate the high amount of overlap that the dataset has. The cropped amplitude and phase of the object is shown in figure 3.14 d) and g), respectively, to give a magnified view of the scan window.

The scan positions \vec{r}_n have been refined in a prior ePIE reconstruction using the position refinement presented in section 2.2.6. The refinement started after 10 iterations and ran for 990 iterations, after which no further change of the positions has been observed by visual inspection. The refined positions are used for all reconstructions in this chapter, including already the reconstruction shown in figure 3.14.

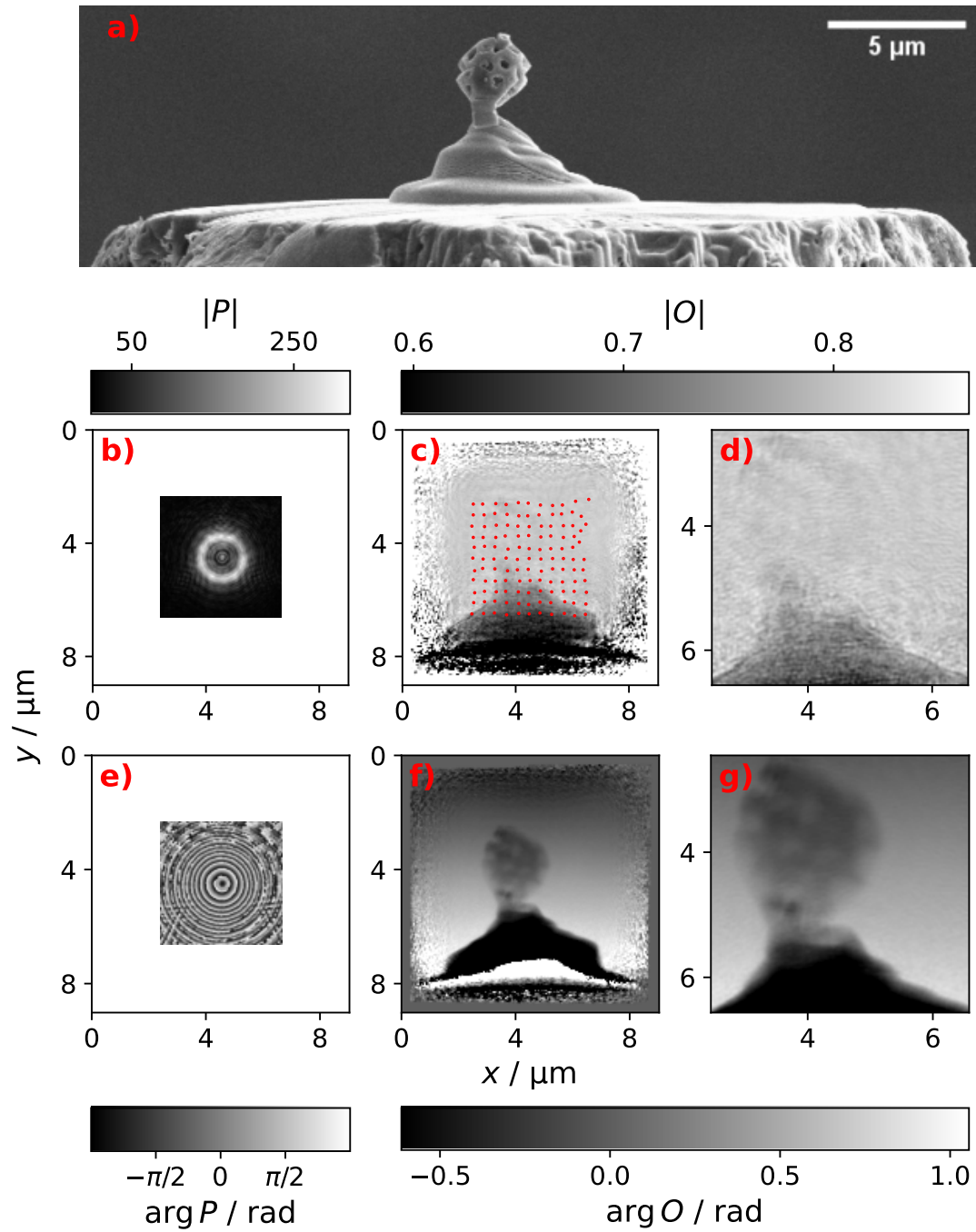


Figure 3.14: A summary of the zeolite dataset. a) A SEM image of the zeolite particle. b) The amplitude of the ePIE illumination reconstruction. c) The amplitude of the ePIE object reconstruction. d) The amplitude in c) cropped by half the illumination size and the object enlargement. e) phase of the ePIE illumination reconstruction. f) The phase of the ePIE object reconstruction. g) The cropped phase of the ePIE object reconstruction.

3.4.2 Reconstruction

ER reconstructions are done for ensemble spreads of $r_e = 1$ to $r_e = 11$. A converged ePIE reconstruction of 1000 iterations is used as the initial guess for the object and the illumination. Each ER reconstruction ran for 600 iterations, after which no further change in the reconstructed object could be observed with more iterations.

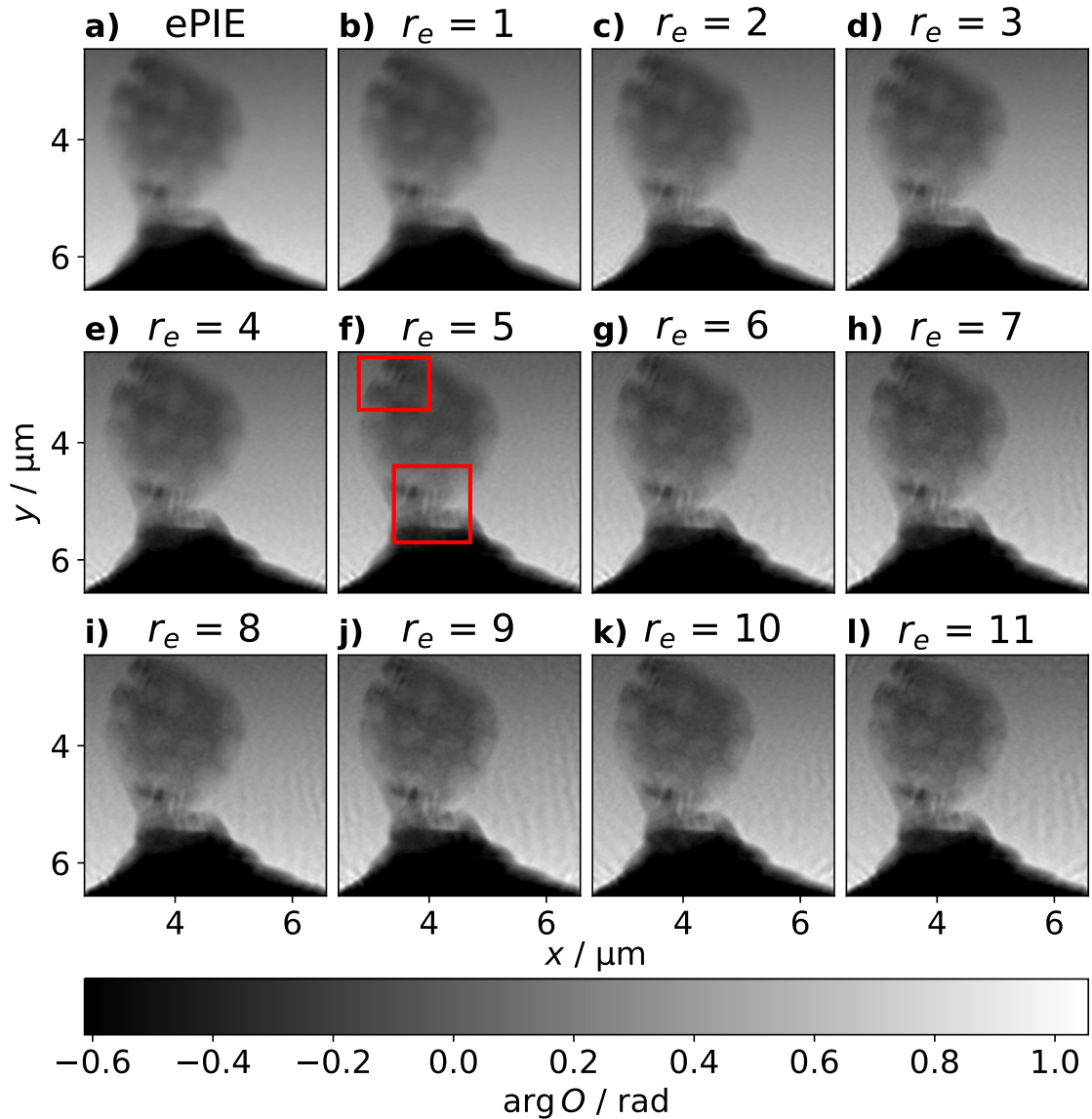


Figure 3.15: ER reconstructions for the zeolite dataset. a) The ePIE reconstruction used as the initial guess for the ER reconstructions. b) to h) The ER is applied for ensemble sizes from $r_e = 1$ to $r_e = 11$. Each ER reconstruction ran for 600 iterations. The red rectangles in f) mark two features that are significantly better resolved by the ER.

The reconstructed phase of the object for $r_e = 1$ to $r_e = 11$ is shown in figure 3.15

b) to l), the value of r_e is indicated in the title. For reference, the ePIE reconstruction is shown in figure 3.15 a). The reconstruction quality gradually improves with ensemble spread r_e . The red rectangles in figure 3.15 f) mark two features that become significantly better resolved by the ER. Roughly after $r_e = 5$, the quality of the reconstructed object is not further influenced by the ensemble size. This indicates that the ensembles are large enough to model the vibrations of the experiment.

Furthermore, the reconstruction quality does not obviously decrease for large ensembles spreads of $r_e > 7$. Since the ensemble size is a parameter that needs to be tuned by the user, it is an important result that the ensemble size can be guessed generously. However, for large ensemble sizes, such as $r_e = 11$, a pattern is introduced in the free space region at the right side of the reconstruction.

To investigate the cause of the pattern, five scan positions are marked by the colored dots in the reconstruction in figure 3.16 a). The corresponding ensembles are shown in figure 3.16 b) to f), indicated by the colored panel denotation. The red and green dots mark two scan positions that are located in free space. In free space, the illumination does not illuminate the object and there is nothing that can vibrate. For such a situation, it is fair to say that the ER may yield undefined behavior and cause artifacts. The corresponding ensembles in figure 3.16 d) and e) have a unreasonable shape. It is concluded that this introduces the pattern.

In contrast, the blue and cyan scan positions are located on the object. The corresponding ensembles in b) and c) indicate a vibration that is stronger in the horizontal dimension. This is in agreement with the vibration characterization at PtyNAMi in figure 3.1. The shape of the ensembles is reasonable.

The magenta scan position is close to the platinum pedestal created in the FIB. The shape of the platinum pedestal is roughly recognizable in the corresponding ensemble in f). This is a similar effect as for the Siemens star reconstruction in figure 3.8. In that region, the object is translation invariant along the edge of the projected surface of the platinum pedestal.

3.5 Implementation Details and Performance

The ensemble refinement has been implemented into `ptycho`. Since the ER only consists of regular ptychographic operations, `ptycho` had already most of the necessary functionalities. The NNLS fit had to be added and originates from Lawson and Hanson. The implementation is Fortran to C translated using the `f2c` software from the original version [90]. The implementation runs on the Central Processing

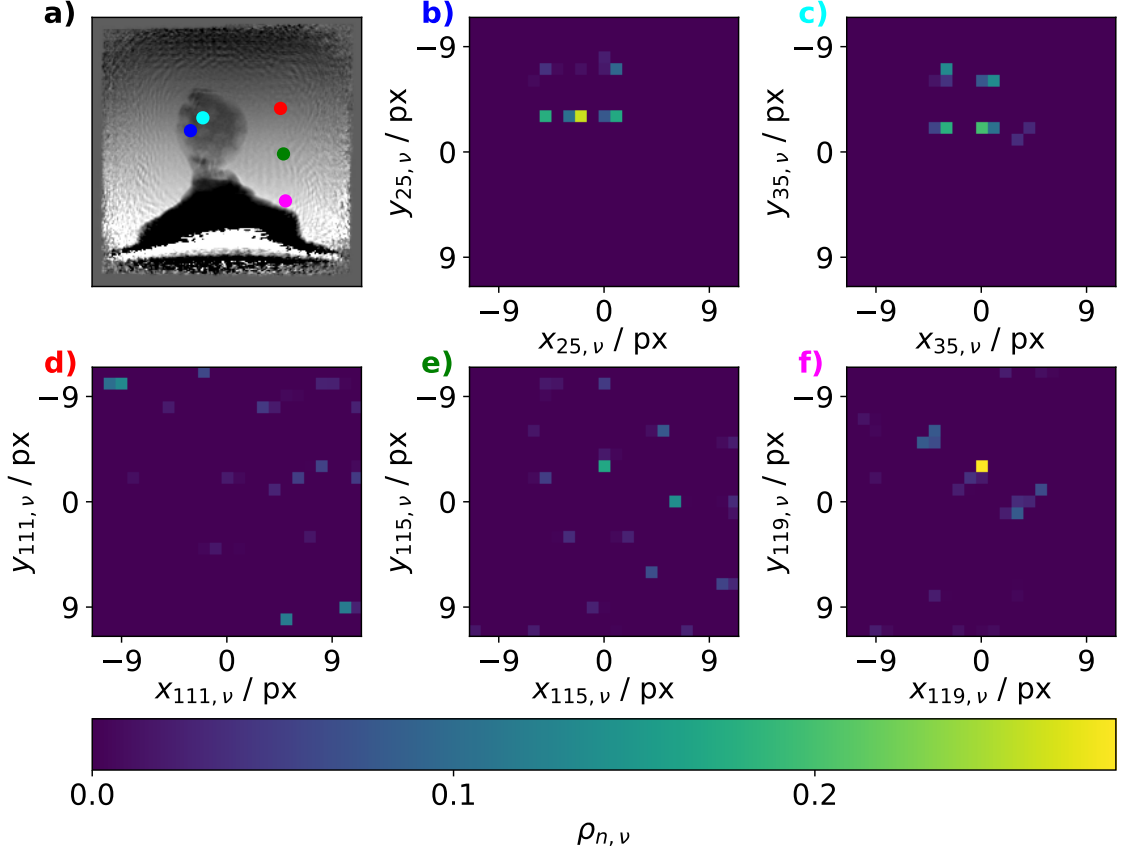


Figure 3.16: Illustration how the weights $\rho_{n,v}$ of different scan positions look like. a) The ER $r_e = 11$ reconstruction. The five colored dots mark five different scan positions. b) to f) The corresponding ensembles of the marked scan positions in a), indicated by the colored panel denotation. The blue and cyan scan positions are located on the zeolite particle and the ensembles in b) and c) have a reasonable shape. The red and green scan positions are located in the free space around the particle. The ensembles in d) and e) have an unreasonable shape. The magenta scan position is located close to the platinum pedestal. The ensemble recreates the shape of the projected surface of the platinum pedestal.

Unit (CPU) and utilizes a single core.

In the following, a benchmark is done on the zeolite dataset, which consists of 121 diffraction patterns and each pattern has dimensions of $256 \text{ px} \times 256 \text{ px}$. The performance scales with the amount of members n_e in the ensemble, which is given by

$$n_e = (2r_e + 1)^2. \quad (3.10)$$

The utilized hardware resources are an AMD EPYC 7543 and an Nvidia A100.

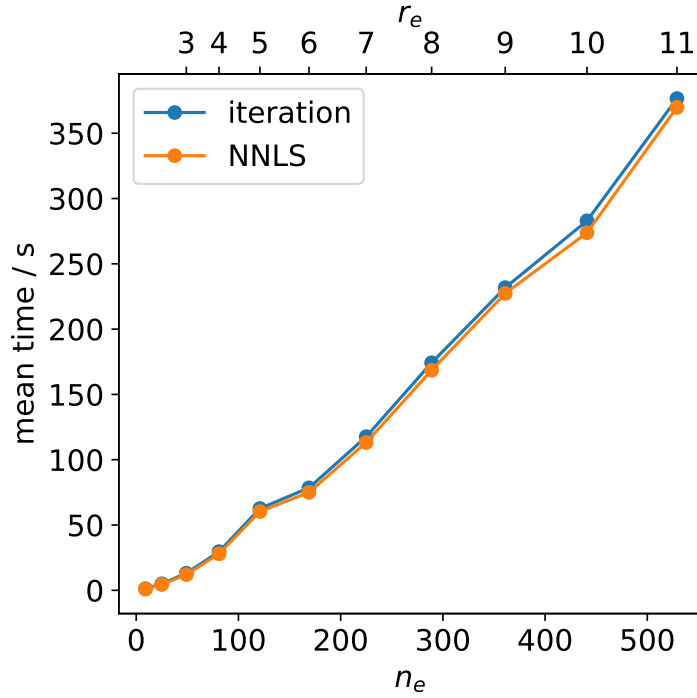


Figure 3.17: The mean iteration time of the ER drawn against the amount of members in the ensembles n_e .

Figure 3.17 shows the mean time per iteration that has been calculating by averaging the time of 50 iterations. The blue curve is the mean iteration time, the orange curve is the mean time that the NNLS fit consumes. There is a rough linear dependency between the mean iteration time and the amount of ensemble members. The NNLS fit clearly consumes most of the runtime.

However, it is emphasized that the performance of the ER is reduced drastically apart from the NNLS fit. For every ensemble shift $\vec{r}_{n,\nu}$, at least the forward model is fully applied, including the propagation via Fourier transform \mathcal{F} . Considering an ER reconstruction with $r_e = 11$, the ensembles have 529 members each. For a dataset with 121 diffraction patterns, this means that the ER processing of a single diffraction pattern is more computational effort than an entire ePIE iteration of the full dataset.

3.6 Conclusion

The novel approach of the Ensemble Refinement (ER) has been introduced, that can correct the effects of vibrations that occur during the experimental data acqu-

sition. The ER has been first tested on a simulated dataset and then applied to two experimental datasets: The Siemens star and the zeolite particle. The ER has shown a consistent improvement for all datasets. The achieved quality is stable against the ensemble size r_e . The spatial resolution of the Siemens star has been determined by line profiles and shows an improvement of at least factor 2.

A precise description of the ER behavior is dependent on many factors, such as the shape and structure of the object and illumination, the overlapping rate, noise, and partial coherence. A sufficient amount of overlap has been determined to be crucial for a successful ER reconstruction. The Siemens star dataset has an illumination with a diameter of about $1\ \mu\text{m}$ and a scanning step size of $250\ \text{nm}$, which gives roughly an overlap of 4. The zeolite dataset has an illumination with a diameter of $1.8\ \mu\text{m}$ and a scanning step size of $400\ \text{nm}$, which gives roughly an overlap of 4.5. For both datasets, the ER worked reliably. The author can report that the ER is working less reliably when the overlap is reduced such that this factor is as low as 2. Furthermore, both datasets utilized a defocused illumination that has a strong phase profile.

The Siemens star reconstructions have demonstrated how the ER introduced artifacts in regions where the projected object is translation invariant under a certain direction. A similar scenario is the empty region around the zeolite particle. To counteract, regularization or constraints can be incorporated to the NNLS fit to prevent the ensemble from getting an unreasonable shape.

One limitation of the current implementation is the long runtime, mostly due to the NNLS fit. Future work should first address an optimization of the NNLS fit. On the one hand, a more recent mathematical NNLS approach can be utilized, such as the approaches by Myre, et al., [92] or Diakonikolas, et al. [93]. Both approaches claim to have a better mathematical determination, that yields a significantly improved performance by at least an order of magnitude compared to the NNLS fit by Lawson and Hanson [90]. On the other hand, the current NNLS fit runs on a single CPU core and a new implementation should utilize a GPU, which is also consistent with the other functionalities of `ptycho`.

One may also want to utilize a parallel ptychographic algorithm, such as DM, so that the processing can be distributed among multiple GPUs. Utilizing DM can also be beneficial because the refinement of the object and illumination is done against all diffraction patterns simultaneously. The reconstruction is less influenced by local changes due to the update from individual diffraction pattern. The application of the ER to other ptychographic algorithms is straight forward. One can also utilize refPIE, that allows to reconstruct thick objects without phase wraps [52].

4 Streaming Ptychography

This chapter presents the development of online ptychography in streaming mode. Online, or live, means the diffraction patterns are reconstructed on-the-fly while the experimental data acquisition is still running. Streaming means the diffraction patterns are transmitted from the detector to the reconstruction instance via network. Online ptychography has been demonstrated before by Weber, et al., in file reading mode, such that the diffraction patterns are read from the storage system [94].

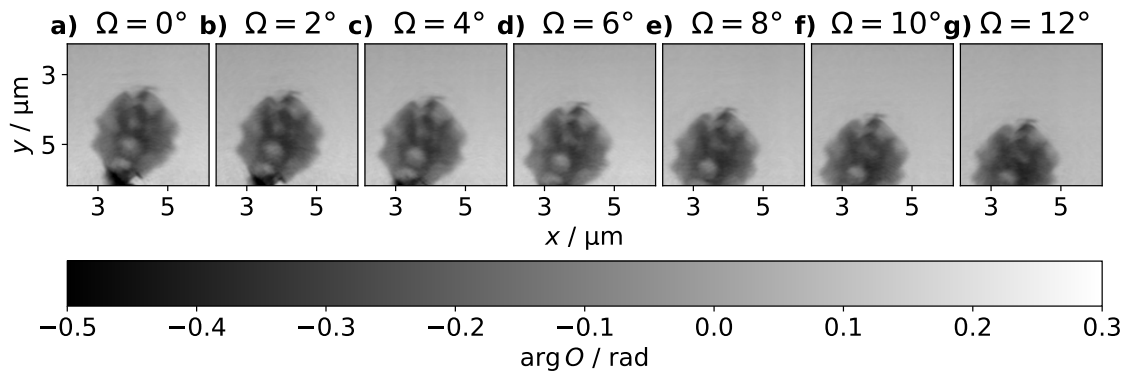


Figure 4.1: Illustration of the sample drift during a ptychographic tomographic scan. a) to g) Each image shows a ptychographic projection of a zeolite particle for a projection angle Ω given in the title. Each projection was acquired with the same scan range. The sample drifts vertically about $1 \mu\text{m}$ over the course of 12° .

Conventionally, ptychography is done offline, which means the data evaluation is performed as a subsequent step once the data acquisition is completed. A ptychographic scan for a third generation synchrotron source such as PETRA III consumes typically minutes to hours. The subsequent reconstruction may consume a similar amount of time. The downside of the offline procedure is that the user has no feedback until the reconstruction is performed.

A typical mistake when performing a ptychographic scan is the adjustment of a wrong scan region. Consider the ptychographic projections of the zeolite particle shown in figure 4.1 a) to g). The sample is rotated consecutively by 2° . The sample drifts vertically more than $50 \text{ nm}/^\circ$. When doing ptychography offline, the sample drift is only noticed once a scan is completed. This problem can be tackled by doing ptychography online. Sample drifts or wrong set scan regions can be identified already during the scan, allowing to abort the scan and correct the scan region. By

doing so, valuable beamtime can be saved.

The development of streaming ptychography has been carried out at the COSMIC Imaging soft X-ray beamline 7.0.1.2 at the Advanced Light Source (ALS), Lawrence Berkeley National Laboratory (LBNL), Berkeley, California, United States of America [23].

Section 4.1 introduces how ptychography is done at the COSMIC Imaging beamline. Section 4.2 presents how streaming ptychography is implemented. This covers the transfer of diffraction patterns and object functions via network, and by which events the live reconstruction can be controlled. Section 4.3 demonstrates how the streaming reconstruction looks for the user. Section 4.4 elaborates why live ptychography still relies on doing an additional offline reconstruction in order to achieve the highest reconstruction quality. Section 4.5 summarizes the full pipeline for online and offline ptychography implemented at the COSMIC Imaging beamline. Finally, section 4.6 concludes the developments in this chapter.

4.1 Ptychography at the COSMIC Beamline

The COSMIC Imaging beamline 7.0.1.2 operates at energies between 250 eV and 2500 eV. The distance between the sample and detector is 0.121 m. The detector is a fast Charge Coupled Device (CCD) camera and further described in section 4.1.1. The entire setup is located in vacuum. The sample is located on a Transmission Electron Microscopy (TEM) sample holder that is inserted horizontally into the vacuum chamber. The sample can be roughly positioned by coarse translation stages. The scanning is done using piezo translation stages that receive feedback from an optical interferometer system. The incoming beam is shaped by a FZP to a circular spot size of 45 nm. The sample is moved behind the focal plane to have a bigger illumination size irradiating the sample. The out of focus distance d_f is given by the illumination energy E and follows the relation

$$d_f = \frac{E * 15 \mu\text{m}}{700 \text{ eV}}. \quad (4.1)$$

4.1.1 Fast CCD Detector and Preprocessing

The raw dimensions of a detector image are 1040 px and 1152 px along the vertical and horizontal dimension, respectively. The detector pixels have a size of $30 \mu\text{m} \times 30 \mu\text{m}$. The detector consists of two panels that are divided by a horizontal gap. A raw detector image of a ptychography scan is shown in figure 4.2 a). The diffraction

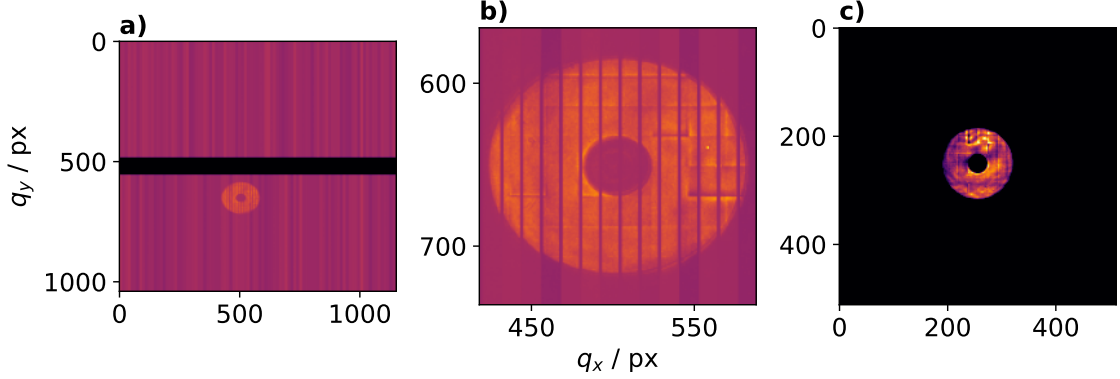


Figure 4.2: Illustration of the necessary preprocessing of the diffraction patterns. a) A raw diffraction pattern. A horizontal gap divides the two detector panels. Central in the image below the gap is the diffraction pattern visible. The vertical lines are the unphysical pixels that need to be removed. b) The magnified diffraction pattern. The horizontal grid is the morphological structure of the FZP. c) A preprocessed diffraction pattern that is suitable for ptychography.

pattern is located on the lower panel in the central region. Figure 4.2 b) shows a magnified view of the diffraction pattern. The detector contains unphysical pixels that are used to readout the detector. The readout pixels must be removed from the image. After removing, the detector image has a shape of $960 \text{ px} \times 960 \text{ px}$.

Further preprocessing of the raw diffraction patterns includes a background removal and an optional resampling. An additional feature is the creation of High Dynamic Range (HDR) like combined images. For this, two diffraction patterns per scan point are collected. One with a short exposure t_s , and a second with a longer exposure $t_l = 10t_s$. During the preprocessing, an image is assembled in which the shorter exposure imposes the high intense features of the diffraction pattern and the longer exposure imposes the low intense features.

A fully preprocessed diffraction pattern is shown in figure 4.2 c).

4.1.2 Illumination Initialization

The illumination P is initialized by the measured diffraction patterns I_n . This is demonstrated now for a dataset acquired at the COSMIC Imaging beamline consisting of 400 diffraction patterns. The energy of the illumination was 851.43 eV, giving an out of focus distance d_f of 18.24 μm utilizing equation 4.1. The distance between the sample and the detector was 0.121 m. A single diffraction pattern is

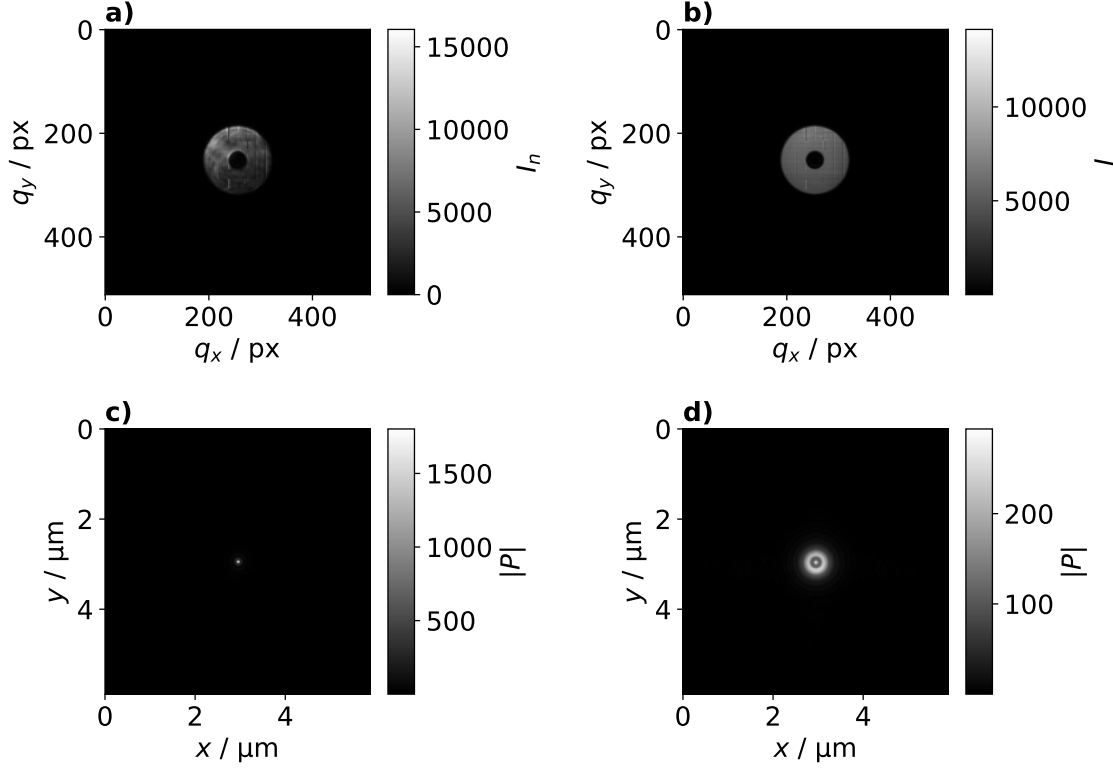


Figure 4.3: Illustration of the illumination initialization by diffraction patterns. a) A single diffraction pattern. b) The average of all diffraction patterns. c) The amplitude of the via inverse Fourier transform backpropagated average of diffraction patterns. This illumination is in focus. d) The illumination shown in c) has been defocused by Fresnel propagation.

shown in figure 4.3 a). The illumination initialization follows

$$P(\vec{r}) = \mathcal{N}_{d_f} \left[\mathcal{F}^{-1} \left[\sqrt{\frac{\sum_n^{\tilde{N}} I_n(\vec{q})}{\tilde{N}}} \right] \right]. \quad (4.2)$$

First, a certain amount \tilde{N} of the diffraction patterns I_n is averaged. For the demonstration in figure 4.3, all diffraction patterns are averaged, such that $\tilde{N} = N$. The average is shown in figure 4.3 b). Then, the square root of the average is backpropagated into the focal plane via inverse Fourier transform \mathcal{F}^{-1} , which is shown in figure 4.3 c). Afterwards, a Fresnel propagation \mathcal{N}_{d_f} according to the out of focus distance $d_f = 18.24 \mu\text{m}$ is done, which is shown in figure 4.3 d). For offline ptychography, all diffraction patterns N would be used for the illumination initialization, such that $\tilde{N} = N$.

4.2 Implementation

4.2.1 ZeroMQ

In order to do streaming ptychography, the acquired diffraction patterns and some metadata about the scan need to be transmitted via network into the reconstruction instance. The network transfer is done using the ZeroMQ library. ZeroMQ is a C library that is well suited for the streaming of big amounts of data. ZeroMQ offers bindings to various programming languages, such as C++ and Python, which covers the scope of this thesis.

ZeroMQ has different functionalities for sending data. Here, the publish-subscribe pattern is used. The idea is that there is one publisher that can have an arbitrary amount of subscribers. The subscriber can receive the data that the publisher sends, but the subscriber cannot communicate to the publisher.

Messages are send under a certain topic, which is a byte sequence at the beginning of the message. The subscriber must subscribe to a certain topic to receive the related messages. In order to use the ZeroMQ topics conveniently, there exist the ZeroMQ multipart functionality. The two functions `sendmultipart` and `recvmultipart` allow to send and receive multiple parts of a message, respectively.

4.2.2 Network Transfer of Images

To transfer an image utilizing ZeroMQ, the image has to be serialized. Serialization is the process of translating an image into a byte sequence, the counter process is called deserialization and refers to the translation of a byte sequence back into the image. There are different possibilities depending on the programming language. A pythonic way is pickle, which works fluently with NumPy arrays. The downside of utilizing pickle is that serializing or deserializing the image from a different programming language such as C++ is more complicated. Other options exist, such as msgpack, which are available to a variety of programming languages. However, during the development of streaming ptychography it has been collaboratively decided to do a custom image serialization and deserialization. By doing so, there is no dependency to a specific library or programming language. The custom serialization and deserialization is described in the following.

An image is split up into a metadata part and a data part. The metadata is a JavaScript Object Notation (JSON) container containing the shape, datatype, element order and byte order of the image. Additional details about the metadata are given in table 4.1. JSON containers can be serialized flawlessly. The data part

is just the byte sequence of all concatenated matrix elements of the image.

Table 4.1: Necessary metadata to serialize and desrialize an array.

Key	Value
<code>dtype</code>	A string indicating the datatype of the matrix elements. The string is a concatenation of either <code>uint</code> , <code>int</code> , <code>float</code> , <code>complex</code> and the bit-depth. E.g. <code>'uint8'</code> , <code>'int16'</code> , <code>'float32'</code> , <code>'complex64'</code> . For complex numbers, <code>'complex64'</code> means 32 bit float values for the real part and 32 bit float values for the imaginary part.
<code>shapex</code>	The amount of pixels along the x direction.
<code>shapey</code>	The amount of pixels along the y direction.
<code>order</code>	Can be <code>'C'</code> or <code>'F'</code> . <code>'F'</code> indicates the array is Fortran-style, i.e. y is the fast axis. <code>'C'</code> indicates C-style, i.e. x is the fast axis.
<code>byteorder</code>	Can be <code>'<'</code> , <code>'=''</code> , or <code>'>'</code> . <code>'<'</code> indicates little-endian, i.e. the most significant byte is first. <code>'=''</code> and <code>'>'</code> indicate big-endian, i.e. the most significant byte is last.

The metadata and the data are transmitted together using the ZeroMQ `sendmultipart` functionality. As elaborated in section 4.2.1, the topic of the message is always the first part, the metadata is the second part, and the data is the third part.

4.2.3 Events

The live reconstruction is controlled by four different incoming events: `start`, `frame`, `stop`, and `abort`. Additionally, there is the outgoing `rec` event that publishes the current reconstruction so that it can be received by a visualizing endpoint. An event is just a ZeroMQ multipart message with the event name as the ZeroMQ topic. The events are described in more detail in the following sections.

Since it can be confusing to have publisher and subscriber agree on the same topics and JSON keys, there are two publicly available repositories that give some helping utilities for C++ [95] and Python [96]. When publisher and subscriber both utilize the same repository, all ZeroMQ topics and JSON keys match automatically.

`start`

The `start` event communicates to the reconstruction instance that a scan begins. It is a ZeroMQ multipart message consisting of two parts: The first part is the serialized topic `start`, the second part is a serialized JSON data container that holds metadata about the scan. The metadata is given in table 4.2. An `identifier` is transmitted

that the reconstruction instance utilizes to recognize the current measurement. The metadata is further used to estimate size shape of the object. An initial guess for the illumination can be transmitted. The parameter `dp_fraction_for_illumination_init` defines the fraction of diffraction patterns that needs to be received before the live begins to iterate.

When a `start` event is received and a reconstruction is already running, the current reconstruction is stopped and the current state is written to disk. Then, the new reconstruction begins.

Table 4.2: The metadata of the `start` event.

Key	Value
<code>identifier</code>	A string indicating the name of the current scan.
<code>translations</code>	A list of lists holding the nominal (x, y) scan positions of the diffraction patterns in m.
<code>energy</code>	Energy of the illumination in J.
<code>distance</code>	Distance between the sample and detector in m.
<code>output_frame_width</code>	Edge length of the diffraction patterns in pixel.
<code>dp_fraction_for_illumination_init</code>	Fraction of diffraction patterns necessary to be received before the reconstruction begins.
<code>x_pixel_size</code>	Edge length of one detector pixel in m.
<code>illuminationreal</code>	A C-style 2D float list holding the real part of the illumination.
<code>illuminationimag</code>	A C-style 2D float list holding the imaginary part of the illumination.

frame

The `frame` event transmits a diffraction pattern to the reconstruction instance. It is a ZeroMQ multipart message consisting of three parts. First, the serialized topic `frame`. Second, the metadata of the image given in table 4.1 as a serialized JSON data container. Third, the image elements as bytes. Additionally, the JSON data container contains the dataset name, the index of the diffraction pattern and the y and x coordinate of the scan position. The respective JSON keys of the additional metadata are given in table 4.3.

It is essential that the `start` event is received by the reconstruction instance before the first diffraction pattern arrives. With the `start` event, an `identifier` is transmitted. When the `identifier` of an arriving diffraction pattern does not match the `identifier` of the `start` event, the diffraction pattern is ignored.

Table 4.3: The additional metadata of the `frame` event.

Key	Value
<code>identifier</code>	A string indicating the name of the current scan.
<code>index</code>	The index of the diffraction pattern.
<code>posy</code>	The y position of the diffraction pattern in m.
<code>posx</code>	The x position of the diffraction pattern in m.

stop

This event indicates that a scan has completed. The reconstruction instance treats a received `stop` event equivalent as successfully transmitting all diffraction patterns to the reconstruction instance. Whenever one of the scenarios happens, the reconstruction instance will continue iterating for the amount of configured iterations. The `stop` event is a ZeroMQ multipart message consisting of two parts: First, the serialized topic `stop`. Second, a serialized JSON data container that only contains an `identifier`, as shown in table 4.4.

Table 4.4: The metadata of the `stop` and `abort` event.

Key	Value
<code>identifier</code>	A string indicating the name of the current scan.

abort

This event indicates that a scan has been aborted. When received, the reconstruction instance will stop iterating and write the current state of the reconstruction to disk. It is a ZeroMQ multipart message consisting of two parts: First, the serialized topic `abort`. Second, a serialized JSON data container. Similar as for the `stop` event, the JSON container only contains an `identifier`, as shown in table 4.4.

rec

This is an outgoing event of the reconstruction instance that publishes the current reconstruction so that it can be visualized while the scan is still running. The `rec`

event is a ZeroMQ multipart message consisting of three parts. First, the serialized topic `rec`. Second, a serialized JSON data container. Third, the concatenated bytes of the image elements. The JSON container contains the image metadata, an `identifier` and the real space pixel size in x and y of the reconstruction, such as shown in table 4.5. The real space pixel size can be used to add a scale bar to the visualization of the reconstruction.

Table 4.5: The metadata of the `rec` event.

Key	Value
<code>identifier</code>	A string indicating the name of the current scan.
<code>obj_pixelsize_x</code>	The real space pixel size of the reconstruction along the x axis in m.
<code>obj_pixelsize_y</code>	The real space pixel size of the reconstruction along the y axis in m.

4.2.4 `ptycho`

The COSMIC Imaging beamline has its own implementation for ptychography: `ptychocam`. Streaming ptychography has been first implemented to `ptychocam` and later to `ptycho`. Since this thesis presents developments made to `ptycho`, a thorough introduction to `ptychocam` is skipped and only general information are summarized explaining key functionalities of `ptycho`.

Offline, `ptychocam` is started with a `cxi` file [97] that contains all information to perform a ptychographic reconstruction. In streaming mode, `ptychocam` is started without a `cxi` file and all necessary information must be transmitted via the `start` event, such as the energy, the distance between sample and detector, and so forth. Furthermore, `ptychocam` does not have the functionality to initialize an illumination, such that one is transmitted via the `start` event.¹

Since the streaming mode for `ptycho` was initially developed for operation at the COSMIC Imaging beamline, `ptycho` supports all of these features, too. However, `ptycho` does not rely on these information given by the `start` event. In streaming mode, `ptycho` is still started with its usual configuration file, and when the `start` event does not have any of the information, they are taken from the configuration file. The only mandatory metadata are the nominal translations, `ptycho` still relies on these to set up the shape of the reconstructed object.

¹It would be trivial to implement an illumination initialization to `ptychocam`, but the idea of `ptychocam` is to reconstruct a fully preprocessed `cxi` file.

It is further stressed that one has to specify a reasonable object enlargement in the `ptycho` configuration file, since the nominal object shape may be too small to incorporate the translations measured by the encoders or interferometers. The nominal object shape is also too small when performing a fly scan at PtyNAMi. For a fly scan, the amount of scan positions exceeds the amount of nominal scan positions, because the collection of detector images continues when the translation stages turnaround at the end of a line.²

4.3 Demonstration of the Streaming Reconstruction

The `ptycho` live reconstruction is now demonstrated to exemplarily illustrate the impression for the user. However, the demonstration is created in a testing scenario. The reconstructions shown here were not created during a measurement at the beamline. Instead, a dataset acquired at the COSMIC Imaging beamline is used to simulate the ZeroMQ streams to `ptycho`.

The simulation mimics a scan consisting of 400 diffraction patterns in total. The sample is scanned on a grid with 20 steps each along the vertical and horizontal dimension. The step size is 80 nm horizontally and vertically, giving a nominal scan window of $1.52\ \mu\text{m} \times 1.52\ \mu\text{m}$. The distance between the sample and the detector is 0.121 m. The energy is 851.43 eV and the corresponding out of focus distance is $d_f = 18.24\ \mu\text{m}$. The illumination has roughly a size of 750 nm in the object plane. The diffraction patterns are cropped to a size of $512\ \text{px} \times 512\ \text{px}$. The illumination is initialized with 40 of the 400 diffraction patterns using equation 4.2. The parameter `dp_fraction_for_illumination_init` is set to 0.1. With these parameters, the `start` event is send to the reconstruction instance and it is waited for 1 s. Then, the diffraction patterns are send every 20 ms.

Different snapshots of the live reconstruction are shown in figure 4.4. From a) to e), it is visualized how the live reconstruction looks after 20 % to 100 % of the diffraction patterns have arrived, in steps of 20 %. The fraction of arrived diffraction patterns is given in the title of each image together with the iterations done so far. Once all diffraction patterns arrived, the reconstruction continues for another 500

²In principle, `ptycho` could be started in streaming mode without any metadata at all, meaning also without the translations. However, this would mean the size of the reconstructed object cannot be known in advance, and the object is continuously extended with every arriving diffraction pattern. While this is technically fine, it is a confusing impression for the user when the object continuously grows. Hence, this feature has not been implemented and `ptycho` relies on a matching object shape from the translations in the start event and the specified object enlargement.

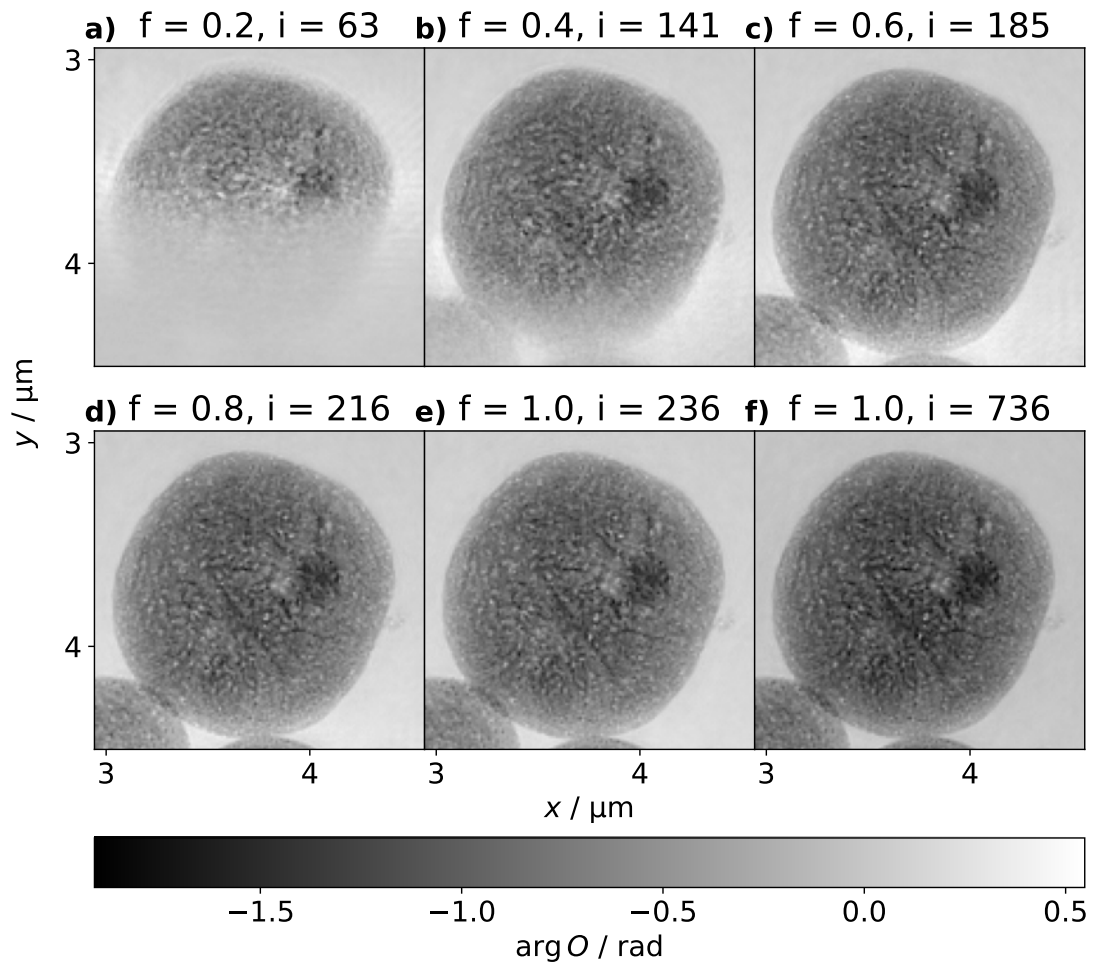


Figure 4.4: An illustration of the streaming reconstruction. a) to e) The images show the reconstruction after 20 % to 100 % of the diffraction patterns have arrived, in steps of 20 %. This is also indicated by the factor f in the title. The amount of iterations is denoted by i in the title. f) The reconstruction after all diffraction patterns have arrived and an additional 500 iterations.

iterations, that has been specified in the `ptycho` configuration file. The final result is visible in figure 4.4 f).

Due to the illumination size of roughly 750 nm and the step size of 80 nm, there is a high degree of overlap. Only 20 % of the diffractions pattern have been processed by the live reconstruction in figure 4.4 a), but roughly half of the object can be identified. At 40 % arrived diffraction patterns in figure 4.4 b), the morphology of the full object can already be estimated.

4.4 Offline Reconstructions

During the development of streaming ptychography, it has been realized that in most scenarios, the live reconstruction does not have the chance to fully converge. In a typical scenario at the beamline, a user will not perform a single ptychographic scan and wait until it is converged, but rather series of ptychographic scans. At the COSMIC Imaging beamline, these series are often spectroscopic scans with different illumination energies, or tomographic scans for different projection angles of the sample. Once the last diffraction pattern of one scan has been acquired, a new scan will start immediately. A new scan will transmit a **start** event to the reconstruction instance and the current reconstruction is stopped. The last diffraction pattern has arrived just briefly before the new **start** event. The live reconstruction can use the the last arriving diffraction patterns only for a couple of iterations.

To counteract, a pipeline has been developed to automatically perform an offline reconstruction of the acquired data. The offline reconstruction is meant to fully converge and less dependent on performance. Slower algorithms with the potential for a higher reconstruction quality can be utilized, such as the ER introduced in chapter 3 or the maximum-likelihood refinement by Thibault and Guizar-Sicairos [98].

4.5 Pipeline

Summarizing what has been introduced in this chapter, the ptychography pipeline at the COSMIC Imaging beamline must include the preprocessing of the diffraction patterns, the reconstruction in streaming mode, and the offline reconstruction.

The resulting pipeline is shown in figure 4.5. The user interacts with the frontend PYSTXM GUI. The GUI communicates with the backend server `pystxmcontrol`. The backend communicates with the CCD detector and initializes the acquisition of a detector image via the CCD Interface. The CCD Interface streams the acquired raw diffraction pattern back into the backend `pystxmcontrol`. From here, `pystxmcontrol` streams the raw diffraction pattern into PYSTXM GUI so that the user can inspect it. Furthermore, `pystxmcontrol` writes the raw diffraction pattern into a `hdf5` file and streams the raw diffraction pattern into the Live Preprocessor.

The Live Preprocessor does all of the preprocessing described in section 4.1.1 and the illumination initialization described in section 4.1.2. The preprocessed diffraction pattern is written by the Live Preprocessor into a `hdf5` file in `cxi` format. Once 10% of the diffraction patterns have arrived, the Live Preprocessor initializes an

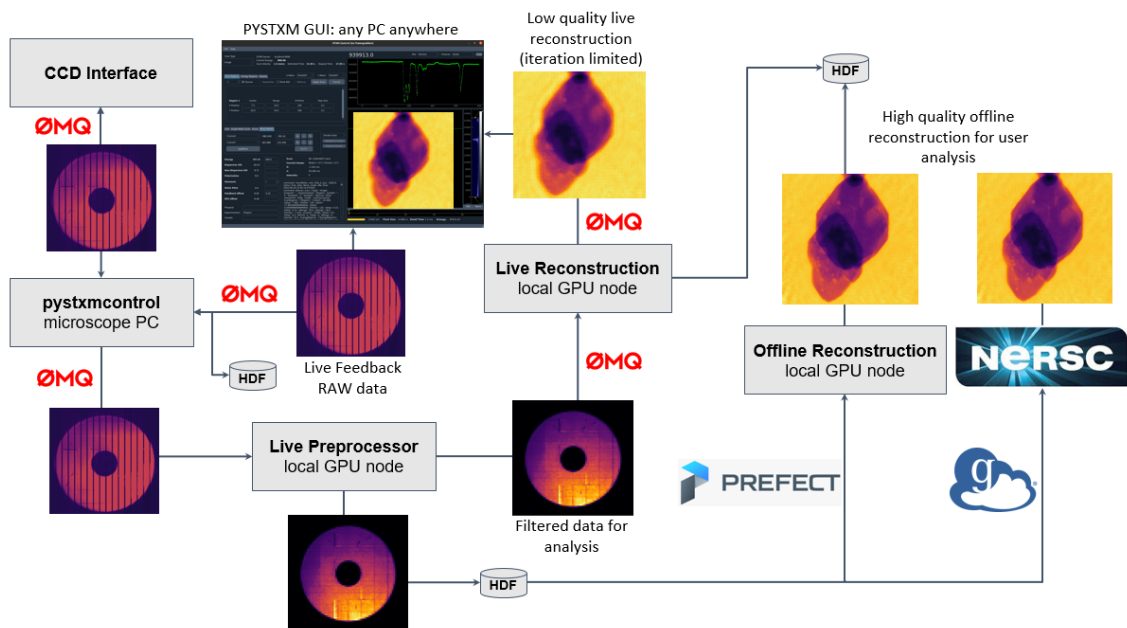


Figure 4.5: The ptychography pipeline at the COSMIC beamline. The pipeline consists of an online preprocessing and reconstruction of the diffraction data. Furthermore, there is an automated mechanism to perform offline reconstructions at local workers at the beamline or at the National Energie Research Scientific Computing Center (NERSC). A thorough description of all components is given in section 4.5.

illumination and sends the `start` event to the Live Reconstruction instance, which could be either `ptychocam` or `ptycho`. Then, the Live Preprocessor begins streaming of the preprocessed diffraction pattern into the Live Reconstruction.

The Live Reconstruction streams the current state of the reconstructed object every 0.1s into PYSTXM GUI, so that the user can inspect it.

When all preprocessed diffraction patterns are written into the `cxi` file, an offline reconstruction is initialized. For this, there are two possibilities. First, an offline reconstruction is performed on a local GPU node at the COSMIC Imaging beamline. This is done by triggering a Prefect workflow. In a simplified picture, Prefect can act as Slurm and allows to automatically trigger and monitor computing jobs.

Second, a GLOBUS data transfer is triggered that transports the finished `cxi` file to the Perlmutter supercomputer at NERSC. Once the `cxi` file has arrived, an offline reconstruction is triggered as a Slurm job via an HTTP request to the NERSC Superfacility API. The offline reconstruction is executed as a containerized version of the reconstruction software `ptychocam` or `ptycho`.

For low data rates, the local GPU nodes at the COSMIC beamline may be sufficient to reconstruct all acquired datasets in a suitable amount of time. For high

data rates, the computing capabilities of the Perlmutter super at NERSC can be utilized.

4.6 Conclusion

In this chapter, online ptychography in streaming mode has been developed for operation at the COSMIC Imaging beamline. By the time of writing this thesis, the live reconstruction was in continuous operation. The live reconstruction is part of a pipeline that includes an additional offline reconstruction with highest quality for postprocessing.

The favorable conditions for ptychography at the COSMIC Imaging beamline give rise to the applicability of the live reconstruction. The ptychographic reconstruction gives a good quality image already after a couple of iterations, as shown in figure 4.4. Furthermore, the large illumination leads to a reconstruction of the scan window before the scan is completed. This enables a real time feedback of the running scan for the user. The PYSTXM GUI in figure 4.5 is the only point of interaction that the user needs to control the ptychographic microscope.

It is stressed that the pipeline in figure 4.5 is the result of a collaboration. David Shapiro is the manager of the COSMIC Imaging beamline and responsible for `pystxmcontrol`, PYSTXM GUI and the reconstruction software `ptychocam`. Abraham Levitan wrote the Live Preprocessor. Yanqi Luo und Dylan McReynolds implemented the Prefect infrastructure and the GLOBUS data transfer to NERSC.

The contributions of the author Silvio Achilles are as follows. The author developed the streaming structure in section 4.2 and implemented it to `ptycho`, `ptychocam` and the Live Preprocessor. Furthermore, the author developed the mechanism to automatically perform offline reconstructions at the local beamline machines and the Perlmutter supercomputer at NERSC.

5 Coupled Ptychographic Tomography

Coupled Ptychographic Tomography (CPT) gained increasing interest in recent years [28], [29], [72], [99], [100]. The approach has been introduced in section 2.4.3. The procedure has been proven to work on experimental data by Kahnt, et al. [29]. The runtime of their implementation is about one week for 50 iterations. The objective of this work is to develop a GPU-accelerated implementation that allows to perform CPT reconstructions in a suitable time. The developed implementation is referred to as `ptycho3d`.

Section 5.1 presents how `ptycho3d` is implemented and what libraries are used. Section 5.2 introduces the dataset of the zeolite catalyst particle. This dataset is used to benchmark `ptycho3d`. Section 5.3 demonstrates the functionality of `ptycho3d` by creating reconstructions with different ptychographic and tomographic algorithms. Section 5.4 presents the achieved performance. Section 5.5 gives insight into another benefit of CPT, which is to use 2D ptychographic position correction procedures during the combined ptychographic tomographic reconstruction. Finally, in section 5.6, the achieved results are summarized and an outlook for future developments is given.

5.1 Implementation Details

The developed GPU-accelerated CPT implementation `ptycho3d` is derived of the ptychography software `ptycho`, which has been introduced in section 2.2.6. Therefore, `ptycho3d` is written in C++ and utilizes the CUDA library for GPU-accelerated calculations. The tomographic components are added from the ASTRA-Toolbox, which is fortunately written in C++/CUDA, too [86].

The ptychographic algorithms ePIE, pePIE, and refPIE and the tomographic algorithms BP, SIRT, and CGLS can be utilized by `ptycho3d`. During the CPT reconstruction, `ptycho3d` updates the reconstructed 3D complex refractive index decrement $\nu(x, y, z)$ after each projection. Therefore, the SIRT algorithm is effectively SART [83]. Furthermore, the BP cannot be applied directly, since the ASTRA-Toolbox does not consider an existing volume when performing the BP. Nevertheless, `ptycho3d` utilizes the BP to update the reconstruction volume ν for a specific

projection angle Ω as follows

$$\nu'(x, y, z) = \nu(x, y, z) + \int_{-\infty}^{\infty} (\nu'_{\Omega}(t, y) - \nu_{\Omega}(t, y)) \tilde{\delta}(t - x \cos(\Omega) - z \sin(\Omega)) dt, \quad (5.1)$$

in which ν' denotes the updated volume, t denotes the projection coordinate and $\tilde{\delta}$ denotes the delta function. Equation 5.1 is a similar update as SART. Therefore, the tomographic update utilizing equation 5.1 is referred to as Backprojection-based SART (BP-SART). In section 5.4, it is shown that BP-SART yields a better performance in `ptycho3d` than the SIRT implementation of the ASTRA-Toolbox.

The tomographic operations in `ptycho3d` are performed on multiple GPUs. Distributing parallel-beam geometry tomographic operations on multiple GPUs is a triviality, since the projection and the volume can be divided into separate parts that do not interact with each other. A further benefit is that the reconstructed volume ν may consume a significant amount of GPU memory. By distributing ν among multiple GPUs, larger volumes can be reconstructed.

In principle, all features of `ptycho` are also available in `ptycho3d`. However, `ptycho3d` has not been tested for all possible scenarios and some features may require a more specified implementation, for instance using multi-beam or multi-slicing during the CPT reconstruction.

5.2 Sample and Experiment

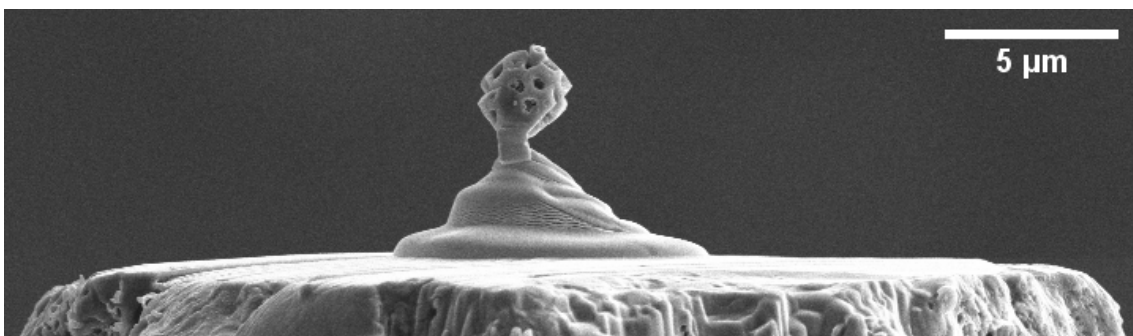


Figure 5.1: A SEM image of the zeolite particle. The particle has a diameter of roughly $2.7 \mu\text{m}$.

The sample is a macroporous zeolite catalyst particle that was measured at PtyNAMi in 2018 [29]. The sample is visible in figure 5.1. The incoming beam had an energy of 9 keV and was focused by a FZP to a circular spot size of 70 nm. The sample was positioned 1.0 mm behind the focal plane of the X-ray optics, yield-

ing an illumination size of $1.8\ \mu\text{m}$ in the object plane. The diffraction patterns were acquired with an Eiger X4M with a pixel size of $75\ \mu\text{m} \times 75\ \mu\text{m}$. The detector was positioned $2.13\ \text{m}$ behind the sample. The diffraction patterns are cropped to $256\ \text{px}$ along the vertical and horizontal dimension. The experimental geometry yields a real space pixel size of $16.57\ \text{nm}$ of the reconstructed object.

The sample was rotated over an angular range of 182° with a step size of 2° , yielding a total amount of 92 projections. For each projection, the sample was translated on a grid with a step size of $400\ \text{nm}$ and 11 steps horizontally and vertically. This yields a nominal scan window of $4\ \mu\text{m} \times 4\ \mu\text{m}$. The scan positions \vec{r}_n were measured with a set of optical interferometers.

The dataset acquisition as well as a prior data evaluation was done by Kahnt, et al. [29]. An essential part of nano-tomographic data evaluation is the alignment of the projections. The used projections in this thesis are aligned beforehand, which has been done by Maik Kahnt.

5.3 Ptychographic and Tomographic Reconstruction Algorithms

To demonstrate the functionality of `ptycho3d`, reconstructions are performed for all combinations of the ptychographic algorithms ePIE, pePIE, and refPIE and the tomographic algorithms BP-SART, SIRT, and CGLS. Each reconstruction ran for 100 iterations after which the contrast converged. For each projection, the illumination amplitude is initialized as a disk with a diameter of $1.8\ \mu\text{m}$ and the illumination phase is initialized by propagating a planar phase $1.0\ \text{mm}$ downstream. The illuminations are constrained during the reconstruction, such that the dosis in the reconstructed illumination matches the dosis of the brightest diffraction pattern. For ePIE and refPIE, the constraint is applied before the processing of each diffraction pattern. For pePIE, the constraint is applied at the beginning of every iteration. Each reconstruction ran for 100 iterations, after which the contrast of the reconstruction converged.

One central horizontal slice of the reconstructed volume is shown in figure 5.2 for each of the algorithm combinations. The reconstructed slices have similar quality. Neither the ptychographic nor the tomographic algorithm has a significant influence on the reconstruction quality.

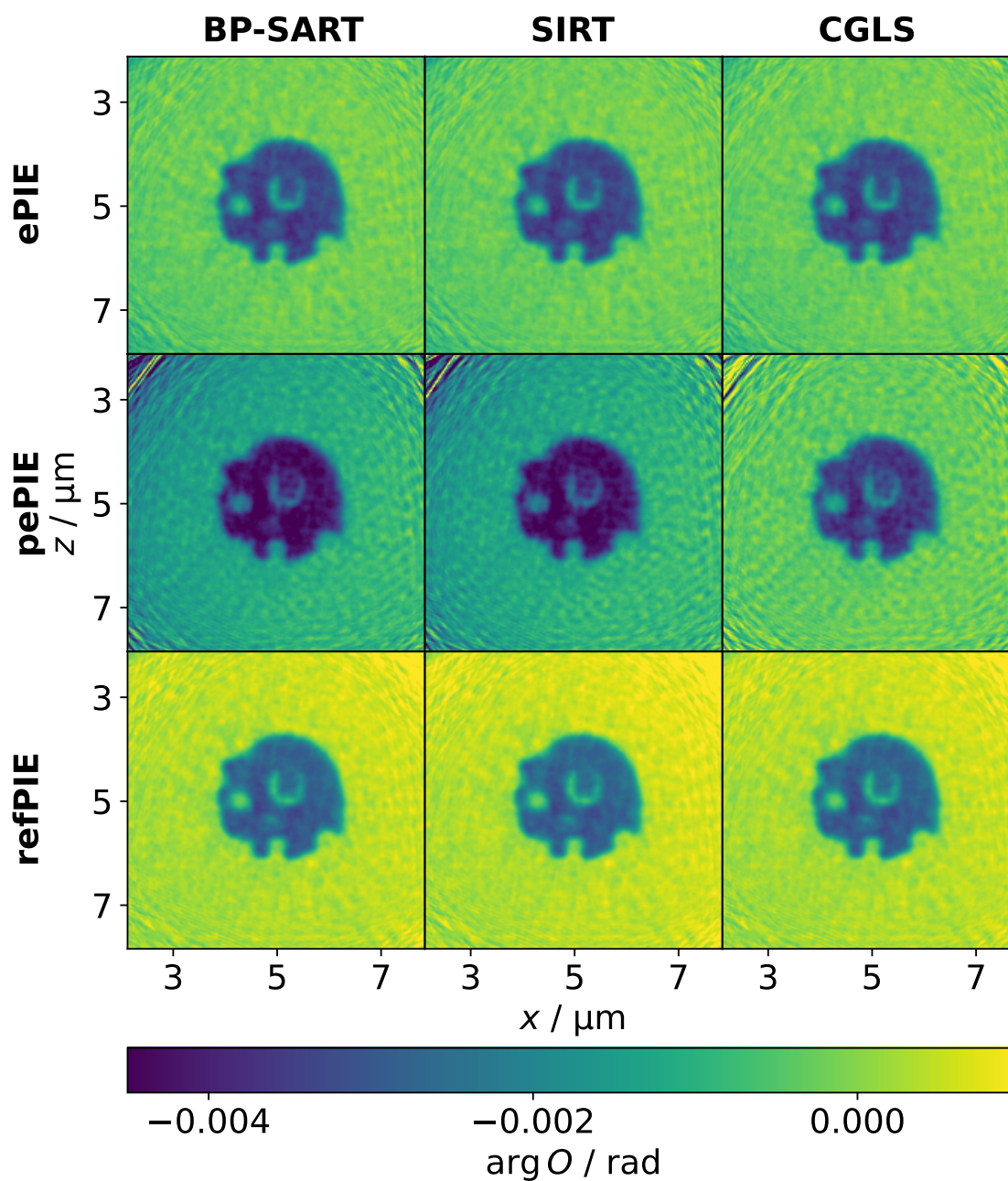


Figure 5.2: A summary of CPT results obtained by combining the ptychographic algorithms ePIE, pePIE, and refPIE and the tomographic algorithms BP-SART, SIRT, and CGLS. Each image shows one reconstructed slice of the zeolite dataset. Each of the combinations yields a similar reconstruction quality and no significant differences can be observed by visual inspection.

5.4 Performance

Theptychographic operations run on a single GPU and the tomographic operations can run on as many GPUs as available on the executing node. Figure 5.3 shows a benchmark of the zeolite dataset for all combinations ofptychographic and tomographic reconstruction algorithms. Each combination was iterated for 200 iterations, of which the mean iteration time is calculated. The benchmarks have been performed using Nvidia A100 GPUs. The dots in figure 5.3 show the mean iteration time versus the amount of utilized GPUs. The color of the dots denotes the tomographic algorithm. The titles in figure 5.3 denote theptychographic algorithm. The tomographic algorithm has a significant influence on the performance.

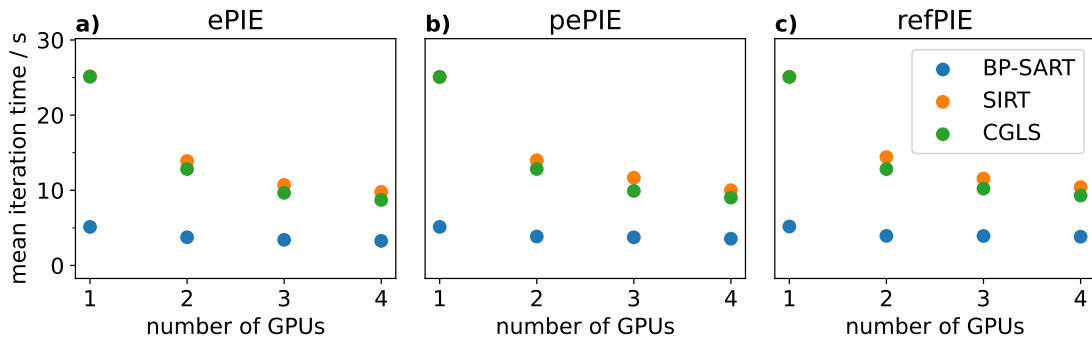


Figure 5.3: A CPT performance comparison for all combinations ofptychographic and tomographic reconstruction algorithms of `ptycho3d`. a) to c) The performance for the threeptychographic algorithms ePIE, pePIE, and refPIE. In each panel, the three tomographic reconstruction algorithms BP-SART, SIRT, and CGLS are denoted by the colored dots. The performance is mostly influenced by the tomographic reconstruction algorithm. The BP-SART gives the best performance.

For a single GPU, SIRT and CGLS have a mean iteration time about three times as high as BP-SART. However, for SIRT and CGLS, the mean iteration decreases significantly when using multiple GPUs.

The BP-SART performance is less increased by the amount of utilized GPUs. This may be due to the fact that the BP-SART is a mathematically much simpler operation and the additional overhead when initializing multiple GPUs instead of one equalizes the performance increase.

The runtime of the implementation by Kahnt, et al., is about seven days for 50 iterations utilizing ePIE and SIRT [29]. The runtime of `ptycho3d` for 50 iterations including IO operations is 201.75 s for BP-SART and 538.82 s for SIRT. This yields a respective performance increase by a factor of 2997 and 1122.

5.5 Position Refinement

A benefit of the combined mathematical description of ptychography and tomography is that additional ptychographic features can be utilized during the reconstruction, such as the 2D brute-force position refinement presented in section 2.2.6. The ptychographic position refinement is applied to the current state of the projected object-transmission function, but before the object function is updated in a certain iteration. Therefore, the scan positions are refined to be consistent with the reconstructed 3D complex refractive index decrement ν . This can yield a better alignment of the ptychographic projections.

Properly aligned projections are a requirement for high quality tomographic reconstructions. Generally, the experiment should be designed as stable as possible. However, the stability of rotation stages is not sufficient for nano-tomographic datasets with spatial resolutions significantly below $1\ \mu\text{m}$. In figure 4.1, it has been shown that the rotation at PtyNAMi causes the sample to drift for more than $50\ \text{nm}/^\circ$. The alignment of the projections is an essential part of the evaluation of nano-tomographic datasets.

The effect of the position refinement is first tested on a simulated dataset in section 5.5.1 and on the zeolite dataset in section 5.5.2.

5.5.1 Simulation Study

Dataset

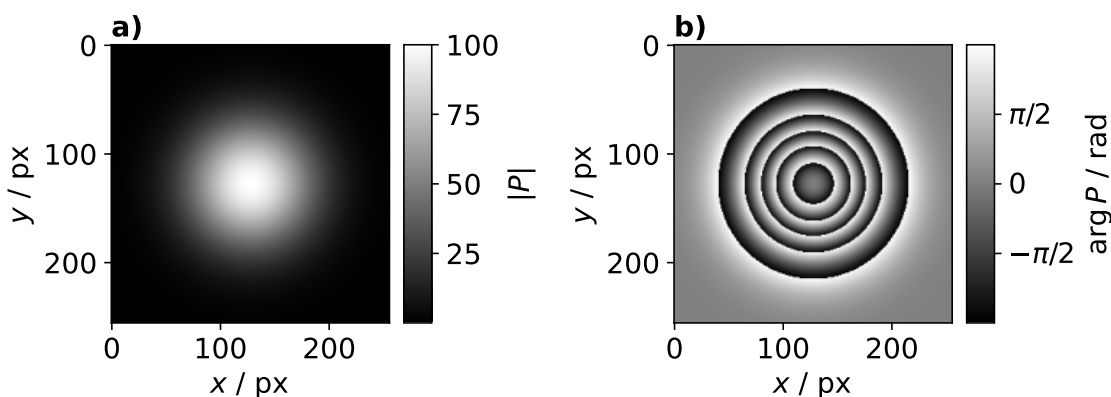


Figure 5.4: The illumination used for the simulation of the Shepp Logan dataset.

The object for the simulations is a 3D Shepp Logan phantom. The edge length of the 3D cubic volume is 808 px, which already includes the obligatory padding for ptychographic datasets by half the illumination size and 20 px object enlargement to

incorporate the position refinement shifts. The illumination has a gaussian-shaped amplitude and a gaussian-shaped phase shown in figure 5.4 a) and b), respectively. The energy of the illumination is 9 keV, the distance between the sample and the detector is 3 m, and the detector has a pixel size of $75 \mu\text{m} \times 75 \mu\text{m}$. However, the discussion throughout this section will be carried out based on the pixel coordinates. In total, 181 ptychographic projections are simulated over an angular range of 180° . Each projection consists of 441 diffraction patterns distributed on a regular grid with 21 steps in each dimension.

Two datasets are simulated: One dataset that has perfectly aligned projections. A second dataset that has the projections randomly misaligned horizontally and vertically by shifts in the range of -5 px to 5 px .

Reconstruction

The datasets are reconstructed as follows. The ptychographic and tomographic reconstruction algorithm is ePIE and BP-SART, respectively. For all reconstructions, the exact illumination is utilized and the illumination is not updated during the reconstruction, meaning $\beta = 0$ in equation 2.21. This is due to the fact that the illumination refinement can yield an improved projection alignment, too [29]. However, this section is dedicated to investigate the effect of only the position refinement on the projection alignment.

First, a CPT reconstruction of the perfectly aligned dataset is done. The reconstruction ran for 20 iterations, after which the contrast of the reconstruction converged. From the reconstructed projections, a sinogram of a central y position is created and shown in figure 5.5 a). The sinogram is perfectly continuous since there is no misalignment. The corresponding slice of the reconstructed volume is shown in figure 5.5 d). The reconstruction has very good quality. The four colored lines mark features used for a line profile analysis later in this section.

Second, a CPT reconstruction without position refinement of the misaligned dataset is done. The reconstruction ran for 20 iterations, after which the contrast of the reconstruction converged. From the reconstructed projections, a sinogram of a central y position is created and shown in figure 5.5 b). The sinogram has discontinuities due to the misalignment. The corresponding slice of the reconstructed volume is shown in figure 5.5 e) and has a severely reduced quality due to the misalignment.

Third, a CPT reconstruction with position refinement of the misaligned dataset is done. As an initial guess for the object, the CPT reconstruction without position refinement of the misaligned dataset is used. The position refinement is applied

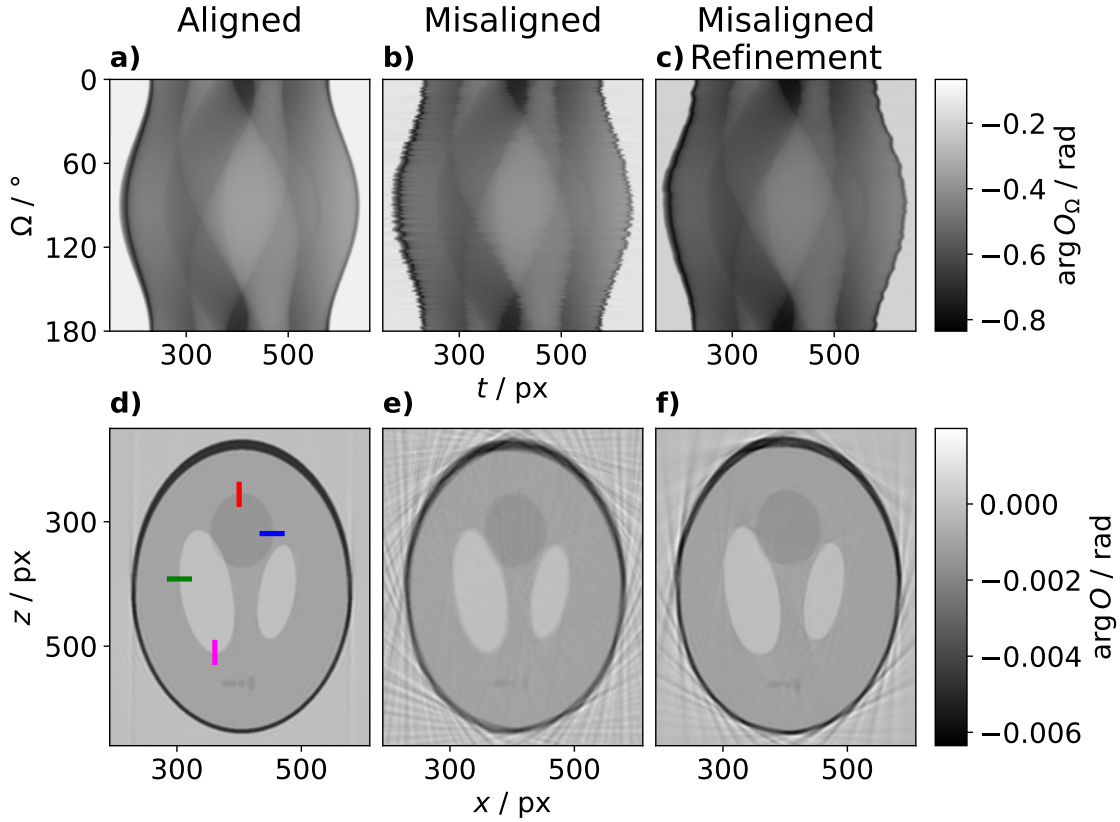


Figure 5.5: A demonstration of the effect of projection misalignment on the tomographic reconstruction. a) The sinogram of the reconstruction of the perfectly aligned dataset. b) The sinogram of the reconstruction of the dataset randomly misaligned by up to ± 5 px. The sinogram has discontinuities. c) The sinogram of the reconstruction that utilized position refinement for 50 iterations to the reconstruction state in b). The position refinement causes a better alignment of the projections and the sinogram is more continuous. d) The reconstruction of the aligned dataset. The object is properly reconstructed. e) The reconstruction of the misaligned dataset. The reconstruction quality is significantly reduced. f) The reconstruction with position refinement of the misaligned dataset. The position refinement causes an improved reconstruction quality compared to e).

in every iteration starting from the beginning of the reconstruction. The spread for the position refinement is $r_p = 5$ px, matching the maximum misalignment of the projections. The reconstruction ran for 200 iterations, after which no further improvement with more iterations could be observed. From the reconstructed projections, a sinogram of a central y position is created and shown in figure 5.5 c). The sinogram is significantly more continuous than the sinogram in b). The corresponding reconstruction is shown in figure 5.5 f). The reconstruction has an improved

quality compared to the reconstruction without position refinement in figure 5.5 e).

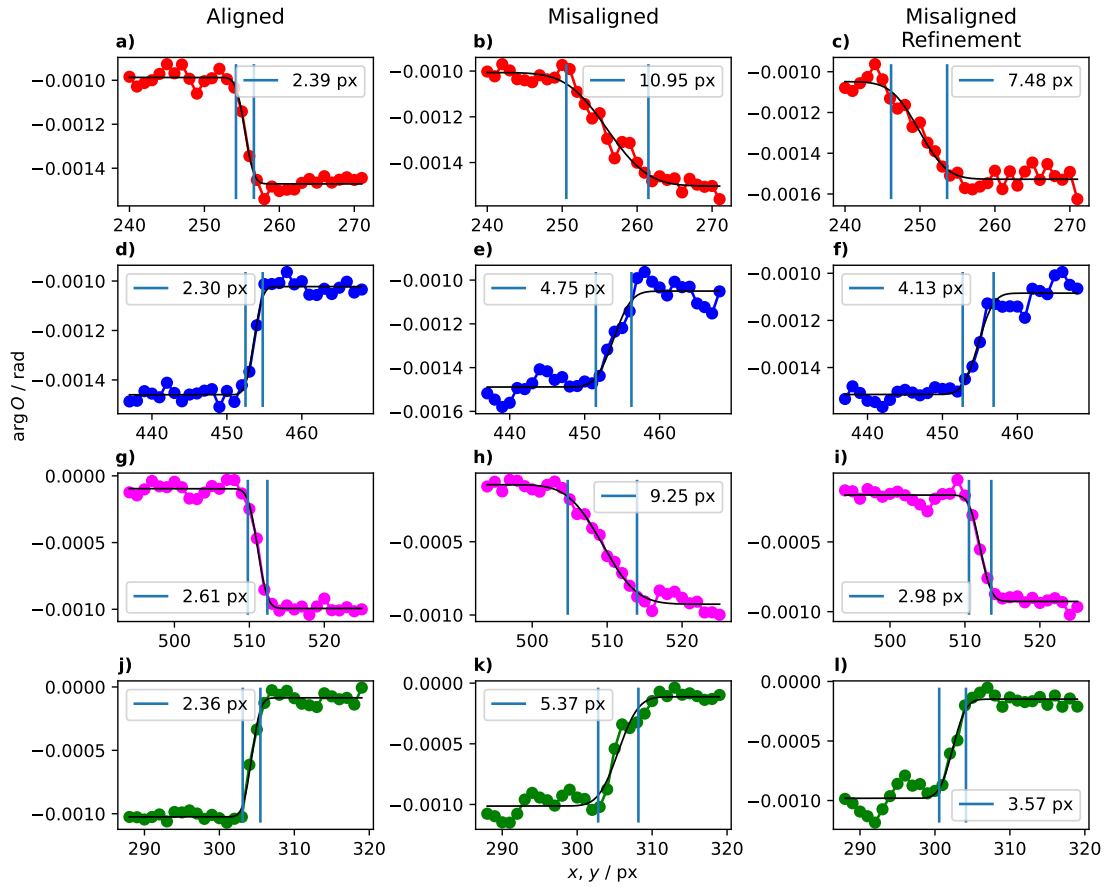


Figure 5.6: Line profiles to determine the spatial resolution of the features marked by the colored lines in figure 5.5 d). The spatial resolution is defined as the distance between the 10 % and 90 % of the maximum value of the error function fit. The determined spatial resolution is given by the label in each panel. The colored dots mark the pixel of the respective feature in figure 5.5. The black line in each plot is the fit of the error function. The fits for the aligned dataset are a), d), g), and j). The fits for the misaligned dataset without position refinement are b), e), h), and k). The fits for the misaligned dataset with position refinement are c), f), i), and l). For all features, the spatial resolution of the misaligned dataset is improved by the position refinement.

The reconstruction quality is further analyzed by line profiles. The line profiles are drawn at the four colored positions marked in figure 5.5 d). The line profile analysis is carried out for each of the three reconstructions. The line profiles and corresponding error function fits are shown in figure 5.6. The spatial resolution is defined as the distance between 10 % and 90 % of the maximum value of the error function fit. The determined spatial resolutions are given as an inset in each panel in figure 5.6. The

line profiles for the perfectly aligned dataset indicate a spatial resolution of 2 px to 3 px. The misalignment causes an increase in the spatial resolution to 4 px to 10 px. The position refinement corrects the misalignment partially and causes a decrease of the spatial resolution to 3 px to 8 px.

5.5.2 Zeolite

Now, the CPT position refinement is tested on the zeolite dataset. The scan positions \vec{r}_n of all projections are refined in a prior 2D ePIE reconstruction using the position refinement presented in section 2.2.6. The refinement started after 10 iterations and ran for 990 iterations. This is to only investigate the influence of the 2D position refinement on the projection alignment. The utilized ptychographic and tomographic reconstruction algorithm is ePIE and BP-SART, respectively. Two CPT reconstructions are done, one without and one with position refinement.

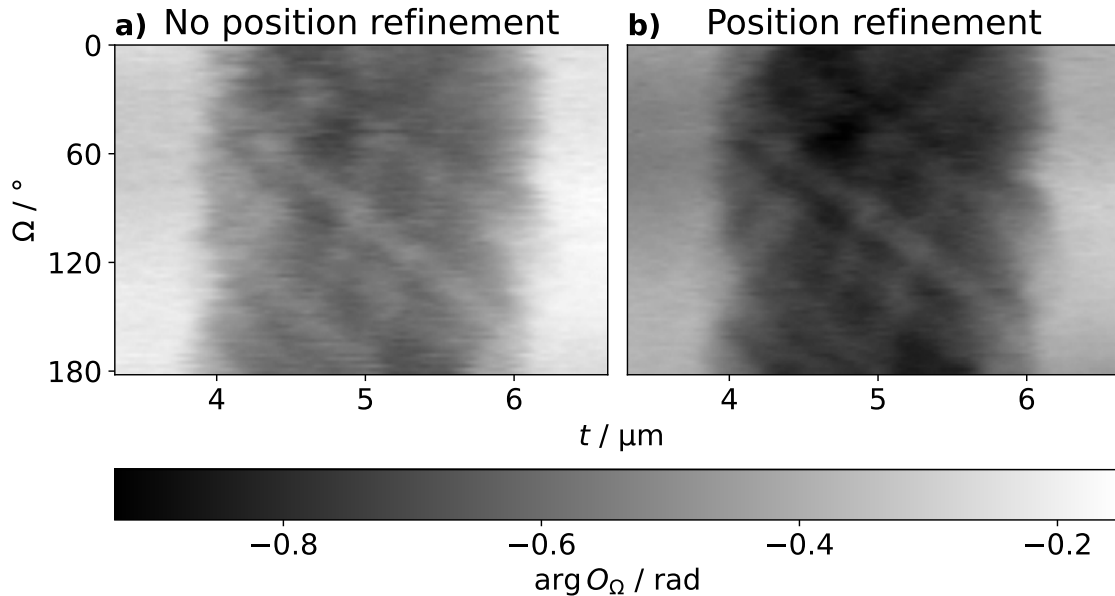


Figure 5.7: A comparison of the effect of position refinement within the CPT reconstruction. Both sinograms are created from the projections after 100 CPT iterations with ePIE and BP-SART as ptychographic and tomographic reconstruction algorithm, respectively. The shown sinograms correspond to the z position $i_z = 332$. In a), a sinogram without position refinement is shown. In b), a sinogram with positions refinement is shown. In a) it can be seen that the projections are not perfectly aligned and discontinuities are visible. In b), the sinogram is smoother and continuous.

The reconstruction without position refinement ran for 100 iterations, after which the contrast of the reconstruction converged.

The reconstruction with position refinement utilizes the state of the reconstruction without position refinement as the initial guess for the volume ν and the illuminations P_Ω . The spread of the square grid for the brute force position refinement is $r_p = 3$ px. The reconstruction with position refinement ran for 200 iterations, after which no further improvement with more iterations could be observed.

Figure 5.7 a) shows the sinogram of a central y position of the the reconstruction without position refinement. It can be seen that the dataset is well aligned, but has some discontinuities. Figure 5.7 b) shows the respective sinogram of the reconstruction with position refinement. The sinogram has a smoother shape.

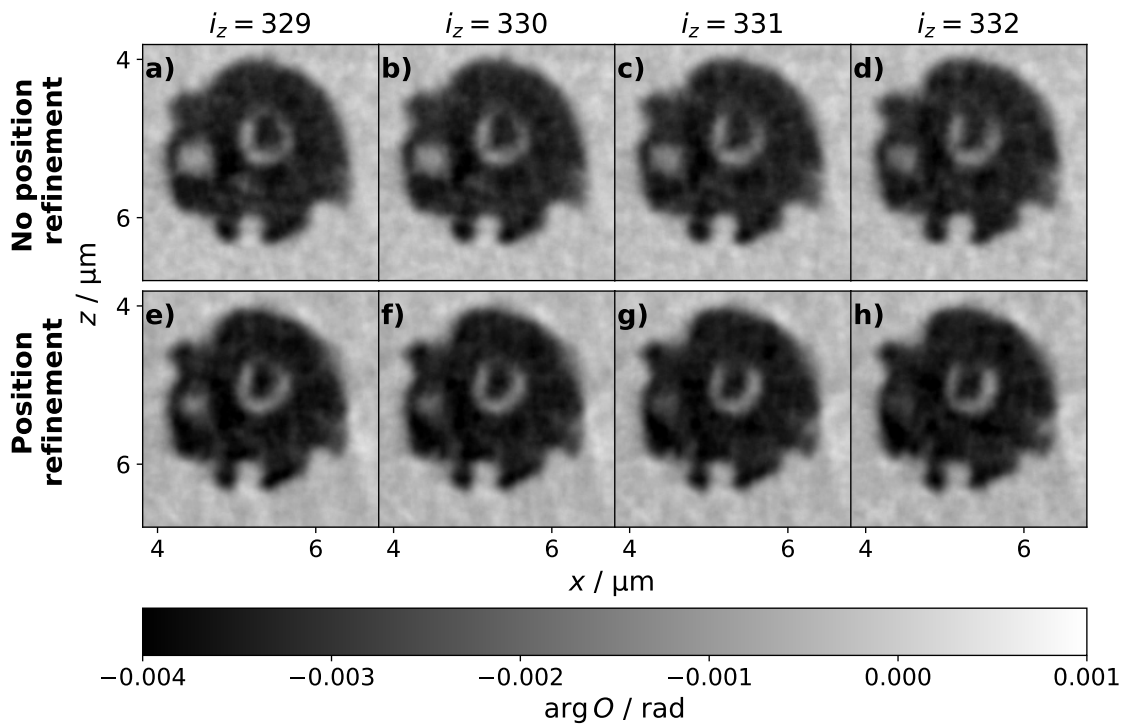


Figure 5.8: A comparison of the effect of position refinement within the CPT reconstruction. From a) to d), four reconstruction slices are shown when no position refinement is used. From e) to h), the corresponding slices with position refinement are shown.

The reconstructions of four consecutive horizontal slices are shown in figure 5.8. The slices without position refinement are shown in a) to d). The slices with position refinement are shown in e) to h). The position refinement causes that the reconstructed volume matches the measured diffraction patterns. This causes that the projections become better aligned. However, not only the projections are better aligned with each other, but also the scan positions in the individual projections are refined to match the corresponding diffraction pattern. The morphology of the

reconstruction can be overall changed by the position refinement. This is visible in figure 5.8. The bright feature on the left side of the particle is present in the reconstructions without position refinement, but the feature can be barely seen in the reconstructions with position refinement.

Furthermore, there is no obvious improvement of the reconstruction quality due to the position refinement. This is because the zeolite particle does not have any sharp edges or very defined structures that become better resolved. However, since the sinogram of the reconstruction with position refinement in figure 5.7 b) is smoother than the sinogram without position refinement in figure 5.7 a), it is concluded that the position refinement causes a better reconstruction of the actual zeolite morphology.

5.6 Conclusion

The GPU-accelerated CPT framework `ptycho3d` has been developed, that combines the ptychography software `ptycho` with tomographic operations from the ASTRA-Toolbox. The achieved performance is about a factor 3000 higher than the original implementation by Kahnt, et al. [29]. Additional ptychographic features and tomographic algorithms can be used by `ptycho3d` during the combined ptychographic tomographic reconstruction. To demonstrate this, the three ptychographic algorithms, ePIE, pePIE, and refPIE have been applied in combination with the tomographic algorithms BP-SART, SIRT, and CGLS.

Furthermore, the 2D ptychographic position correction of `ptycho` has been utilized within the CPT reconstruction. It has been shown on simulated and experimental data that this yields a better alignment of the ptychographic projections and improves the reconstruction quality.

6 Summary and Conclusion

This thesis comprises three distinct projects which advance ptychography.

First, the Ensemble Refinement (ER) has been introduced, which corrects for mechanical instabilities during a ptychographic measurement. The ER procedure has been implemented into the custom C++/CUDA software `ptycho`. Preliminary tests have been performed on simulated data, that successfully verified the general working principles and a correct implementation. Two experimental datasets were treated with the ER and reliable improvements have been achieved for both. The ePIE reconstruction of the Siemens star dataset was severely blurred and the ER resulted in a significant correction. The spatial resolution has been estimated by line profiles at four different features in the reconstruction and the improvement due to the ER was at least a factor 2. The ER prove to be stable in regard to the ensemble size parameter r_e .

The stability of the ER is imposed by an high amount of overlap. For both datasets in this work, the ratio between the illumination size and the scanning step size is about a factor 4. Furthermore, the phase of the illumination may be influential for the stability of the ER. In this work, both datasets had the object positioned behind the focal plane of the utilized X-ray optics, such that there is a profile in the illumination phase.

Nevertheless, the ER has introduced artifacts for both datasets in either free space regions, or regions that have a translation invariancy within the grid spanned by the individual ensembles. Furthermore, the computational performance is heavily reduced, which is mainly caused by the current implementation of the Non-Negative Least Squares (NNLS) fit, that utilizes only a single CPU core. Future work should focus on optimizing the NNLS fit. The performance of the NNLS fit can be increased by utilizing a more recent mathematical approach [92], [93], that can potentially reduce the runtime by more than an order of magnitude. Further, the NNLS fit should be GPU-accelerated to achieve the highest possible performance. In that sense, it may be favorable to use a parallel ptychographic algorithm, such as Difference Map (DM), so that the processing of all diffraction patterns can be parallelized [51]. These developments can reduce the runtime of the ER significantly and allow for a more routine operation.

The second project presented the implementation of online ptychography in streaming mode, which is a novel type of on-the-fly data evaluation. By the time of writ-

ing this thesis, most ptychographic microscopes still do the data evaluation offline, meaning the data acquisition and evaluation are subsequent steps. Performing the ptychographic data evaluation online allows to observe a measurement live. Mistakes can be identified and corrected, such that valuable beamtime can be saved. However, in most scenarios, the online reconstruction is unlikely to converge. Hence, a mechanism has been developed to perform offline reconstructions automatically. Part of the offline reconstruction can be to delete the raw data once it is processed. This is beneficial because less data is saved for long time and hardware resources can be saved. An additional benefit of separating the online and offline reconstruction is that the offline reconstruction is not dependent on performance. This means that the offline reconstruction can utilize even slower algorithms to achieve the best reconstruction quality, such as the ER or the maximum-likelihood refinement [98].

The third project was the development of `ptycho3d`, a GPU-accelerated software for Coupled Ptychographic Tomography (CPT) [28]. The performance of `ptycho3d` is improved by a factor 3000 to the previous implementation by Kahnt, et al. [29]. Different ptychographic and tomographic algorithms can be utilized by `ptycho3d`. Furthermore, ptychographic features such as 2D position correction can be utilized during the combined ptychographic tomographic reconstruction. It has been demonstrated on simulated and experimental data how the position correction yields an improved projection alignment. However, the 2D position refinement has not been able to fully correct a simulated misaligned dataset. For further investigations, one can use different position refinement procedures, such as the cross-correlation approach [82], or directly incorporate projection alignment procedures [101], such as tomographic consistency [102]. In principle, the ER is a viable candidate for projection alignment, too. One may also want to incorporate strategies for an automatic determination of the rotation center [103]. Alignment is an essential part of nanotomography. Including the alignment into the 3D ptychography reconstruction has the potential to reconstruct 3D ptychographic datasets in an automated manner. Once being achieved 3D ptychography provides a tool to zoom into the 3D nanostructure with a precision down a few tenth nm [40].

Combined ptychography and tomography can be further advanced by doing multi-beam ptychography. An array of illuminations is used to illuminate a large field of view of the object. This would further decrease the acquisition time by a factor up to the amount of utilized illuminations. Another benefit is the utilization of the redundancy of the entire ptycho-tomographic dataset. Multi-beam ptychography often suffers from ghost images, since multiple object regions are refined against a single diffraction pattern. The increased redundancy has the potential to stabilize

the multi-beam reconstruction.

The results achieved in this thesis are especially important for fourth generation synchrotron sources such as PETRA IV. Compared to third generation synchrotron sources, the coherent flux will increase by a factor 100 to 1000 and thereby improve the reconstruction quality, reduce the acquisition time, and significantly increase the amount of collected data. When the reconstruction quality improves, then the influence of the mechanical instabilities during the data acquisition will become more severe. An optimized version of the ER can be consistently included into the reconstruction procedure and correct for the mechanical instabilities.

To counteract the high data rates, online evaluation becomes more important to immediately process the acquired data. In this work, a pipeline has been developed that performs online and offline ptychographic reconstructions automatically. The pipeline can be extended to delete the raw data once the offline reconstruction is completed. By doing so, hardware resources are saved since the raw data is not kept for long time.

Furthermore, the increased coherent flux allows to do 3D ptychography scans in minutes. The CPT implementation presented here can catch up with such high data rates and is fast enough to allow for online analysis. This has the potential to become a reliable tool to zoom into the 3D nano-structure with a time resolution that can visualize fast dynamic processes.

Bibliography

- [1] M. Holler, M. Guizar-Sicairos, E. H. R. Tsai, *et al.*, “High-resolution non-destructive three-dimensional imaging of integrated circuits”, *Nature*, vol. 543, no. 7645, pp. 402–406, 2017.
- [2] S. Weber, A. Diaz, M. Holler, *et al.*, “Evolution of Hierarchically Porous Nickel Alumina Catalysts Studied by X-Ray Ptychography”, *Advanced Science*, vol. 9, no. 8, 2022.
- [3] A. Schropp, S. Achilles, S. Patjens, *et al.*, “3D scanning coherent x-ray microscopy at PtyNAMi”, in *Developments in X-Ray Tomography XIV*, B. Müller and G. Wang, Eds., vol. 1224208, SPIE, 2022, p. 7.
- [4] A. B. Dey, M. K. Sanyal, A. Schropp, *et al.*, “Culling a Self-Assembled Quantum Dot as a Single-Photon Source Using X-ray Microscopy”, *ACS Nano*, vol. 17, no. 16, pp. 16 080–16 088, 2023.
- [5] K. M. Spiers, D. Brueckner, J. Garrevoet, G. Falkenberg, and A. van der Ent, “Synchrotron XFM tomography for elucidating metals and metalloids in hyperaccumulator plants”, *Metallomics*, vol. 14, no. 11, pp. 3–6, 2022.
- [6] A. Gräfenstein, D. Brückner, C. Rumancev, *et al.*, “Single-Slice XRF Mapping of Light Elements in Frozen-Hydrated *Allium schoenoprasum* via a Self-Absorption-Corrected Hyperspectral Tomographic Reconstruction Approach”, *Analytical Chemistry*, vol. 95, no. 27, pp. 10 186–10 195, 2023.
- [7] S. Achilles, “3D Scanning X-ray Diffraction Microscopy on the Nanoscale”, M.S. thesis, University of Hamburg, 2020.
- [8] J. Hektor, S. Hall, N. Henningsson, *et al.*, “Scanning 3DXRD Measurement of Grain Growth, Stress, and Formation of Cu₆Sn₅ around a Tin Whisker during Heat Treatment”, *Materials*, vol. 12, no. 3, p. 446, 2019.
- [9] Y. Hayashi, Y. Hirose, and Y. Seno, “Scanning three-dimensional x-ray diffraction microscopy using a high-energy microbeam”, in *AIP Conference Proceedings*, vol. 1741, 2016, p. 050 024.
- [10] S. Y. Harouna-Mayer, S. Tao, Z. Gong, *et al.*, “Real-space texture and pole-figure analysis using the 3D pair distribution function on a platinum thin film”, *IUCrJ*, vol. 9, no. 5, pp. 594–603, 2022. arXiv: arXiv:1805.10342.

-
- [11] S. Alizadehfanaloo, J. Garrevoet, M. Seyrich, *et al.*, “Tracking dynamic structural changes in catalysis by rapid 2D-XANES microscopy”, *Journal of Synchrotron Radiation*, vol. 28, pp. 1518–1527, 2021.
- [12] D. Friebel, M. W. Louie, M. Bajdich, *et al.*, “Identification of highly active Fe sites in (Ni,Fe)OOH for electrocatalytic water splitting”, *Journal of the American Chemical Society*, vol. 137, no. 3, pp. 1305–1313, 2015.
- [13] Y. Cao, L. Guo, M. Dan, *et al.*, “Modulating electron density of vacancy site by single Au atom for effective CO₂ photoreduction”, *Nature Communications*, vol. 12, no. 1, p. 1675, 2021.
- [14] M. Scholz, “3D Multimodal X-ray Imaging of a Microchip : Correlating Structure , Composition and Orientation at the Nanoscale”, Ph.D. dissertation, University of Hamburg, 2020.
- [15] C. Ossig, C. Strelow, J. Flügge, *et al.*, “Four-Fold Multi-Modal X-ray Microscopy Measurements of a Cu(In,Ga)Se₂ Solar Cell”, *Materials*, vol. 14, no. 1, p. 228, 2021.
- [16] C. Ossig, N. Pyrlík, R. Carron, *et al.*, “X-ray vision of Cu(In,Ga)Se₂: From the Ga/In ratio to solar-cell performance”, *JPhys Energy*, vol. 4, no. 4, 2022.
- [17] L. Grote, S.-A. Hussak, L. Albers, *et al.*, “Multimodal imaging of cubic Cu₂O@Au nanocage formation via galvanic replacement using X-ray ptychography and nano diffraction”, *Scientific Reports*, vol. 13, no. 1, p. 318, 2023.
- [18] A. Saadaldin, A. M. Slyamov, M. E. Stuckelberger, *et al.*, “Multi-modal characterization of kesterite thin-film solar cells: experimental results and numerical interpretation”, *Faraday Discussions*, vol. 239, pp. 160–179, 2022.
- [19] K. W. Bossers, R. Valadian, S. Zanoni, *et al.*, “Correlated X-ray Ptychography and Fluorescence Nano-Tomography on the Fragmentation Behavior of an Individual Catalyst Particle during the Early Stages of Olefin Polymerization”, *Journal of the American Chemical Society*, vol. 142, no. 8, pp. 3691–3695, 2020.
- [20] T. Feggeler, A. Levitan, M. A. Marcus, H. Ohldag, and D. A. Shapiro, “Scanning transmission X-ray microscopy at the Advanced Light Source”, *Journal of Electron Spectroscopy and Related Phenomena*, vol. 267, no. May, p. 147 381, 2023.

-
- [21] A. Schropp, R. Hoppe, J. Patommel, *et al.*, “Hard x-ray scanning microscopy with coherent radiation: Beyond the resolution of conventional x-ray microscopes”, *Applied Physics Letters*, vol. 100, no. 25, 2012.
- [22] A. Schropp, R. Döhrmann, S. Botta, *et al.*, “PtyNAMi: ptychographic nano-analytical microscope”, *Journal of Applied Crystallography*, vol. 53, no. 4, pp. 957–971, 2020.
- [23] D. A. Shapiro, R. Celestre, B. Enders, *et al.*, “The COSMIC Imaging Beamline at the Advanced Light Source: a new facility for spectro-microscopy of nano-materials”, *Microscopy and Microanalysis*, vol. 24, no. S2, pp. 8–11, 2018.
- [24] S. Sala, D. J. Batey, A. Prakash, S. Ahmed, C. Rau, and P. Thibault, “Ptychographic X-ray computed tomography at a high-brilliance X-ray source”, *Optics Express*, vol. 27, no. 2, p. 533, 2019.
- [25] M. Guizar-Sicairos, I. Johnson, A. Diaz, *et al.*, “High-throughput ptychography using Eiger-scanning X-ray nano-imaging of extended regions”, *Optics Express*, vol. 22, no. 12, p. 14 859, 2014.
- [26] P. Godard, G. Carbone, M. Allain, *et al.*, “Three-dimensional high-resolution quantitative microscopy of extended crystals”, *Nature Communications*, vol. 2, no. 1, p. 568, 2011.
- [27] J. Deng, C. Preissner, J. A. Klug, *et al.*, “The Velociprobe: An ultrafast hard X-ray nanoprobe for high-resolution ptychographic imaging”, *Review of Scientific Instruments*, vol. 90, no. 8, 2019.
- [28] D. Gürsoy, “Direct coupling of tomography and ptychography”, *Optics Letters*, vol. 42, no. 16, p. 3169, 2017.
- [29] M. Kahnt, J. Becher, D. Brückner, *et al.*, “Coupled ptychography and tomography algorithm improves reconstruction of experimental data”, *Optica*, vol. 6, no. 10, p. 1282, 2019.
- [30] C. G. Schroer, H.-C. Wille, O. H. Seeck, *et al.*, “The synchrotron radiation source PETRA III and its future ultra-low-emittance upgrade PETRA IV”, *The European Physical Journal Plus*, vol. 137, no. 12, p. 1312, 2022.
- [31] T. Hellert, C. Steier, and M. Venturini, “Lattice correction and commissioning simulation of the Advanced Light Source upgrade storage ring”, *Physical Review Accelerators and Beams*, vol. 25, no. 11, p. 110 701, 2022.
-

-
- [32] A. Robert, Y. Cerenius, P. F. Tavares, *et al.*, “MAX IV Laboratory”, *The European Physical Journal Plus*, vol. 138, no. 6, p. 495, 2023.
- [33] R. Hettel, “STATUS OF THE APS-U PROJECT *”, in *IPAC 2021 - Proceedings of the 12th International Particle Accelerator Conference*, JACoW Publishing, 2021, pp. 7–12.
- [34] J. Biasci, J. Bouteille, N. Carmignani, *et al.*, “A Low-Emittance Lattice for the ESRF”, *Synchrotron Radiation News*, vol. 27, no. 6, pp. 8–12, 2014.
- [35] G. Xu, X. H. Cui, Z. Duan, *et al.*, “Progress of the lattice design and physics studies on the high energy photon source”, *IPAC 2017 - Proceedings of the 8th International Particle Accelerator Conference*, no. December, pp. 2697–2699, 2017.
- [36] K. Soutome, T. Hiraiwa, and H. Tanaka, “UPDATE OF LATTICE DESIGN OF THE SPring-8-II STORAGE RING TOWARDS 50 pmrad”, in *Proceedings of IPAC2022*, JACoW Publishing, 2022, pp. 477–480.
- [37] J. Als-Nielsen and D. McMorrow, *Elements of Modern X-ray Physics*. Wiley, 2011.
- [38] J. W. Goodman, *Introduction to Fourier Optics McGraw-Hill Series in Electrical and Computer Engineering*, 2nd ed. The McGraw-Hill Companies, 1996.
- [39] J. Rodenburg and A. Maiden, “Ptychography”, in *Springer Handbooks*, Springer, 2019, pp. 819–904.
- [40] M. Holler, A. Diaz, M. Guizar-Sicairos, *et al.*, “X-ray ptychographic computed tomography at 16 nm isotropic 3D resolution”, *Scientific Reports*, vol. 4, no. 1, p. 3857, 2014.
- [41] M. Dierolf, A. Menzel, P. Thibault, *et al.*, “Ptychographic X-ray computed tomography at the nanoscale”, *Nature*, vol. 467, no. 7314, pp. 436–439, 2010.
- [42] Y. S. Yu, M. Farmand, C. Kim, *et al.*, “Three-dimensional localization of nanoscale battery reactions using soft X-ray tomography”, *Nature Communications*, vol. 9, no. 1, pp. 1–7, 2018. arXiv: 1711.01525.
- [43] C. G. Schroer, S. Hönig, A. Goldschmidt, *et al.*, “Hard x-ray nano-beam characterization by ptychographic imaging”, *Advances in Computational Methods for X-Ray Optics II*, vol. 8141, no. September 2011, p. 814 103, 2011.

-
- [44] C. G. Schroer, F. Seiboth, A. Schropp, *et al.*, “Hard x-ray wavefront engineering for aberration correction and beam shaping”, in *Advances in X-Ray/EUV Optics and Components XVII*, H. Mimura, C. Morawe, and A. M. Khounsary, Eds., SPIE, 2022, p. 10.
- [45] F. Seiboth, A. Kubec, A. Schropp, *et al.*, “Rapid aberration correction for diffractive X-ray optics by additive manufacturing”, *Optics Express*, vol. 30, no. 18, p. 31 519, 2022.
- [46] O. Bunk, M. Dierolf, S. Kynde, I. Johnson, O. Marti, and F. Pfeiffer, “Influence of the overlap parameter on the convergence of the ptychographical iterative engine”, *Ultramicroscopy*, vol. 108, no. 5, pp. 481–487, 2008.
- [47] J. M. Rodenburg and H. M. Faulkner, “A phase retrieval algorithm for shifting illumination”, *Applied Physics Letters*, vol. 85, no. 20, pp. 4795–4797, 2004.
- [48] P. Thibault, M. Dierolf, A. Menzel, O. Bunk, C. David, and F. Pfeiffer, “High-Resolution Scanning X-ray Diffraction Microscopy”, *Science*, vol. 321, no. 5887, pp. 379–382, 2008.
- [49] A. Maiden, D. Johnson, and P. Li, “Further improvements to the ptychographical iterative engine”, *Optica*, vol. 4, no. 7, p. 736, 2017.
- [50] A. M. Maiden and J. M. Rodenburg, “An improved ptychographical phase retrieval algorithm for diffractive imaging”, *Ultramicroscopy*, vol. 109, no. 10, pp. 1256–1262, 2009.
- [51] P. Thibault, M. Dierolf, O. Bunk, A. Menzel, and F. Pfeiffer, “Probe retrieval in ptychographic coherent diffractive imaging”, *Ultramicroscopy*, vol. 109, no. 4, pp. 338–343, 2009.
- [52] F. Wittwer, J. Hagemann, D. Brückner, S. Flenner, and C. G. Schroer, “Phase retrieval framework for direct reconstruction of the projected refractive index applied to ptychography and holography”, *Optica*, vol. 9, no. 3, p. 295, 2022.
- [53] H. Chang, P. Enfedaque, and S. Marchesini, “Blind Ptychographic Phase Retrieval via Convergent Alternating Direction Method of Multipliers”, *SIAM Journal on Imaging Sciences*, vol. 12, no. 1, pp. 153–185, 2019. arXiv: 1808.05802.

-
- [54] R. Hesse, D. R. Luke, S. Sabach, and M. K. Tam, “Proximal Heterogeneous Block Implicit-Explicit Method and Application to Blind Ptychographic Diffraction Imaging”, *SIAM Journal on Imaging Sciences*, vol. 8, no. 1, pp. 426–457, 2015.
- [55] Z. Wen, C. Yang, X. Liu, and S. Marchesini, “Alternating direction methods for classical and ptychographic phase retrieval”, *Inverse Problems*, vol. 28, no. 11, 2012.
- [56] H. Chang, P. Enfedaque, Y. Lou, and S. Marchesini, “Partially coherent ptychography by gradient decomposition of the probe”, *Acta Crystallographica Section A Foundations and Advances*, vol. 74, no. 3, pp. 157–169, 2018. arXiv: 1710.07382.
- [57] J. Reinhardt and C. Schroer, “Quantitative ptychographic reconstruction by applying a probe constraint”, *Journal of Instrumentation*, vol. 13, no. 04, pp. C04016–C04016, 2018.
- [58] P. Thibault and A. Menzel, “Reconstructing state mixtures from diffraction measurements”, *Nature*, vol. 494, no. 7435, pp. 68–71, 2013.
- [59] C. Yang, J. Qian, A. Schirotzek, F. Maia, and S. Marchesini, “Iterative Algorithms for Ptychographic Phase Retrieval”, pp. 630–632, 2011. arXiv: 1105.5628.
- [60] S. Welker, T. Peer, H. N. Chapman, and T. Gerkmann, “Live Iterative Ptychography with projection-based algorithms”, 2023. arXiv: 2309.08639.
- [61] F. Wittwer, “Development and Study of Refractive Phase Retrieval and X-ray Multibeam Ptychography Dissertation”, Ph.D. dissertation, University of Hamburg, 2020.
- [62] B. Enders and P. Thibault, “A computational framework for ptychographic reconstructions”, *Proceedings of the Royal Society A: Mathematical, Physical and Engineering Sciences*, vol. 472, no. 2196, p. 20160640, 2016.
- [63] K. Wakonig, H.-C. Stadler, M. Odstrčil, *et al.*, “PtychoShelves , a versatile high-level framework for high-performance analysis of ptychographic data”, *Journal of Applied Crystallography*, vol. 53, no. 2, pp. 574–586, 2020.
- [64] M. J. Cherukara, T. Zhou, Y. Nashed, *et al.*, “AI-enabled high-resolution scanning coherent diffraction imaging”, *Applied Physics Letters*, vol. 117, no. 4, 2020.

-
- [65] L. Loetgering, M. Du, D. Boonzajer Flaes, *et al.*, “PtyLab.m/py/jl: a cross-platform, open-source inverse modeling toolbox for conventional and Fourier ptychography”, *Optics Express*, vol. 31, no. 9, p. 13 763, 2023. arXiv: 2301.06595.
- [66] Y. S. G. Nashed, D. J. Vine, T. Peterka, J. Deng, R. Ross, and C. Jacobsen, “Parallel ptychographic reconstruction”, *Optics Express*, vol. 22, no. 26, p. 32 082, 2014.
- [67] S. Marchesini, H. Krishnan, B. J. Daurer, *et al.*, “SHARP: A distributed GPU-based ptychographic solver”, *Journal of Applied Crystallography*, vol. 49, no. 4, pp. 1245–1252, 2016. arXiv: 1602.01448.
- [68] K. Yue, J. Deng, Y. Jiang, Y. Nashed, D. Vine, and S. Vogt, “Ptychopy: GPU framework for ptychographic data analysis”, in *X-Ray Nanoimaging: Instruments and Methods V*, B. Lai and A. Somogyi, Eds., SPIE, 2021, p. 4. arXiv: 2202.03144.
- [69] A. M. Maiden, M. J. Humphry, F. Zhang, and J. M. Rodenburg, “Superresolution imaging via ptychography”, *Journal of the Optical Society of America A*, vol. 28, no. 4, p. 604, 2011.
- [70] V. Favre-Nicolin, G. Girard, S. Leake, *et al.*, “PyNX: High-performance computing toolkit for coherent X-ray imaging based on operators”, *Journal of Applied Crystallography*, vol. 53, pp. 1404–1413, 2020. arXiv: 2008.11511.
- [71] Robert Hoppe, “Anpassung und Optimierung des ptychographischen Modells für die quantitative Mikroskopie mit kohärenter Röntgenstrahlung und sichtbarem Laserlicht”, Ph.D. dissertation, University of Hamburg, 2019.
- [72] S. Achilles, S. Ehrig, N. Hoffmann, *et al.*, “GPU-accelerated coupled ptychographic tomography”, in *Developments in X-Ray Tomography XIV*, B. Müller and G. Wang, Eds., SPIE, 2022, p. 21.
- [73] Y. Yao, Y. Jiang, J. A. Klug, *et al.*, “Multi-beam X-ray ptychography for high-throughput coherent diffraction imaging”, *Scientific Reports*, vol. 10, no. 1, p. 19 550, 2020.
- [74] M. Lyubomirskiy, F. Wittwer, M. Kahnt, *et al.*, “Multi-beam X-ray ptychography using coded probes for rapid non-destructive high resolution imaging of extended samples”, *Scientific Reports*, vol. 12, no. 1, p. 6203, 2022.

-
- [75] F. Wittwer, M. Lyubomirskiy, F. Koch, *et al.*, “Upscaling of multi-beam x-ray ptychography for efficient x-ray microscopy with high resolution and large field of view”, *Applied Physics Letters*, vol. 118, no. 17, 2021.
- [76] A. M. Maiden, M. J. Humphry, and J. M. Rodenburg, “Ptychographic transmission microscopy in three dimensions using a multi-slice approach”, *Journal of the Optical Society of America A*, vol. 29, no. 8, p. 1606, 2012.
- [77] M. Kahnt, L. Grote, D. Brückner, *et al.*, “Multi-slice ptychography enables high-resolution measurements in extended chemical reactors”, *Scientific Reports*, vol. 11, no. 1, p. 1500, 2021.
- [78] A. Schropp, R. Hoppe, V. Meier, *et al.*, “Full spatial characterization of a nanofocused X-ray free-electron laser beam by ptychographic imaging”, *Scientific Reports*, vol. 3, pp. 1–5, 2013.
- [79] C. G. Schroer, C. Baumbach, R. Döhrmann, *et al.*, “Hard x-ray nanoprobe of beamline P06 at PETRA III”, in *AIP Conference Proceedings*, vol. 1741, 2016, p. 030 007.
- [80] A. Maiden, M. Humphry, M. Sarahan, B. Kraus, and J. Rodenburg, “An annealing algorithm to correct positioning errors in ptychography”, *Ultramicroscopy*, vol. 120, pp. 64–72, 2012.
- [81] P. Dwivedi, A. Konijnenberg, S. Pereira, and H. Urbach, “Lateral position correction in ptychography using the gradient of intensity patterns”, *Ultramicroscopy*, vol. 192, pp. 29–36, 2018.
- [82] F. Zhang, I. Peterson, J. Vila-Comamala, *et al.*, “Translation position determination in ptychographic coherent diffraction imaging”, *Optics Express*, vol. 21, no. 11, p. 13 592, 2013.
- [83] A. C. Kak and M. Slaney, *Principles of Computerized Tomographic Imaging*. Society for Industrial and Applied Mathematics, 2001, pp. 275–296.
- [84] Johann Radon, “Über die Bestimmung von Funktionen durch ihre Integralwerte längs gewisser Mannigfaltigkeiten”, *Verh. Säch. Akad. Wiss. Leipzig*, vol. 295, pp. 262–277, 1917.
- [85] N. Andrei, “Conjugate Gradient Methods”, in *Springer Optimization and Its Applications*, vol. 195, 2022, pp. 169–260.
- [86] W. van Aarle, W. J. Palenstijn, J. Cant, *et al.*, “Fast and flexible X-ray tomography using the ASTRA toolbox”, *Optics Express*, vol. 24, no. 22, p. 25 129, 2016.

-
- [87] M. Kahnt, S. Sala, U. Johansson, *et al.*, “First ptychographic X-ray computed tomography experiment on the NanoMAX beamline”, *Journal of Applied Crystallography*, vol. 53, no. 6, pp. 1444–1451, 2020.
- [88] D. Gürsoy, Y. P. Hong, K. He, *et al.*, “Rapid alignment of nanotomography data using joint iterative reconstruction and reprojection”, *Scientific Reports*, vol. 7, no. 1, p. 11 818, 2017.
- [89] K. M. Seyrich, “High-Resolution and In-Solution Hard X-ray Ptychography at the Ptychographic Nano-Analytical Microscope PtyNAMi”, Ph.D. dissertation, University of Hamburg, 2020.
- [90] C. L. Lawson and R. J. Hanson, *Solving Least Squares Problems*. Society for Industrial and Applied Mathematics, 1995.
- [91] M. Kahnt, “3D nano-tomography using coherent X-rays”, Ph.D. dissertation, University of Hamburg, 2020.
- [92] J. Myre, E. Frahm, D. Lilja, and M. Saar, “TNT-NN: A Fast Active Set Method for Solving Large Non-Negative Least Squares Problems”, *Procedia Computer Science*, vol. 108, pp. 755–764, 2017.
- [93] J. Diakonikolas, C. Li, S. Padmanabhan, and C. Song, “A Fast Scale-Invariant Algorithm for Non-negative Least Squares with Non-negative Data”, *Advances in Neural Information Processing Systems*, vol. 35, 2022. arXiv: 2203.03808.
- [94] D. Weber, S. Ehrig, A. Schropp, *et al.*, “Live Iterative Ptychography”, 2023. arXiv: 2308.10674.
- [95] S. Achilles, *Cosmicstreams*, <https://github.com/silvioachilles/cosmicstreams>, Accessed 14.11.2023.
- [96] S. Achilles, *Cosmicstreams*, <https://github.com/silvioachilles/cosmicstreams>, Accessed 14.11.2023.
- [97] F. R. N. C. Maia, *The cxi file format*, <https://www.cxidb.org/cxi.html>, Accessed 14.11.2023.
- [98] P. Thibault and M. Guizar-Sicairos, “Maximum-likelihood refinement for coherent diffractive imaging”, *New Journal of Physics*, vol. 14, no. 6, p. 063 004, 2012.

-
- [99] T. Ramos, B. E. Grønager, M. S. Andersen, and J. W. Andreasen, “Direct three-dimensional tomographic reconstruction and phase retrieval of far-field coherent diffraction patterns”, *Physical Review A*, vol. 99, no. 2, p. 023 801, 2019.
- [100] V. Nikitin, S. Aslan, Y. Yao, *et al.*, “Photon-limited ptychography of 3D objects via Bayesian reconstruction”, *OSA Continuum*, vol. 2, no. 10, p. 2948, 2019.
- [101] M. Odstrčil, M. Holler, J. Raabe, and M. Guizar-Sicairos, “Alignment methods for nanotomography with deep subpixel accuracy”, *Optics Express*, vol. 27, no. 25, p. 36 637, 2019.
- [102] M. Cop and J. Dengler, “A multiresolution approach to the 3D reconstruction of a 50S ribosome from an EM-tilt series solving the alignment problem without gold particles (electron microscopy)”, in *[1990] Proceedings. 10th International Conference on Pattern Recognition*, vol. i, IEEE Comput. Soc. Press, 1990, pp. 733–737.
- [103] T. Donath, F. Beckmann, and A. Schreyer, “Automated determination of the center of rotation in tomography data”, *Journal of the Optical Society of America A*, vol. 23, no. 5, p. 1048, 2006.

7 Acknowledgements

Without the help and support of the many people I have worked with, I would not have been able to create this work.

First and foremost, I would like to thank the supervisor and first reviewer of this thesis, Prof. Christian G. Schroer. Christian has impressive knowledge and is by far the most advanced scientist that I have met. His suggestions have always helped me and encouraged me to further deepen my knowledge. I am also very grateful for Christian's generosity in allowing me to conduct one of my research projects in California.

I would also like to express my deepest gratitude to Dr. Andreas Schropp for being my co-supervisor and guiding me through the many projects we have worked on over the last few years. I would also like to thank Prof. Peter Modregger for being the second reviewer of this thesis, and furthermore, the examination committee for taking the time to review and evaluate my work.

It can't be stressed enough how much I thrived from the discussions with my colleagues in the X-ray Nanoscience and X-ray Optics group. Especially I would like to thank Johannes Hagemann, Tang Li, Sina Röper, Martin Seyrich, and Johannes Dora for their help, advice and review. The atmosphere at work was always comfortable and enjoyable and I would like to sincerely thank every group member for that. I would like to give my gratitude to Christina Newiger for all the organizational help. I would also like to thank my friends Jackson Barp, Vincent Strenzke and Sani Harouna-Mayer for going together on the journey of a doctoral thesis.

Special thanks go to Nico Hoffmann and Simeon Ehrig from Helmholtz Zentrum Dresden-Rossendorf. Quite in the beginning of my employment, Nico invited me to a weekly developer meeting and supervised my work. Simeon supported me numerous times during the implementation of new features to `ptycho`, and his help was invaluable for my progress.

Special thanks also go to my collaborators at the Berkeley Laboratory, David Shapiro, Yanqi (Grace) Luo, Abe Levitan, Dylan McReynolds, and Alex Hexemer. Especially I like to thank David, who has a very tight schedule but still was very responsive and gave me always great suggestions. I would also like to thank Dong Hyun Kim for his company during the time at LBNL.

Finally, I would like to thank my family and friends for the constant support I have been able to rely on over the past few years.

Eidesstattliche Versicherung

Hiermit erkläre ich an Eides statt, dass ich die vorliegende Dissertationsschrift selbst verfasst und keine anderen als die angegebenen Hilfsmittel und Quellen benutzt habe.

Hamburg, 15. November 2023

Silvio Achilles